Electronic transport and spin control in SiGe self-assembled quantum dots

Natalia Ares

Natalia Ares. Electronic transport and spin control in SiGe self-assembled quantum dots. Quantum Physics [quant-ph]. Université de Grenoble, 2013. English. NNT : 2013GRENY060 . tel-01499920

HAL Id: tel-01499920
https://theses.hal.science/tel-01499920

Submitted on 1 Apr 2017

UNIVERSITÉ DE GRENOBLE

THÈSE

Pour obtenir le grade de

DOCTEUR DE L'UNIVERSITÉ DE GRENOBLE

Spécialité : **Nanophysique**

Arrêté ministériel : 23 avril 2009

Présentée par

Natalia Ares

Thèse dirigée par **François Lefloch et Silvano De Franceschi**

préparée au sein du **Laboratoire de**
Transport Électronique Quantique et Supraconductivité
et de l'école doctorale **de Physique de Grenoble**

Electronic transport and spin control in SiGe self-assembled quantum dots

Thèse soutenue publiquement le **24 octobre 2013**,
devant le jury composé de :

Julia S. Meyer
Prof., Université Joseph Fourier Grenoble, Président
Seigo Tarucha
Prof., University of Tokyo, Rapporteur
Andreas Fuhrer
Dr., IBM Zurich Research Laboratory, Rapporteur
Yuli V. Nazarov
Prof., TU Delft, Examinateur
Silvano De Franceschi
HDR, CEA Grenoble, Directeur de thèse
François Lefloch
HDR, CEA Grenoble, Directeur de thèse

Acknowledgements

To begin with, I would like to thank the reviewers of this thesis, Dr. Andreas Fuhrer and Prof. Seigo Tarucha, as well as the other honourable members of the jury; Prof. Julia S. Meyer and Prof. Yuli V. Nazarov.

Furthermore, the realization of this work would not have been possible without the immense support of many people. In the first place, I would like to thank Silvano De Franceschi and Georgios Katsaros for their guide and patience during these years. Silvano has been an inspiring source of exciting ideas and Georgios, a indefatigable guide through each step towards the actual realization of these.

I would also like to thank Aaron Prager and Eduardo Lee for their always at hand help and advise, and for the many pleasant moments shared at the lab. I want to thank Elena Talache-Prager and Isil Aydin too, for their warmth and caring.

For the support I have been given at the beginning, I would like to mention Massimo Mongillo et Panayotis Spathis and for the last few months, Juan Carlos Estrada, Patrick Torresani and Julien Renard.

Finally, I would like to thank Vitaly Golovach for the production and constant enlightenment of all the theoretical work presented in this thesis.

Bien que je n'ai pas appris plus que quelques mots, je voudrais remercier certaines personnes en français. Premièrement, à François Lefloch, pour son énorme patience, ses attentions, et surtout pour sa qualité humaine incomparable.

À Jean-Luc Thomassin, Frederic Gustavo, Christophe Lemonias, Frederic Poletti, Iulian Matei et Jean-Michel Martinod, pour faire de la 'magie' et pour être toujours prêt à m'aider. Et finalement à Georg Knebel, Christophe Marcenat, Louis Jansen, Claude Chapelier, Xavier Jehl, Laurent Vila, Marc Sanquer et Jean-Pascal Brison pour leur énorme soutien et à Benoit Voisin, Benoît Roche, Andreas Pfeffer, Charlène Tonnoir, Alexander Grimm, Toai Le Quang, Paul Clapera, Soumya Ray, Mathieu Taupin et Audrey Grockowiak, parmi beaucoup d'autres camarades, pour leur compagnie.

Y, por último, en porteño, quiero agradecer a mi familia y amigos por su cariño, contención y apoyo incondicional. Por hacerme sentir que 10.000 km no son nada y por perdonar tantas ausencias. Especialmente a mi mamá, por ponerme siempre primero y por el esfuerzo y las lágrimas puestas en dejarme ir. A mi hermana, por su infinita capacidad para quererme y mimarme. Y a mi nonna, por ser desde siempre mi fan número uno. Quiero mencionar también a Naty, por estar siempre dispuesta a rescatarme a donde quiera que vaya, a mis tíos y a mi nonno, por quererme tanto, a Cami, a Patri y también a las últimas adquisiciones, Marcelo, Martín y Carlos.

A Elisa Chisari, Ariel Berenstein, Ezequiel Badgen, Nahuel Vega y Maricel Repetto por cuidar nuestra amistad a pesar de la distancia. Gracias por estar siempre para mí.

A mi familia política, Mercedes, Lucía, Pablo, Clara, Alberto y Alejandra y Ricardo, por el gran cariño que me brindan.

Y para terminar, a Martín Obligado por ser mi incondicional compañero, sostén en los momentos más difíciles. Vos hiciste que todo esto fuera posible.

Gracias, gracias, gracias,

Natalia

Extrait en français

Introduction

La mécanique quantique affiche déjà toute son étrangeté en considérant l'équation de Schrdinger dans un puits de potentiel à une dimension. L'effet tunnel qui en résulte, en est un exemple frappant. La possibilité de récréer cette situation dans un système matériel est un enjeu excitant et un grand pas vers le contrôle des effets quantiques. Par exemple, il est maintenant possible de confiner des électrons dans des dispositifs semi-conducteurs permettant une technologie de cellules solaires plus efficaces.

Le confinement spatial des spins électroniques a été suggéré comme une approche possible pour la réalisation d'un ordinateur quantique. Chaque spin formant un système à deux niveaux pouvant coder une bit élémentaire pour l'information quantique (spin qubit). Cette proposition par Loss et Di Vincenzo a contribué à l'ouverture d'un domaine de recherche important dénommé spintronique quantique. L'intérêt des qubits de spin s'appuie sur le fait que les états de spin ont des temps de cohérence beaucoup plus long que les qubits de charge (états orbitaux).

Un potentiel de confinement de spin peut être créé de différentes façons comme en appliquant à la fois un champ magnétique et un champ électrostatique, par l'application de champs électriques alternatifs ou encore à l'interface entre différentes couches d'oxydes conducteurs. L'utilisation de l'alignement des bandes d'énergies de semi-conducteurs de différentes natures permet également de créer un potentiel de confinement. Cependant, les dimensions spatiales du système obtenu doivent toujours être inférieures à la longueur de cohérence de phase des quasi-particules considérées afin de préserver leur comportement quantique.

Jusqu'à présent, la plupart des progrès ont été réalisés en utilisant des hétérostructures semiconductrices à base d'arsenure de Gallium (GaAs). Dans de tels systèmes, le mouvement des porteurs de charges est limité à un plan bidimensionnel et le confinement latéral peut être obtenu par des techniques de lithographie jusqu'à des tailles inférieures à 100 nm. De cette façon, des systèmes quasi-zéro-dimensionnels dont les états électroniques sont parfaitement quantifiés (boîtes quantiques), sont réalisés.

Diverses techniques utilisant des signaux hautes fréquences ont permis de manipuler et lire l'état de spin de tels boîtes quantiques de GaAs et, il y a quelques années, les premiers qubits de spin ont été démontrés. Cependant, ces systèmes ont montré des temps de cohérence relativement courts en raison de l'interaction hyperfine avec les spins nucléaires du Gallium et de l'Arsenic. En dépit de progrès significatifs sur le contrôle de la polarisation, ce problème n'est toujours pas résolu.

Au cours de ces dernières années, un effort croissant s'est donc concentré sur des systèmes à base de matériaux alternatifs pour lesquels l'interaction hyperfine est naturellement absente ou rendue très faible par des techniques de purification. Même si le Silicium, qui est le matériau de base en microélectronique, remplit cette condition, il souffre d'une faible mobilité par rapport aux semiconducteurs III-V ce qui pose problème pour la spintronique quantique. Les structures à base Silicium-Germanium (SiGe) offrent un moyen de contourner ce problème tout en gardant un matériau compatible avec les procédés de fabrication standards [1].

Durant mon travail de thèse, je me suis concentrée principalement sur l'étude des propriétés électroniques d'îlots auto-assemblés (nanocristaux) de SiGe. Le manuscrit de thèse qui relate les principaux aspects de cette étude est organisé en six chapitres. Dans le premier chapitre, je décris les principaux concepts de la croissance cristalline d'îlots auto-assemblés de SiGe ainsi que les propriétés du potentiel de confinement qu'ils définissent. Le chapitre 2 est consacré aux principes du transport électronique dans de telles structures. Le chapitre 3 traite de la modulation électrique du facteur de Landé (g) des trous confinés dans les îlots en vu de la manipulation rapide des états de spin. Dans le chapitre 4, je présente les résultats théoriques et expérimentaux relatifs à la sélectivité en spin dans les nanocristaux de SiGe. Le chapitre 5 décrit les résultats sur la réalisation d'une pompe électronique obtenue à partir de nanofils d'InAs/InP. Enfin, le chapitre 6 montre les progrès technologiques que j'ai obtenus vers la réalisation et l'étude de dispositifs couplés à base de nanocristaux de SiGe.

---

[1] La mobilité électronique augmente avec la concentration en Ge dans les couches de SiGe.

Résumé

Le Silicium (Si) et le Germanium (Ge) sont des semi-conducteurs miscibles dans tout le domaine de composition. Les deux matériaux ont une structure cristalline de forme diamant mais leurs paramètres de maille sont différents: 5.43 $\AA$ pour le Si et 5.66 $\AA$ pour le Ge. Dans une première phase de croissance, le Ge pousse en couches minces sur un substrat de Si (100). A cause du désaccord de paramètres de maille entre les deux matériaux une contrainte biaxiale se construit et est libérée à partir de 3-4 couches atomiques. Cette relaxation de contrainte se fait soit par l'établissement de dislocations, soit par la formation de structures cristallines 3D appelées îlots (croissance Stranski-Krastanov).

Les nanostructures formées peuvent avoir une variété de tailles et de formes en fonction des paramètres de croissance. Dans cette thèse, je me suis intéressée essentiellement aux îlots en forme de dôme. Ces îlots ont une structure cristalline et des dimensions ($\sim$ 100 nm) accessibles par les moyens actuels de nanofabrication. En fonction de l'alignement des bandes de conduction et de valence un potentiel de confinement pour les trous peut être créé (chapitre 1).

Afin d'étudier les propriétés de transport électronique, il est nécessaire de pouvoir contacter électriquement ces îlots. La technique généralement utilisée et dont la mise au point a également fait partie de mon travail de thèse, consiste à utiliser des procédés de nanofabrication pour déposer sur ces îlots plusieurs contacts métalliques (source, drain et grille). Les contacts drain et source permettent de connaitre la réponse électrique du système alors que la tension de grille offre la possibilité de régler les niveaux d'énergie dans l'îlot. Les premières mesures de transport électronique obtenues par le groupe sont résumées dans ce manuscrit (chapitre 2) ce qui permet de décrire et de détailler les concepts généraux de la physique sous-jacente aux systèmes que j'ai étudiés: spectres d'énergie discrets, couplage spin-orbite, anisotropie du facteur de Landé, effet du champ magnétique, etc.

Durant ma thèse, j'ai contribué à la mise au point d'une étude expérimentale de résonance de spin électronique (ESR). Cette technique consiste à ma-

nipuler de manière cohérente l'état de spin des électrons grâce à un champ radio-fréquence. Les techniques habituelles consistent à placer le système dans un champ magnétique statique et d'appliquer un champ magnétique alternatif perpendiculaire au champ statique pour exciter et manipuler les spins. Dans notre cas, le champ magnétique radio-fréquence est remplacé par un champ électrique et la modulation du facteur de Landé permet d'exciter les spins électroniques. Mon travail a permis l'observation expérimentale d'une modulation exceptionnelle et non-monotone du facteur de Landé dans ces îlots de SiGe (chapitre 3). Pour interpréter ces résultats, nous proposons un nouveau mécanisme appliqué à un système de trous à basse dimensionnalité. Ce mécanisme repose sur l'existence d'un terme de correction important dans le facteur de Landé et ignoré jusqu'ici. Nous montrons également que l'amplitude de cette correction dépend du mélange des trous lourds et légers qui composent la fonction d'onde électronique.

L'étape complémentaire à la manipulation cohérente des spins électroniques, est la détection de leur état. Une technique appelée conversion spin-charge permet de corréler les états de spin aux états de charge. Ainsi, une mesure électrique de la charge d'une boîte quantique permet de connaitre l'état de spin. Plusieurs méthodes de détection ont déjà été démontrées expérimentalement. La première exploite la différence d'énergie entre les deux états de spin et une deuxième profite de la différence de taux tunnels des états de spin vers les électrodes métalliques. Dans le chapitre 4, ces différentes méthodes sont rappelées et je discute une autre méthode basée sur le couplage spin-orbite propre aux systèmes de trous des îlots de SiGe.

Les pompes à électrons sont couramment réalisées dans des systèmes nanométriques. La sélectivité en spin du taux tunnel évoqué au chapitre 4, permet d'envisager la réalisation d'une pompe électronique en manipulant l'état de spin d'une boîte quantique. La simple manipulation-rotation du spin permet de générer un courant à travers la nanostructure sans appliquer de tension source-drain. Durant ma thèse, j'ai fabriqué et étudié un tel système à partir de nanofils d'InAs/InP. Les détails de cette étude sont présentés dans le chapitre 5.

Enfin, le chapitre 6 est entièrement dédié aux nombreux efforts technologiques développés durant mon travail de thèse pour aller plus loin dans la réalisations de nanostructures complexes à partir de plusieurs îlots de SiGe connectés. Pour ce faire, j'ai du mettre au point un nouveau protocole technologique qui permet d'adresser individuellement plusieurs îlots et cela de manière contrôlée. Des géométries diverses et variées sont présentées ainsi que les enjeux scientifiques associés.

Conclusion

En plus des applications potentielles, les boites quantiques semi-conductrices sont des systèmes modèles pour étudier de nombreux phénomènes quantiques. Dans ce manuscrit de thèse, j'ai présenté des mesures expérimentales et des modèles qui ouvrent des perspectives nouvelles sur les potentialités de ces nanostructures pour le transport électronique quantique. Ces études ont principalement porté sur les nanocristaux de SiGe obtenus par croissance auto-assemblée pour lesquels un long temps de cohérence de spin est prédit. Mon travail a permis de décrire les effets de confinement électrostatique et révéler des effets de tunneling/cotunneling et d'explorer les divers phénomènes liés aux états de spin des porteurs de charge.

Durant ma thèse, j'ai pu mesurer le tenseur de Landé des trous dans des îlots de SiGe et montré qu'il est possible de moduler sa valeur par un champ électrique externe. L'analyse détaillée des résultats a montré que cet effet ne peut pas être lié à un gradient de concentration dans l'îlot. Nous avons alors proposé une interprétation nouvelle basée sur la prise en compte d'un terme correctif dans l'expression du facteur de Landé et généralement négligé dans la littérature.

Ces nanocristaux de SiGe permettent également d'envisager la manipulation des états de spin par un champ électrique radio-fréquence. Mon travail de thèse a permis de clarifier les conditions dans lesquelles il est possible d'utiliser ces boîtes quantiques en SiGe comme brique élementaire pour l'information quantique basée sur le codage des états de spins. Les estimations montrent qu'il doit être possible d'obtenir des temps de cohérence comparables à ceux obtenus dans les nanofils d'InSb.

Par ailleurs, en étudiant les processus de transfert électronique inélastique dans ces boîtes quantiques, j'ai pu montrer une asymétrie de conductance en fonction de l'état de spin. Cette observation nous a amené à proposer un protocole expérimental qui permet de fabriquer une pompe électronique d'une toute nouvelle nature. Pour des raisons de difficultés dans les processus de nanofabrication, j'ai réalisé cette pompe à partir de fils semi-conducteurs d'InAs/InP.

Enfin, j'ai développé une méthode originale de nanofabrication afin de pouvoir fabriquer à la demande des nanostructures incluant plusieurs îlots de SiGe auto-assemblés et donc aléatoirement dispersés sur une substrat de Silicium. Ces avancées technologiques ouvrent des perspectives pour l'ingénierie quantique basée sur ce genre de matériau qui est compatible avec les techniques de fabrication modernes en micro-nanoélectronique.

Contents

Introduction

Quantum mechanics displays all its exciting strangeness already by considering the Schrödinger equation in a one-dimensional square-well potential; tunneling events put this statement in evidence. To recreate this situation in a given material system is an inspiring playground and a big step towards taking control of quantum mechanisms. For instance, it is now possible to confine electrons in solid-state devices enabling a more efficient solar-cell technology.

Confining individual electron spins has in fact been suggested as a possible approach to the realization of a quantum computer. Each electron spin forms a natural two-level system encoding an elementary bit of quantum information (a so-called *spin qubit*). This proposal, by Loss and DiVincenzo [1], has contributed to the opening of an active research field referred to as *quantum spintronics*. Spin qubits rely on the fact that spin states can preserve their coherence on much longer time scales than charge (i.e. orbital) states.

A confinement potential can be created artificially in many different ways; producing constant magnetic fields and spatially inhomogeneous electric fields, applying oscillating electric fields, using conductive oxide layers, etc. To take advantage of the band-alignment of different semiconductors is among these. The relevant dimensions of the considered system should still be smaller than the phase coherence length of the confined particles in order that their quantum behaviour is preserved.

So far, most of the progress has been achieved using GaAs-based semiconductor heterostructures [2]. In such layered systems the motion of carriers is confined to a plane and further confinement is achieved by means of lithographic techniques, which allow lateral confinement to be achieved on a sub-100 nm length scale. In this way, quasi-zero-dimensional systems whose electronic states are completely quantized, i.e. *quantum dots* (QDs), can be devised.

Various time-resolved techniques involving high-frequency electrical signals have been developed to manipulate and read-out the spin state of confined electrons in GaAs QDs, and several years ago the first spin qubits were reported [2]. In GaAs-based QDs, however, the quantum coherence of electron spins is lost on relatively short time scales due to the hyperfine interaction with the nuclear spins (both Ga and As have non-zero nuclear spin). In spite of significant advances in controlling the nuclear polarization [3, 4], this problem remains unsolved.

In the past few years an increasing effort is concentrating on alternative material systems in which hyperfine interaction is naturally absent or at least very weak and, in principle, controllable by isotope purification.

While Si fulfills this requirement and it is the dominant material in modern microelectronics [5], it suffers from low mobility compared to III-V semiconductors, which obstructs its application for quantum spintronics. SiGe structures offer a way to circumvent this problem that is still compatible with standard silicon processes [2].

I have focused mainly on the study of the electronic properties of SiGe self-assembled islands, also called SiGe nanocrystals. This work, which condensates the main points of this study, is organized as follows; in the first chapter, I describe the basics of the growth of SiGe self-assembled islands and the properties of the quasi-zero-dimensional confinement potential that they define. Chapter 2 is devoted to the basics of electronic transport in these structures. Chapter 3 deals with the electric modulation of the hole g-factor in SiGe islands, which would enable a fast manipulation of the spin states. In Chapter 4 I present theoretical and experimental findings related to spin selectivity in SiGe QDs and Chapter 5 is dedicated to the realization of an electron pump in InAs nanowires based on this effect. Finally, Chapter 6 exhibits our progress towards the study of coupled SiGe QD devices.

---

[2] The mobility is enhanced as a function of the Ge concentration in SiGe layers [6].

Chapter 1

SiGe self-assembled nanostructures

Molecular Beam Epitaxy (MBE) is a growth technique by which a single crystalline film of a given material can be grown on a crystal substrate under ultra-high vacuum conditions. Among other material combinations, this technique enables the growth of crystalline Ge on a Si(001) wafer.

Si and Ge are semiconductors of the group IV, miscible over the entire composition range. $\mathrm{Si}_{1-x}\mathrm{Ge}_x$ alloys from $x = 0$ to $x = 1$ can thus be grown. Both Si and Ge have a diamond-like crystal structure, but their lattice constants (α) are different; $\alpha_{Si} = 5.43 \mathring{A}$ while $\alpha_{Ge} = 5.66 \mathring{A}$. Initially Ge grows on Si(001) in a layer-by-layer mode, but as the in-plane lattice-constant of Ge has to adjust that of Si, a biaxial stress is built up. After 3 or 4 monolayers, the accumulated strain is released either through the formation of dislocations or through the formation of crystalline 3D structures, usually called islands. This is the so-called Stranski-Krastanov growth mode [7, 8]. Schematic representations of the growth mode and the strain relaxation mechanism are shown in Fig.1.1 a) and b), respectively. Finally, these so-called *self-assembled* structures are capped with a thin Si layer of about 2 to 4 nm. This Si cap prevents the formation of Ge oxides, which are known to be highly soluble in water and thermally unstable.

The formed nanostructures can have a variety of sizes and shapes depending on the chosen growth parameters (see Fig.1.2) [9, 10]. Unless specifically mentioned, from now on I will focus on dome islands. These islands, while crystalline, have accessible dimensions for the current sample fabrication capabilities.

It has been shown that the position of these nanocrystals can be controlled by prepatterning the growth surface [14, 15]. An example of this prepatterned growth is shown in Fig.1.3. Potentially scalable, this material system could

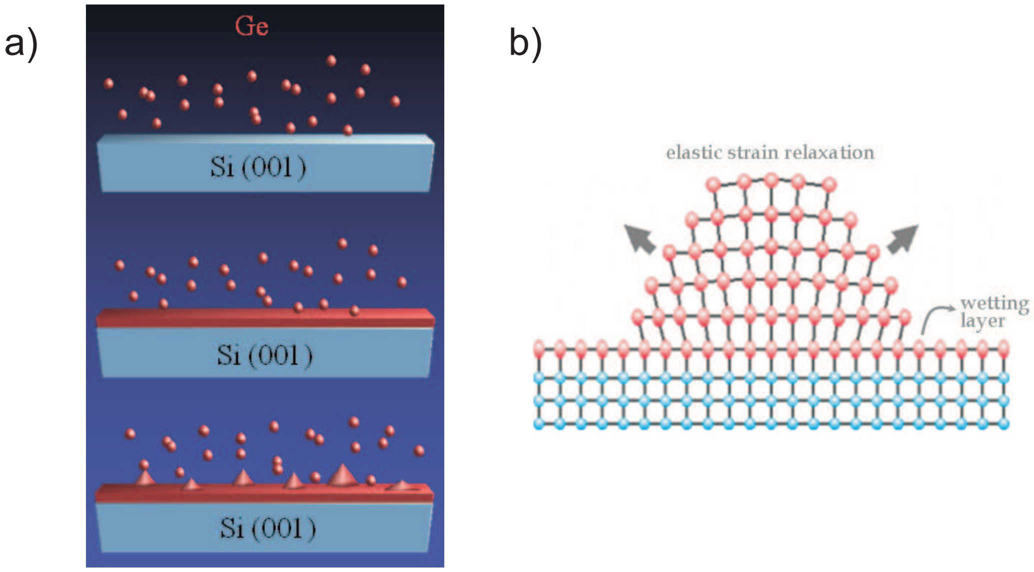

Figure 1.1: a) Schematic of the evolution of the growth of Ge islands on Si by means of the Stranski-Krastanov growth mode, from [11]. b) Schematic representation of the strain relaxation by formation of a 3D island. Taken from www.fkf.mpg.de/mbe/.

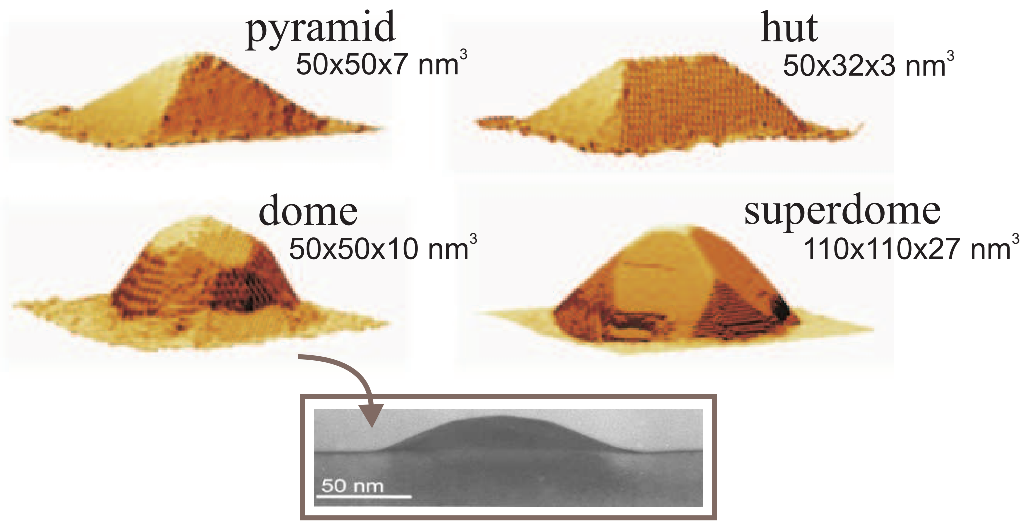

Figure 1.2: Three-dimensional Scanning Tunneling Micrographs (STM) of self-assembled SiGe nanocrystals with characteristic ‘pyramid’, ‘hut’, ‘dome’ and ‘superdome’ shapes. Taken from [11]. Inset: Cross sectional Transmission Electron Microscopy (TEM) image of a dome island. Taken from [12].

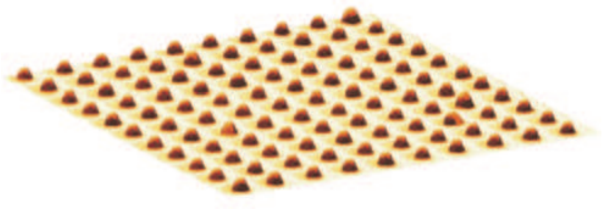

Figure 1.3: Atomic force micrograph (4.7 × 4.7) μm^2 illustrating a self-organized array of SiGe nanocrystals grown on a prepatterned silicon wafer [13].

be a platform for integrated circuits compatible with CMOS technology [16].

Properties of the confinement potential and the spin-orbit interaction in SiGe islands

Depending on the relative position of the conduction and the valence band of two semiconductor materials, type I and type II alignments are defined. It has been shown that a type II alignment is present for strained SiGe on Si [17]. In this case, the conduction and the valence band align in such a way that a confinement potential for holes is created. In Fig.1.4 a) (TOP) a SiGe dome island with a simplified compositional cross-section is represented together with its correspondent schematic band-alignment, Fig.1.4 a)(BOTTOM).

For SiGe the valence band varies linearly with the Ge content [18], which is a function of the crystal height (z) [19]. Figs.1.4 b) (TOP) and (BOTTOM) show the dependence along z of the Ge content of a dome island. To sum up, we can say that holes are confined in a quasi-one-dimensional potential with a shape that is given by the compositional gradient of the SiGe island.

Noteworthy, holes in the valence band have an orbital angular momentum $l = 1$. Given the multiplicity, $(2l + 1)$, this band is threefold degenerate (sixfold degenerate taking into account the spin). However, because of the confinement and compressive strain in the islands, this degeneracy is lifted giving rise to heavy-holes (HH) and light-holes (LH) branches, with projections of the orbital angular momentum $m = \pm 1$ and $m = 0$, respectively. In the QD, the orbital states consist of a mixture of HH and LH wave functions.

When spin-orbit (SO) interactions are considered, the orbital angular momentum couples to the spin degree of freedom $s = \frac{1}{2}$. The conserved magnitude is now the total angular momentum J that can take the values $J = \frac{3}{2}$ and $J = \frac{1}{2}$. Those corresponding to $J = \frac{3}{2}$ are the HH and LH bands, with $m = \pm\frac{3}{2}$ and $m = \pm\frac{1}{2}$ respectively. The so-called *split-off* band is the one corresponding to $J = \frac{1}{2}$ and its energy separation from the heavy- and light-hole bands, called *spin-orbit splitting* (Δ_{SO}), quantifies the strength of the SO interaction. Fig.1.5 illustrates this split-off band as well as the HH and a LH branches, whose Gamma-point degeneracy is lifted by strain and confinement. It should be noted that the effective masses of confined holes are dependent on directions. The effective mass of HH branches along the quantization axis is larger than that of LH branches, while the effective mass of HH branches on the xy-plane is smaller than that of LH branches.

The SO interaction has become of central interest for the possibility to perform electrically-driven spin manipulation. Golovach et al. [21] have pro-

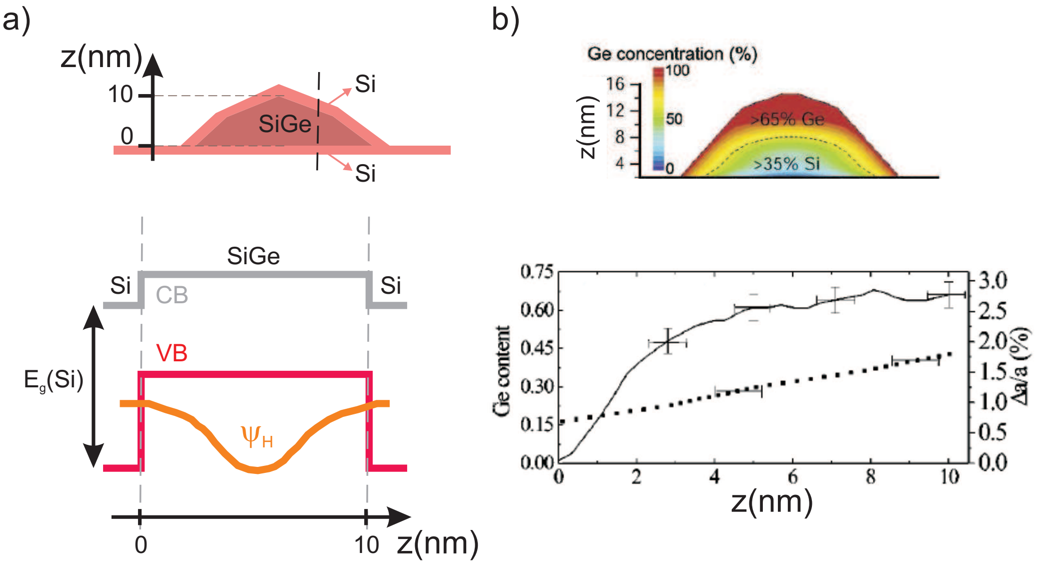

Figure 1.4: a) TOP: scheme of a nanostructure with a simplified compositional cross-section. BOTTOM: corresponding conduction band (CB) and valence band (VB) alignment scheme, where $E_g(Si)$ is the Si band-gap and Ψ_h represents the localization of holes. b) TOP: Chemical composition map of dome islands [20]. BOTTOM: Ge content (line) of these islands as a function of z. The lattice parameter relaxation with respect to the lattice parameter of Si, $\Delta a/a$, is also displayed (points). Taken from ref.[19].

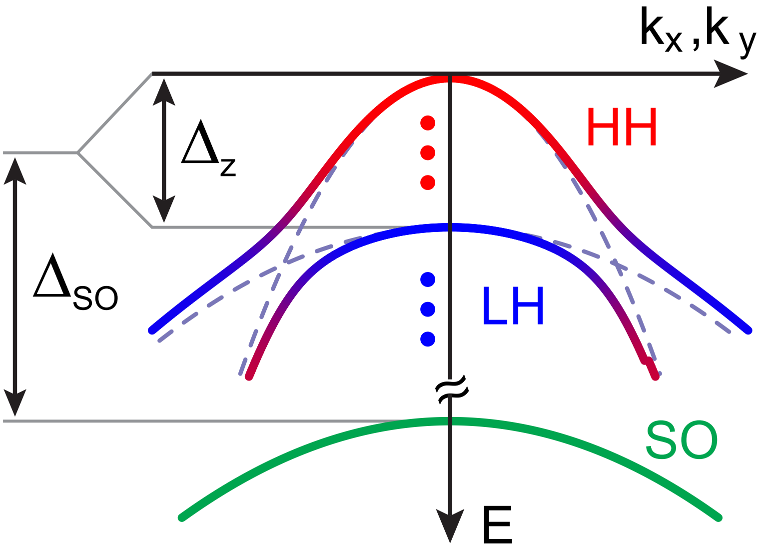

Figure 1.5: Qualitative band diagram of a Ge-rich SiGe quantum well, with E the energy and k_x and k_y the plane wave vectors. The HH and a LH branches are lifted by Δ_z due to the presence of strain and confinement and they anticross at finite k_x or k_y. A split-off band appears as a result of the SO interaction in the valence band, quantified by Δ_{SO}.

posed an all-electrical approach, called *electric-dipole spin resonance* (EDSR), that was successfully used for spin rotations of electrons in QDs [22, 23].

In the case of Si, $\Delta_{SO} = 44$ meV, whereas for Ge $\Delta_{SO} = 290$ meV. Therefore, SO effects in Si quantum structures are rather small and SiGe appears again as a better candidate for quantum spintronics. Furthermore, valence band states have a stronger SO coupling than the conduction band states, which makes hole confinement very promising for an efficient electric manipulation of the spin states. To conclude, holes confined in SiGe structures have very propitious properties for the realization of fast spin qubits.

Chapter 2

Single quantum dot devices based on SiGe self-assembled nanostructures

In order to perform a transport-spectroscopy study of the electronic properties of SiGe nanocrystals, metal electrodes serving as *source* and *drain* contacts are required. These contacts are metal-like reservoirs to which an external bias voltage V_{sd} can be applied. By measuring the current flow through this device, the electronic properties of carriers in the crystal can be explored. Fig.2.1 a) illustrates these kind of devices based on SiGe islands. In addition, a *gate voltage* (V_g), a voltage applied to an additional metallic electrode, gives the possibility to electrically tune the energy levels and hence influence the current that flows through a device.

In order to have a clear picture of the processes involved in the transport of carriers, the literature often refers to schemes like the one shown in Fig.2.1 b). In this scheme, the source and drain contacts are symbolized by their electrochemical potentials μ_s and μ_d, with $|\mu_s - \mu_d| = eV_{sd}$ where e is the absolute value of the elementary charge. A one-dimensional square well potential represents the SiGe nanocrystal. As discussed in the previous chapter, this is a fairly adequate picture although the quasi-zero-dimensional confinement that defines the QD in the crystal is created in the valence band and consequently, the carriers are holes instead of electrons.

2.1 Device fabrication

The nanodevices were fabricated using electron-beam (ebeam) lithography. The basic process flow for this techniques is illustrated in Fig.2.2. The first

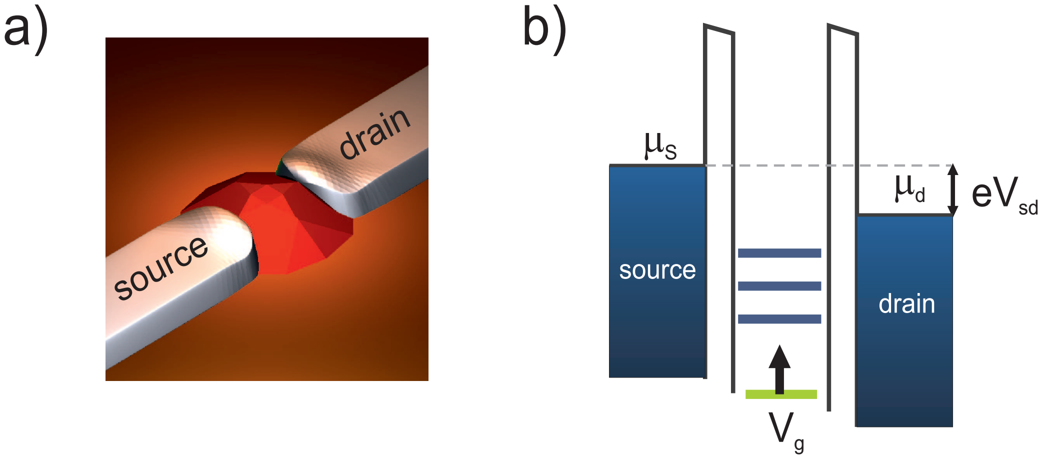

Figure 2.1: a) Schematics of a SiGe nanocrystal based device. b) Schematics of a device, μ_s and μ_d being the electrochemical potentials of the metallic contacts and V_{sd}, the bias voltage between them. The gate voltage V_g regulates the current flow through the device by electrically tuning the quantized states inside the crystal.

step is to deposit an organic resist material onto a substrate by means of a spinner. The resist is then selectively exposed to an electron beam. The beam induces changes in the chemical structure of the irradiated polymer, such that in a following step the irradiated portion dissolves when immersed in a developer (positive resist). Once the pattern is defined on the substrate, a given metal is evaporated and it covers the resist profile. Finally, the resist is removed from the substrate through a so-called *lift-off* process and just the metal deposited on the pattern remains.

Fabrication of SiGe nanodevices

Inspired by recent work on self-assembled InAs nanocrystals [24, 25, 26], a technique to contact single SiGe islands has been developed by the group. It starts from a wafer of SiGe nanocrystals grown on a non-standard silicon-on-insulator (SOI) substrate, which consists of an undoped silicon overlayer, a SiO_2 insulating layer, and a degenerately doped silicon substrate that serves as a back-gate [1](Fig.2.3 a)).

---

[1] These substrates were fabricated by F. Fournel in CEA, LETI, from commercial SOI wafers. These commercial wafers were thermally oxidized and bonded to a heavily doped Si wafer. By grinding and selective chemical etching, non-standard SOI substrate having a 40-nm-thick Si upper layer, a 65-nm-thick oxide layer and a degenerately doped Si

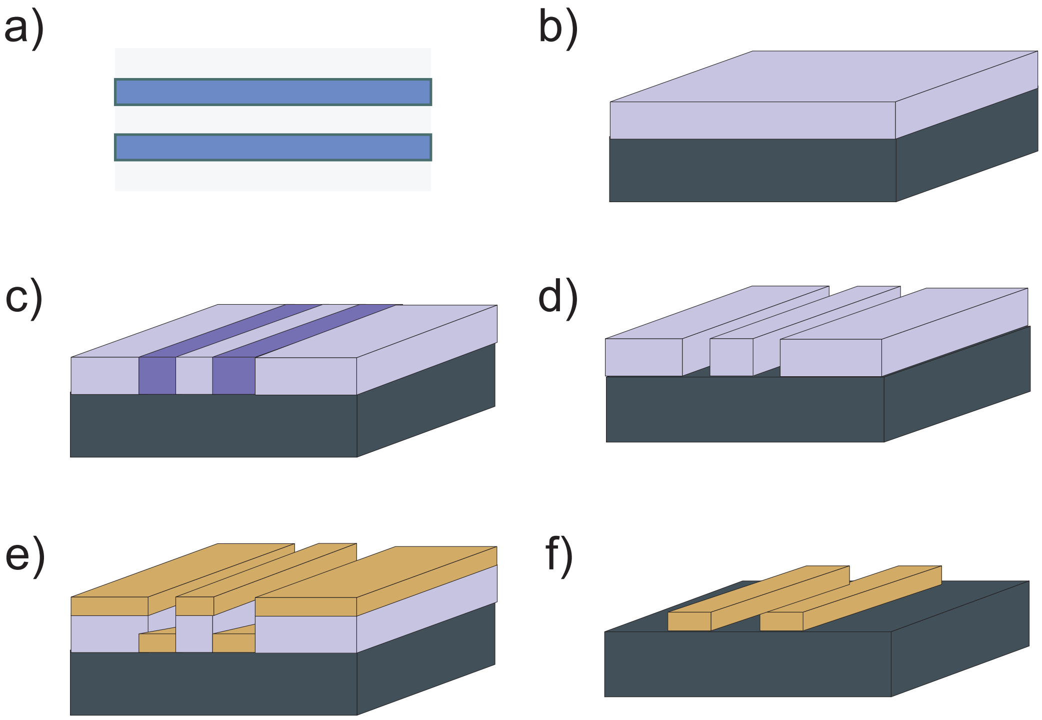

Figure 2.2: Nanofabrication technique based on ebeam lithography; a) design of the two lines which represent the desired pattern to be transferred, b) substrate coated with a resist material, c) the resist is selectively exposed to the electron beam, d) after development the exposed parts of the resist dissolve, e) a metal is evaporated, f) the resist and the residual metal are removed by immersing the substrate in a solvent (lift-off process).

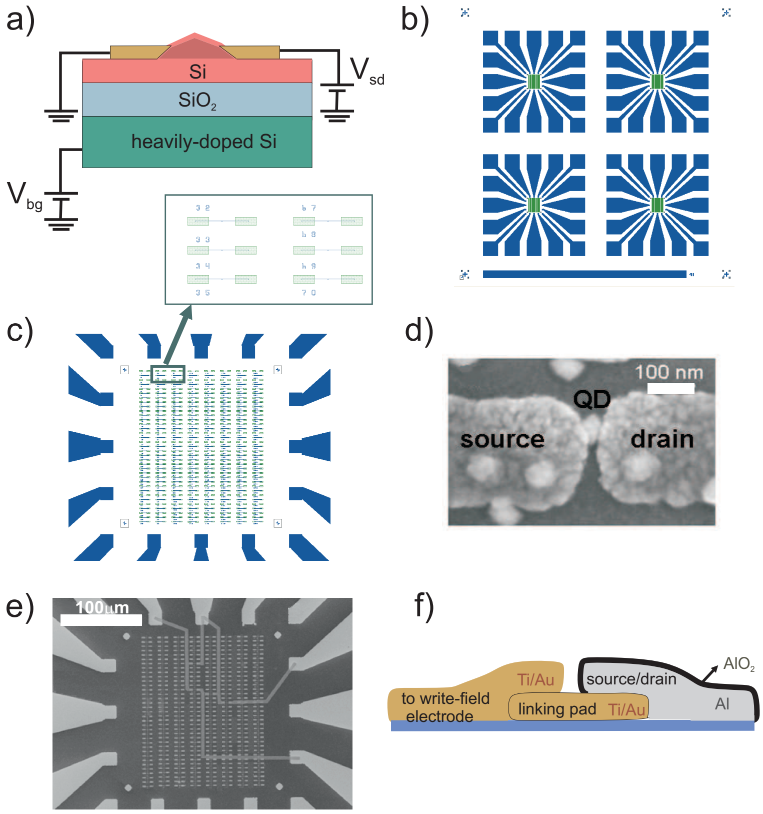

Figure 2.3: a) Scheme of a contacted SiGe self-assembled nanostructure grown on a non-standard SOI wafer. This wafer consists of a thin Si layer, a SiO_2 layer of about 65 nm and a heavily doped silicon substrate. To this doped substrate, a voltage V_{bg} can be applied in order to gate the SiGe devices. b) Pattern that defines the write-fields and the alignment crosses on the substrate in the first step of ebeam lithography. c) Design of the source and drain contacts distributed all over the inner area of a particular write-field in the second step of ebeam lithography. Numbers are added to the side of each pair of contacts in order to be able to address later those which contact a SiGe island. d) SEM image of source and drain contacts after exposure, etching and metal deposition. An island is contacted by these leads. e) The third step of ebeam lithography connects those pairs of electrodes that contact a SiGe crystal to the write field electrodes. f) Ti/Au linking pads used to contact the aluminium leads from its bottom surface in order to get a good electrical contact that is otherwise prevented by the AlO$_2$ formation. These linking pads are afterwards connected to the write field electrodes.

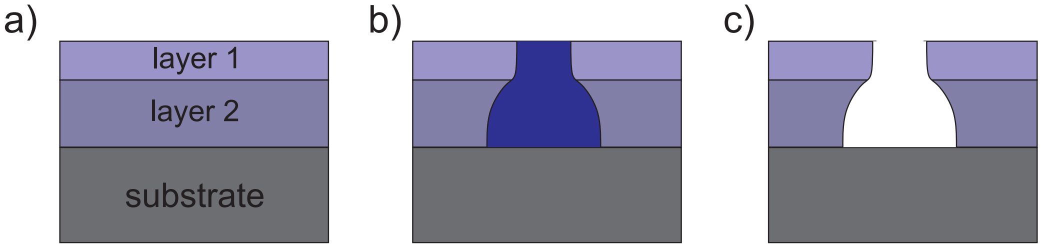

Figure 2.4: a) Double layer resist spun on a substrate, the molecular weight of the top layer being higher than the one of the bottom layer. b) Same bilayer after exposure. c) Same bilayer after exposure and development. This resist profile is known as undercut.

Following the procedure described in Fig.2.2, a first step of ebeam lithography is done on this wafer in order to define the pattern shown in Fig.2.3 b). It consists of a set of alignment crosses and 4 *write-fields*, each of them with 16 electrodes that shrink until they frame an area of $250 \times 250\ \mu\text{m}^2$. The source and drain contacts are defined in this area, shown in Fig.2.3 c), in a second step of ebeam lithography. A big number of contacts increases the probabilities to actually catch a SiGe island in between.

This second step of ebeam lithography is not as trivial as the first one; firstly, because it will define the contact surface of the metal with the semiconductor island and secondly, because the source and drain contacts should be separated by a ~ 20 nm gap in order to contact a SiGe island. Therefore, an exhaustive list of the parameters chosen for this fabrication step is essential, and thus it is displayed below.

1. Resist

   A bilayer technique, in which a high molecular weight resist is spun on top of a low molecular weight resist was used. The sensitivity of a resist is related to its molecular weight; at low molecular weights, high sensitivities, which means that lower doses of radiation will be needed in order to secure a proper exposure. Consequently, the effective dose of radiation delivered to the bottom layer (more sensitive) will be bigger than the one delivered to the top layer (less sensitive). This difference in sensitivity results, after development, in a particular resist profile called *undercut* (see Fig.2.4). This resist profile makes the lift-off process easier, especially for narrow gaps.

---

substrate, were obtained.

The bottom layer was chosen to be PMMA 4% 200K and the top layer, PMMA 2% 950K. The top layer is most critical, as it is the one that limits the resolution. PMMA 2% was chosen for its capability of producing reduced thickness layers that allowed us to achieve the resolution needed in the pattern writing.

In order to guarantee a total resist thickness of about 200 nm, both resist layers were spin coated for 30 s at a speed of 6000 rpm and an acceleration of 2000 rpm/s. Then, they were heated, one at the time, at $180^\circ C$ for 5 min in order to secure the evaporation of the solvents that are present in resist materials.

2. Exposure

   Ebeam lithography can be performed with relatively simple modification to a conventional scanning electron microscope (SEM) through computer control of the position of the beam. We had access to a equipment of this kind, called modified SEM, that is capable of defining features with critical dimensions of the order of 100 nm and that has an alignment precision, with respect to a set of predefined crosses, in the order of 250 nm. Noteworthy, this value varies significantly with the chosen write-field area ($(250 \times 250)\ \mu\text{m}^2$ in this case). The acceleration voltage was 20 kV and the current of the electron beam 15 pA.

3. Development

   To develop the exposed resist, a 30 s dip in a solution MIBK/IPA $1:3$ followed by a 1 min rinse in IPA was performed. MIBK (Methyl Isobutyl Ketone) itself provides the ingredient necessary for solubility control and swelling of the resist, while the IPA (Propan-2-ol) stops the development. Solutions containing a higher amount of IPA are best for high resolution fabrication.

4. Etching

   As discussed in the previous chapter, the SiGe nanocrystals are capped with a thin Si layer of 2 to 4 nm. Once exposed to air under ambient conditions, a very shallow layer (approximately 1 nm) of so-called native oxide is formed on the surface. This silicon dioxide represents a huge tunnel barrier for carriers and, consequently, it should be removed in order that current can flow through the device. This is the reason why a 10 s wet etching in BHF (Buffered Hydrofluoric acid) followed by a short rinse in deionized water was performed before the metal deposition.

BHF refers to a mixture of a buffering agent, such as ammonium fluoride (NH_4F), and hydrofluoric acid (HF). Concentrated HF (typically 49% HF in water) etches silicon dioxide too quickly for good process control. For that reason, BHF is commonly used for more controllable etching, as it can keep the etch rate low and constant.

This solution etches the native silicon oxide in a few seconds and it is self-limited, i.e. once the silicon oxide is etched away, due to its high selectivity, the Si left in the capping layer ($\sim$ 1 to 3 nm) is not attacked. In addition, this Si layer becomes hydrogen passivated, which means that its oxidation when exposed again to air is prevented for a limited time.

5. Metal deposition

   While the capping layer is still hydrogen passivated, the deposition of a metallic layer should take place. This is done with an electron beam evaporator, with a base pressure of 1×10^{-8} mTorr.

   The electron beam is generated by thermal emission from a heated tungsten filament. A crucible containing the material to be deposited is held at a positive potential relative to this filament. To avoid chemical interactions between the filament and the crucible material, the filament is kept out of sight. Magnetic and electric fields are then employed to direct and steer the electron beam from its source to the crucible location. One can choose between different materials to be evaporated by rotating the crucible selector.

   In order to improve the uniformity of the evaporated layer and to avoid the overheating of the resist, the substrate stage is located far away from the source and it rotates during deposition.

   Under these conditions, a layer of 30 nm of Al is deposited to form the source and drain contacts.

6. Lift-off

   The remaining resist is lifted in hot acetone (40°C) for 5 min. Before removing the sample from the acetone bath, the metal layer is peeled off by gently forcing with a pipette the liquid towards the substrate surface. Finally, the sample is sprayed with IPA and dried with nitrogen.

Once this lithographic process is concluded, the following step is the SEM imaging of each write-field looking for those source and drain leads that are actually contacting a SiGe island (see Fig.2.3 d)). This SEM imaging is performed at 5 kV.

A final ebeam lithography step is then needed in order to contact these source and drain leads to the write-field electrodes. This lithographic step is relatively simple, a SEM image of a write-field after the corresponding development and metal deposition is shown in Fig.2.3 e).

Noteworthy, some metals that are used for defining the source and drain contacts oxidise under ambient conditions. Aluminium is one of these and to remove the aluminium oxide layer is known to be a hard task. A solution to this problem is to add an extra step of ebeam lithography, previous to the one in which source and drain are defined. In this step, some small areas covered by a Ti/Au layer are defined. Ti is just an adhesion layer and Au, as it does not oxidise, is able to make a good contact to an aluminium layer deposited on top, i.e. the source-drain leads. These areas, called linking pads, will be the ones connected to the write-field electrodes afterwards. Fig.2.3 f) illustrates this idea. Table 2.1 summarizes the fabrication steps described above.

Table 2.1: Process flow

1.	Alignment crosses and write field electrodes	Ti/Au 10/65 nm + lift off	see Fig.2.3 b)
2. (optional)	Linking pads	Ti/Au 2/8 nm + lift off	
3.	Source and drain leads	Al 30 nm + lift off	see Fig. 2.3 c)
4.	SEM imaging		see Fig. 2.3 d)
5.	Connection of source and drain leads to write field electrodes	Ti/Au 10/70 nm + lift off	see Fig. 2.3 e)

The very last step of the sample fabrication is the *wire bonding*, a technique that allows us to electrically connect the fabricated chip with a printed circuit board (PCB). The wire bonding technique used in our case is the one called *Al wedge bonding*. It involves a very fine aluminium wire (*bonding wire*)

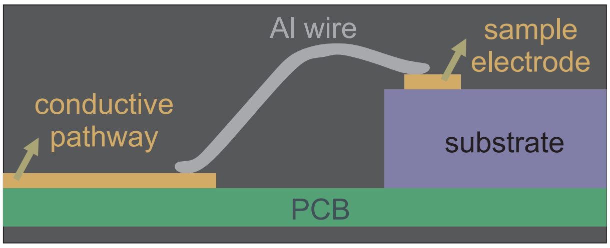

Figure 2.5: Al wedge bonding technique. Two metals are pressed together using a specific amount of pressure and are friction welded with an ultrasonic signal.

that is brought in contact with the surfaces to be connected (see Fig.2.5). An ultrasonic energy is applied to the wire for a specific duration while being held down by a specific amount of force, forming the wedge bond between the wire and the sample electrode. The wire is then positioned above the corresponding pad in the PCB, against which it is again pressed. The wire is finally broken off by clamping.

In Figs.2.6 a) and b), the fabricated sample assembled to a PCB is shown. In the PCB, the copper conductive lines can be clearly distinguished. 24 conductive lines are available and they are divided in two groups, each of them soldered to a 12 pin connector. Two pairs of these connectors are accessible. One of these pairs is short-circuited to a ground plane in order to avoid undesired current flow during bonding. This ground plane is removed once the sample is plugged-in the measurement setup, which provides a fixed potential to the sample leads.

2.2 Low-temperature setups

At room temperature, the upper silicon layer of the SOI substrate introduces a significant parallel conduction path. A temperature below $\sim$ 100 K is needed to suppress this parallel conduction path, so that uniquely transport through the SiGe QD can be addressed.

In addition, in order to be able to resolve the quantized levels in a QD, their energy separation should exceed the thermal broadening of the metal leads. An energy spacing of the quantized levels of a few tens of μeV corresponds to a characteristic temperature of a few tenths of a degree Kelvin. Consequently, when the temperature is increased beyond this value, all quantum effects are smeared out.

In this thesis, three types of fridges were used in order to cool-down the

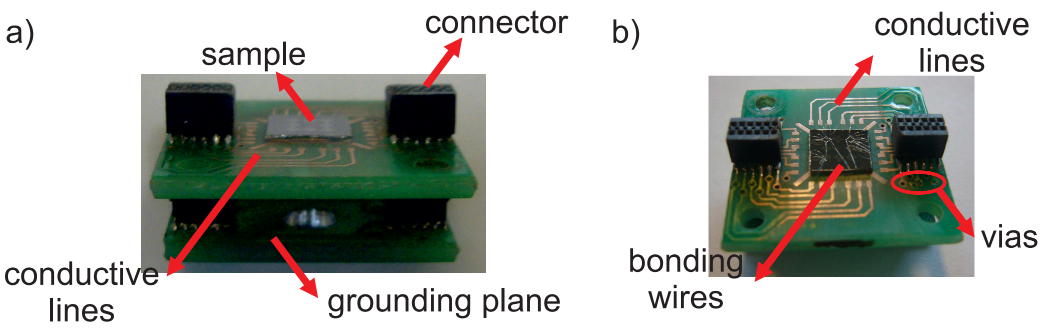

Figure 2.6: Chip carrier. a) The fabricated sample, the conductive lines to the connectors and the ground plane is observed. b) The through-hole paths to the other surface (*vias*) as well as the bonding wires can be distinguished in this picture.

samples. Each of them with a different base temperature and therefore, suitable for different purposes.

1. 4 K dip-stick

   It consists of a stainless steel stick provided with measurement wires (12 constantan twisted pairs) ending on a 24-terminal sample holder at the bottom-edge of the stick. This stick is inserted in a can which is pumped down for a few minutes. Then, some He gas is allowed in and the can is inserted in a liquid He dewar. The He inside the can serves as *exchange gas*, allowing thus the sample to thermalize down to about 4 K.

   This technique was used for fast measurements in which the goal was mainly to estimate the contact resistance of the devices. The thermal broadening prevents a precise characterization of the discrete energy levels.

2. ^{3}He refrigerator

   ^{4}He, the most common isotope of helium, boils at 4.22 K at ambient pressure. However, the boiling point reduces with a pressure drop. Therefore, temperatures of 1.5 K are obtained by pumping on a small container of liquid ^{4}He (called 1*K pot*) that is continually replenished with helium of a main bath.

   At this temperature, by pumping on a ^{3}He pot, temperatures of the order of 250 mK can be achieved. ^{3}He is very rare, and therefore expensive, so it is handled in a closed system.

To mount the sample in such a setup is relatively easy and fast, as the procedure is equivalent to the one followed for the 4 K dip-stick. The main difference is that once the system is inside the liquid He dewar and it is thermalized to 4 K, the exchange gas needs to be removed in order that the ^{4}He and ^{3}He circuits are able to cool the system down to base temperature.

3. dilution refrigerator

   A dilution refrigerator is a very sophisticated system which profits from a spontaneous phase separation of a mixture of ^{4}He and ^{3}He to reach temperatures in the order of tens of mK. Its operation details are out of the scope of this work.

   The base temperature reached by this system gives access to the study of many subtle quantum effects. On the counterpart, a few days are required to put the fridge in operation.

2.3 Tunneling and cotunneling spectroscopy

2.3.1 Basics of charge transport

As already discussed, in these SiGe devices the confinement of carriers is imposed in all three spatial directions, resulting in a discrete spectrum of energy levels as in an atom or molecule.

In addition, when a charge carrier is transferred from one of the leads to the QD, the electrostatic potential of the dot changes, leading to the *single-electron tunneling* phenomenon described below.

For an ideal conductor with a capacitance C, the electrostatic potential (V) due to charge (Q) on an ideal conductor is given by the expression $V = Q/C$. If the conductor has macroscopic size, the change in potential energy associated with the addition (or removal) of an elementary charge is hardly noticeable. However, the capacitances of nanostructures can be so small that this change in potential energy may be greater than the thermal energy, k_BT, particularly at low temperatures. Such large changes in the electrostatic energy due to a single charge, result in a gap in the energy spectrum at the Fermi energy. This effect is known as *Coulomb blockade* and it inhibits the tunneling of carriers until the energy gap or *charging energy* (E_c) is overcome through an applied voltage. With C the sum of the capacitances between the dot and its gate and leads, $E_c = \frac{e^2}{C}$.

The total ground-state energy in a dot of N carriers is then given by the sum of the filled single-particle energy states and the electrostatic energy due to its total charge eN. The difference in total energy between two consecutive charge states with N and $N-1$ carriers defines the electrochemical potential, μ_N, for the $N-$electron ground state.

The electrochemical potential is the most convenient quantity for describing tunneling processes. For a bias voltage V_{sd} across the dot, charge transport is allowed whenever μ_N lays within the energy window $|\mu_s - \mu_d| = eV_{sd}$. In this case, transport occurs by single-electron tunneling events with the dot occupation varying between $N-1$ and N carriers. If μ^*_{N-1}, the electrochemical potential for an excited state for $N-1$ carriers, also lays within the bias window, transport through this extra channel will also be observed.

The condition $\mu_s > \mu_N > \mu_d$ required for the onset of single-electron tunneling can be achieved either by increasing V_{sd} (see Figs.2.7 a)-c)) or by varying the electrostatic potential of the dot with a gate voltage (see Figs.2.8 a)-c)). Each channel brought into the bias window results in a step in the measured current I, and therefore, a peak in differential conductance $dI/dV_{sd} \equiv G$, as illustrated in Fig.2.7 d).

Fig.2.8 d) shows the diamond-shaped diagram obtained when dI/dV_{sd} is monitored while sweeping V_{sd} and stepping V_g [2]. This is the *stability diagram* of the device, where the area inside the diamonds corresponds to a Coulomb blockaded region in which the amount of charges on the dot is fixed. In the constant interaction model [2], the height in eV_{sd} of these diamonds is defined as the *addition energy* (E_{add}) and it consists of a purely electrostatic part (E_c) plus the energy spacing between two discrete quantum levels ($\Delta\varepsilon$). $\Delta\varepsilon$ can be zero if consecutive carriers are added to the same spin-degenerate level. This is the reason why the stability diagram of QDs with well-separated spin-degenerate levels consists of a regular sequence of large and small Coulomb diamonds corresponding to even and odd filling, respectively.

The inset of Fig.2.8 d) exhibits the case in which, by moving the electrochemical potential ladder, a transport channel can be activated even at a very small bias. This occurs at the so-called *degenerate points*, found at the crossing of two diamond regions.

Until now, we have treated the tunneling to lowest order in perturbation theory, i.e. just *direct tunneling* processes were described. However, in the regime of Coulomb blockade, higher-order processes may become important when the resistances of the tunnel junctions begin to approach e^2/h, where h is Planck's constant [27].

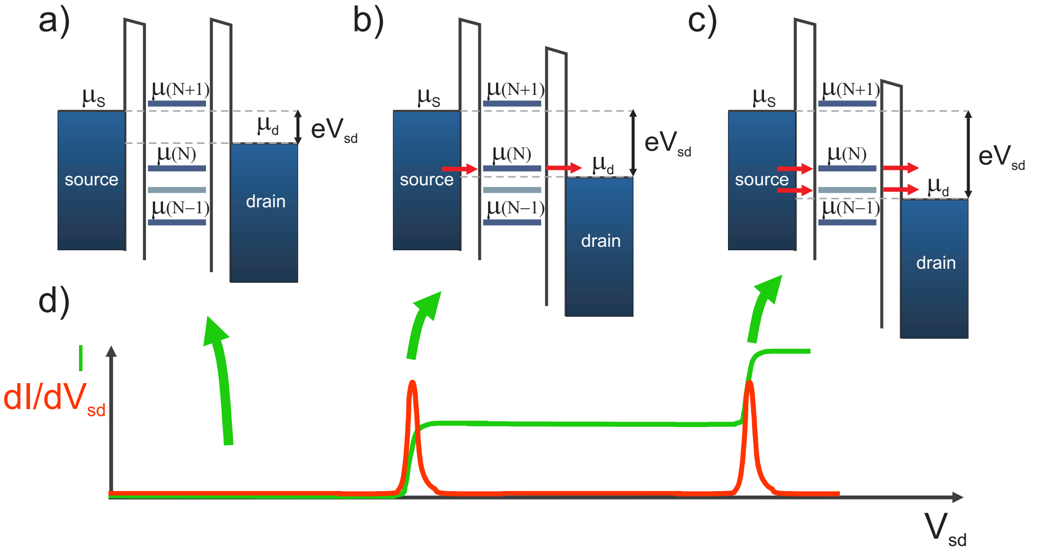

Figure 2.7: Schematic diagrams of the electrochemical potential levels for different bias voltages. The level in gray corresponds to a channel involving an excited state for $N-1$ carriers. a) No electrochemical potential level of the dot falls within the bias window (eV_{sd}) set by μ_s and μ_d. The charge number in the island is then fixed at N. b) $\mu(N)$ is in the bias window, transport can take place through this channel and as a consequence, the amount of charge carriers in the dot alternates between N and $N-1$. c) The bias window is big enough to allow transport through two channels; one of them involves ground states and the other, a ground state and an excited state. d) Current flow through the device (I) and differential conductance (dI/dV_{sd}) for each case represented in a), b) and c). A channel which is open for transport appears as a step in the measured current and as a peak in differential conductance.

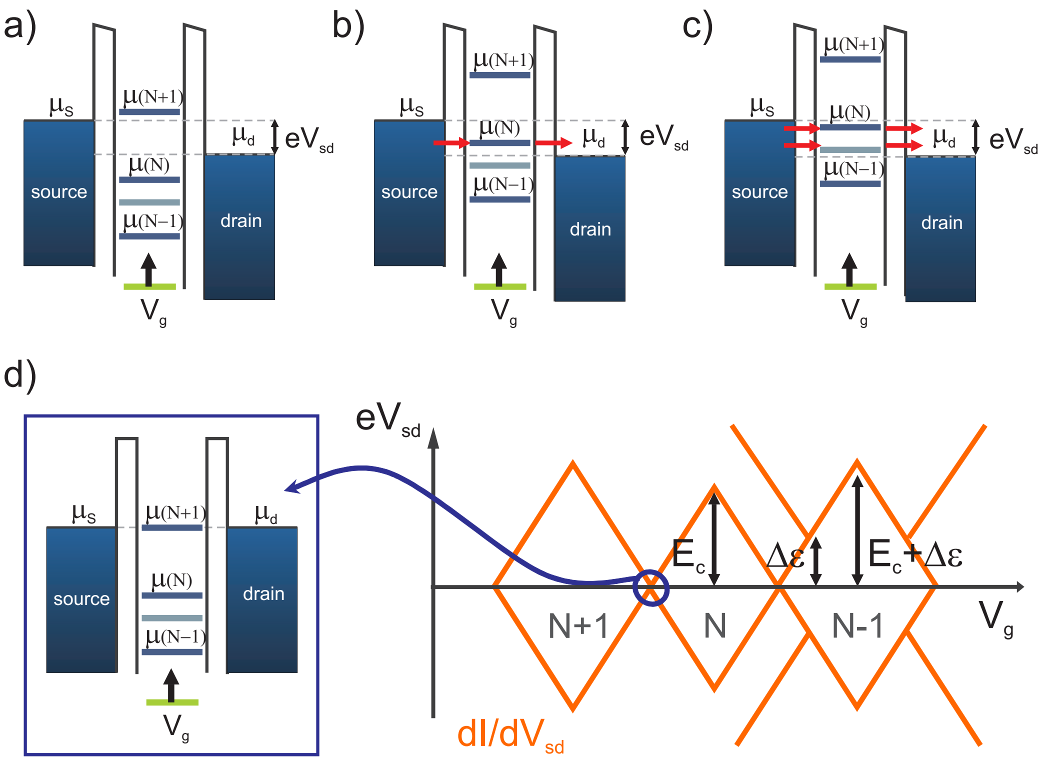

Figure 2.8: Schematic diagrams of the electrochemical potential levels for different gate voltages (V_g). The level in gray represents a transition to an excited state for $N-1$ carriers. The cases a), b) and c) are analogous to the ones on Fig.2.7 with the difference that the bias window is kept fixed and the electrochemical potential ladder is moved by a positive voltage applied to the gate. d) Diamond-shaped stability diagram. The differential conductance is displayed as a function of V_g and V_{sd}. The charging energy E_c plus the energy spacing between levels $\Delta\varepsilon$ is needed to activate the transport through the dot. $\Delta\varepsilon$ can be zero when a second carrier is added to a spin-degenerate level. This case is illustrated by the diamond corresponding to N charges. The diamond region for $N-1$ exhibits lines representing transport through the excited state. It is important to remark that in most of the experiments discussed in this thesis, the charge carriers are holes and consequently, a positive variation of a gate voltage will lead to the depletion of the QD. Inset: Zero-bias transport takes place at the degenerate points, where an electrochemical potential level aligns with the electrochemical potential of the leads.

2.3.2 Elastic and inelastic cotunneling processes

In a first order process, a particle cannot tunnel from the leads to the dot when biased in the Coulomb blockade regime due to conservation of energy. However, higher order processes allow the transfer of a charge carrier from the left lead to the right lead (or vice versa) via a virtual state in the island.

These processes may be either *elastic* or *inelastic*. Elastic cotunneling is the dominant off-resonance process at low bias. It gives rise to current inside the Coulomb diamond (light grey region in Fig.2.9 a)). The corresponding two-electron process (Fig.2.9 b)) transfers one carrier from the left to the right lead, thereby leaving the dot in the ground state.

Similar two-electron processes can occur which drive the dot into an excited state. For instance, a carrier can leave the dot from the ground state to the lowest Fermi sea, while another carrier from the highest Fermi sea tunnels into the excited state (see Fig.2.9 c)). Although this type of process is called inelastic [28], the total electron energy is conserved. The on-site excitation is created at the expense of the energy drop eV_{sd}. To first approximation, the onset of inelastic cotunneling yields a step in dI/dV_{sd} [29], as depicted in Fig.2.9 a).

2.4 First hybrid devices on SiGe self-assembled quantum dots

A big advantage of self-assembled semiconductor QD is that metal leads can be deposited directly on top of the nanostructure, allowing thus to explore different types of metals as contacts. A variety of *hybrid* devices can be envisioned, which combine metal properties, as superconductivity or ferromagnetism, with the microscopic properties of the QD.

The first low-temperature transport measurements on SiGe self-assembled QDs were performed and published by the group [13]. The scheme of the device is the one shown in Fig.2.3 a). Single-hole tunneling was observed and discrete energy spectra with $\Delta\varepsilon$ up to a few meV were reported (see Fig.2.10). The measurements were taken at a base temperature of 15 mK and the islands were contacted by Al leads, though devices with Ti/Au and Pt contacts have also been tested. Very low contact resistances were found in the latter case.

So far it has not been possible to deplete the SiGe islands. The reason for this is that the gate voltage also influences the capacitance between the dot and its leads, leading to different coupling regimes. When a large positive gate voltage is applied in order to deplete the QD, the coupling to the leads

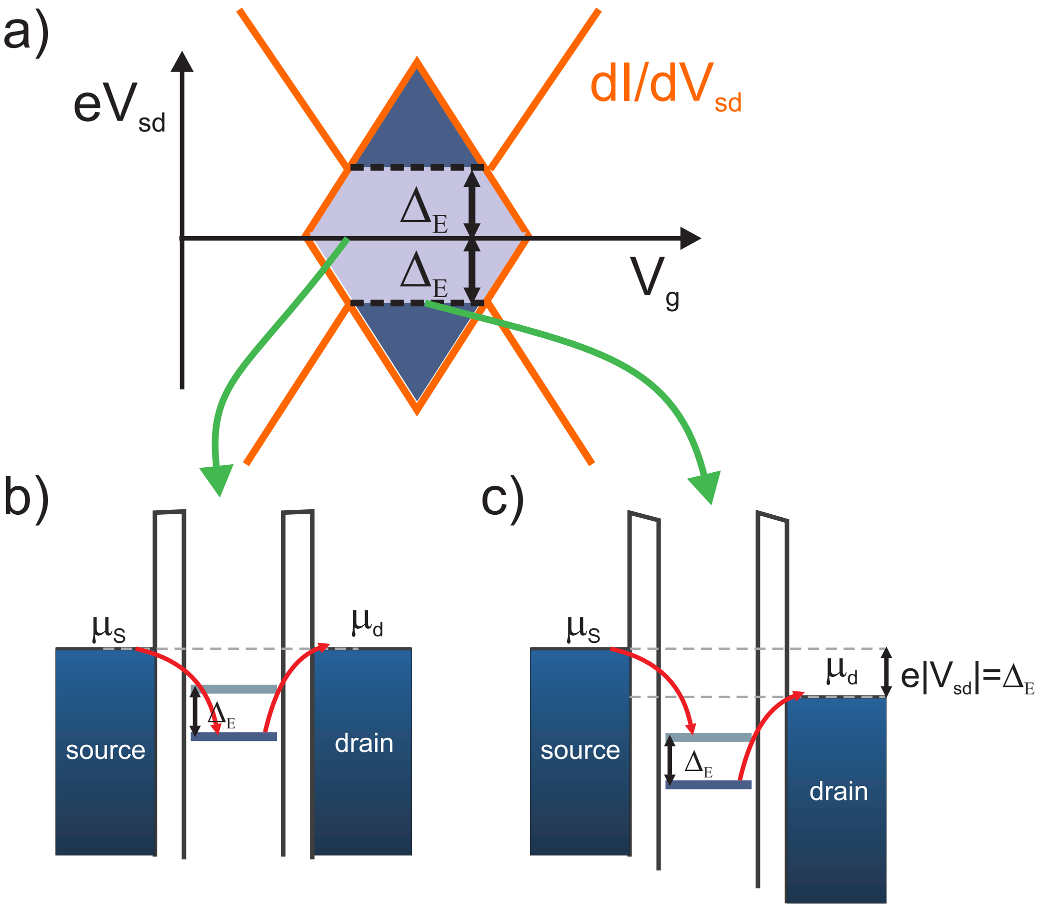

Figure 2.9: a) Illustration of a Coulomb diamond. In the light-blue area, conduction is due to elastic cotunneling via virtual events as shown in b). For $eV_{sd} \geq \Delta_E$, inelastic processes, illustrated in c), increase the cotunneling current (dark-blue areas). Δ_E is the energy spacing between the ground state and the first excited state, which in b) and c) are represented by blue and grey lines, respectively.

becomes very weak. As a consequence, it is not possible to conclude whether the unmeasurable current results from the depletion of the QD or from a very low tunneling rate. The effect of the gate voltage on the capacitance between the nanostructure and the metal contacts can be observed in Fig.2.10, where an increasing size of the diamonds towards positive voltages evidences mainly an increasing E_c and thus, a decreasing C_{eq}.

The last three diamonds in Fig.2.10 show size alternation, implying that the N^{th} carrier is a $s = \frac{1}{2}$ particle added to a spin-degenerate level, as a smaller E_{add} is observed in this case. Noteworthy, spectroscopy on dots containing more than two charge carriers has shown important deviations from an alternating spin filling scheme [30, 31].

For these SiGe self-assembled islands, strong spin-orbit coupling and resonant supercurrent transport have been reported in [13] among other spin-related phenomena.

2.5 Hole g-factor measurements in SiGe self-assembled nanostructures

When an external magnetic field $\vec{B}$ is applied, additional lines in dI/dV_{sd} appear around those diamonds that correspond to an odd number of confined charges. These additional lines result from the splitting of the energy levels caused by the lifting of the spin degeneracy in the presence of a $\vec{B}$. The energy difference between the split levels, the so-called *Zeeman* energy, is given by

$$\Delta E_z = \|\mathbf{g}\mu_B \vec{B}\|, \tag{2.1}$$

where μ_B is Bohr's magneton and $\mathbf{g}$ is the *g-factor* tensor. This tensor is related to the electronic structure of the system. Therefore, the g-factor depends on many factors, among which we find the spin-orbit coupling [32] and the confinement potential [33, 34].

In absence of magnetic field, the ground state of a dot with an even occupation has an integer spin, S. In the case of well separated levels, the ground state is a spin singlet ($S = 0$), $|S\rangle = (|\uparrow\downarrow\rangle - |\downarrow\uparrow\rangle)/\sqrt{2}$ [35]. In this case, the highest occupied orbital is filled with two electrons with opposite spins.

The first excited states are the spin triplets ($S = 1$), where one charge is promoted to the first available empty orbital. The three triplet states are degenerate at zero magnetic field, but the Zeeman energy shift under finite magnetic field is different because their spin projection differs, $S_z = +1$

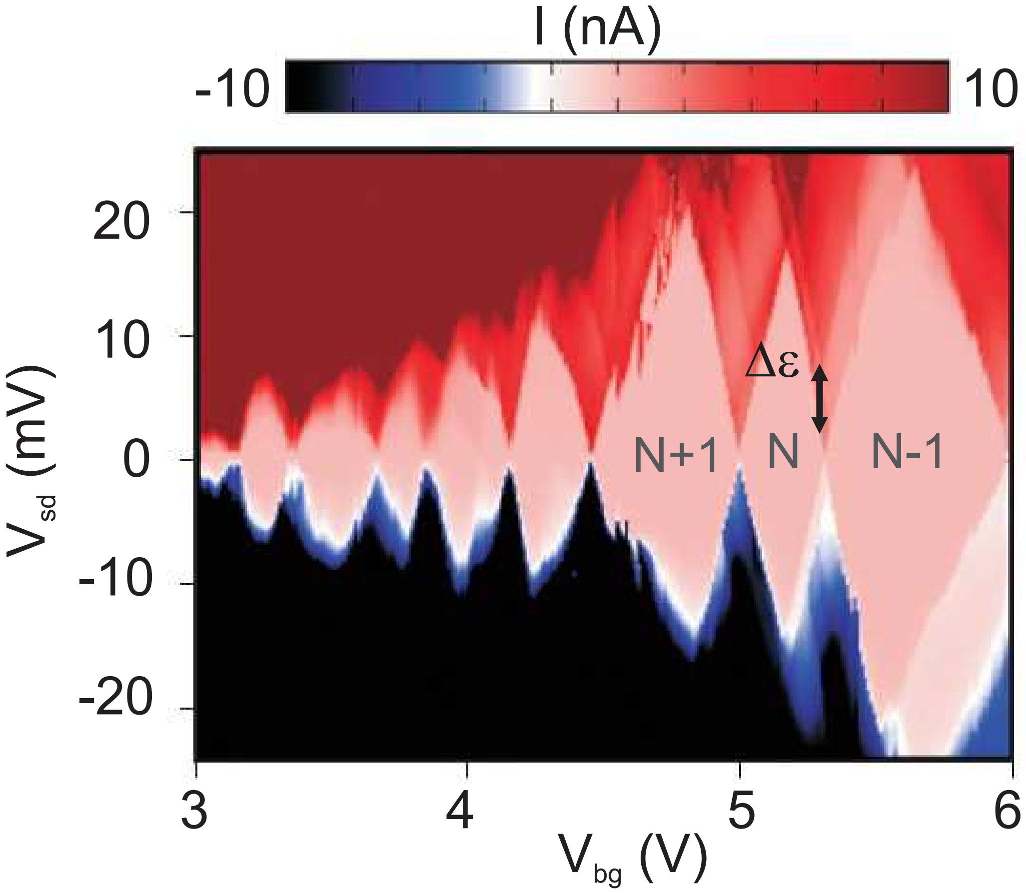

Figure 2.10: Stability diagram of a SiGe island coupled to Al leads taken from [13]. A 50 mT magnetic field perpendicular to the substrate plane was applied in order to suppress the superconductivity in the contacts. The current through the device is measured while sweeping V_{sd} and stepping the back-gate voltage, V_{bg}. A discrete energy spectrum is evidenced by steps in the current corresponding to the opening of transport channels involving excited states. The energy spacing $\Delta\varepsilon$ is indicated for one of these transitions. It is important to remark that, as the charge carriers are holes, the number of carriers N diminishes for more positive values of V_{bg}.

for $|T_+\rangle = |\uparrow\uparrow\rangle$, $S_z = 0$ for $|T_0\rangle = (|\uparrow\downarrow\rangle + |\downarrow\uparrow\rangle)/\sqrt{2}$ and $S_z = -1$ for $|T_-\rangle = |\downarrow\downarrow\rangle$.

The split energy levels, the ladder in electrochemical potentials for the allowed transitions and the corresponding lines in the stability diagram for a finite $\vec{B}$, are illustrated in Fig.2.11 a) [2]. Fig.2.11 b) exhibits a differential conductance measurement performed on a SiGe island contacted with Al leads in the presence of an external magnetic field perpendicular to the substrate plane B_z. The magnetic field causes a splitting of the diamond edges as indicated by green rhombi. This splitting follows from the lifting of the degeneracy in the ground states associated with the side diamonds. We thus conclude that the central diamond corresponds to an even number N of confined holes [2]. $g_\perp = (3.0 \pm 0.4)$ and $g_\perp = (2.8 \pm 0.4)$ are extracted for the right and the left diamond ground states, respectively [2]. The error bar on these measurements is given by the uncertainty in energy introduced by the life-time broadening of the confined energy states.

The line indicated by a star in Fig.2.11 b) is due to the spin-triplet excited state for N holes on the QD. We measure a 2 meV singlet-triplet energy in this particular device, which is an order of magnitude larger than for electrons in Si/SiGe heterostructures [36]. Noteworthy, large singlet-triplet excitation energies are particularly desirable for the observation of spin blockade in double-dot experiments [37]. Upon increasing B_z, the line denoted by a star splits as shown by the emergence of a second parallel line, indicated by a circle, that shifts away proportionally to B_z (see Figs.2.11 b) CENTER and RIGHT). This behaviour corresponds to the Zeeman splitting of the excited spin-triplet state [2] with $g_\perp = (2.8 \pm 0.4)$.

The Zeemann energy can also be extracted from cotunneling spectroscopy, as shown in Fig.2.12. Due to the fact that the smearing of the cotunneling step is uniquely determined by the electronic temperature [38], at very low temperatures the cotunneling spectroscopy provides a high resolution tool to estimate the Zeeman energy.

As mentioned before, the **g** tensor is affected by multiple electronic properties, and thus the measured g-factors differ substantially from the free-electron value (2.002). **g** also exhibits a pronounced anisotropy; in Fig.2.13 a) the Zeeman energy is measured in inelastic cotunneling as a function of B_z and $B_\parallel$ [13]. $g_\perp \approx 2.7$ and $g_\parallel \approx 1.2$ are the extracted g-factor values in the perpendicular and parallel plane, respectively. This anisotropy is qualitatively consistent with calculations for pure Ge islands [39]. Simi-

---

[2] Since we measure ΔE_z and we extract g from Eq.2.1, we have no information about the sign of g. Therefore, throughout this thesis, measured values of g will always stand for the absolute value of this magnitude. As will be discussed in Chapter 3, the sign of $g_\perp$ in SiGe dome islands appears to be negative.

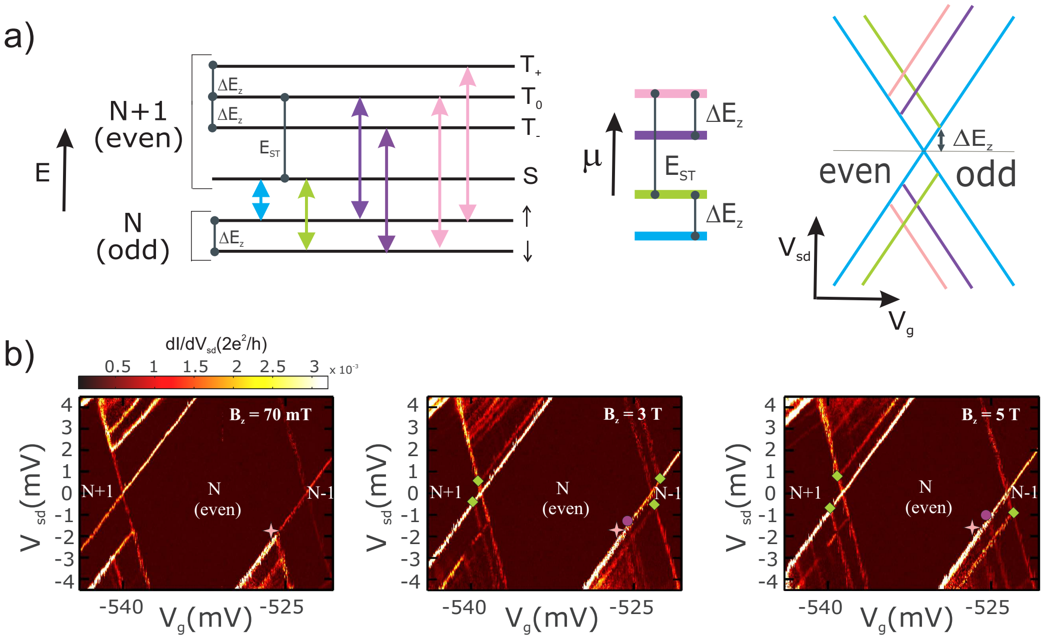

Figure 2.11: a) LEFT: Schematic energy diagram showing the split energy levels for an even and odd occupation of the island, being ΔE_z the Zeeman energy and E_{ST} the singlet-triplet energy difference at $B = 0$. The coloured vertical arrows represent excitations allowed by the spin selection rule ($|\Delta S_z| = 1/2$). We note that $\uparrow \leftrightarrow T_-$ and $\downarrow \leftrightarrow T_+$ are not allowed. CENTER: Electrochemical potential ladder for the transitions on the right using the same color coding. RIGHT: Schematics of a stability diagram plot where the lines corresponding to the allowed transition are illustrated. The color coding is also respected. b) dI/dV_{sd} as a function of V_{sd} and V_g for a SiGe device contacted by Al leads and measured at a base temperature of ~ 250 mK. LEFT: $B_z = 70$ mT, the line corresponding to the singlet-triplet transition is indicated. The purpose of this small magnetic field is to suppress the superconductivity of the Al contacts. CENTER, RIGHT: $B_z = 3$ T, $B_z = 5$ T respectively. The transitions in a) are indicated with symbols of corresponding colors. The lines indicated by green rhombi correspond to the onset of tunneling via Zeeman-split levels for $N-1$ and $N+1$ holes on the QD. The lines indicated by a star and a circle correspond to singlet-triplet excitations for N holes. Noteworthy, some of these transitions are visible for negative bias voltages, while they are not for positive values of the latter.

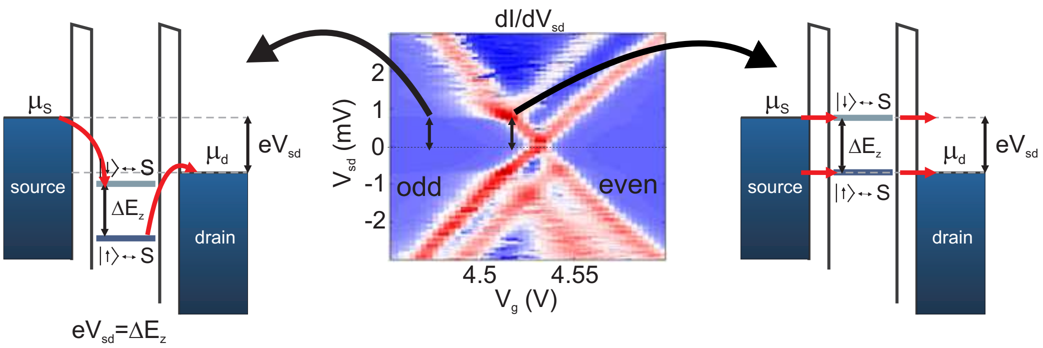

Figure 2.12: CENTER: dI/dV_{sd} as a function of V_{sd} and V_g is shown for a SiGe device in the presence of $B_z = 8$ T at 15 mK. Taken from [13]. RIGHT: Scheme of the direct tunneling process that gives rise to the line indicated in the center plot. LEFT: Inelastic cotunneling leading to the step in dI/dV_{sd} indicated in the center plot. This process activates when the bias voltage equals the difference in energy between the two electrochemical levels, i.e. when the bias coincides with the Zeeman energy. Inelastic cotunneling spectroscopy provides thus an additional way to measure the g-factor. From the observed step in dI/dV_{sd}, $g_\perp \approx 3$ was extracted.

lar anisotropies have also been reported for strained bulk Ge [40], acceptor levels in Si/Ge/Si heterostructures [41] and Ge/Si core-shell nanowires [42]. A characterization of the Zeeman energy as a function of the magnetic field angle is shown in Fig.2.13 b).

In [13] it has also been shown that **g** depends on the number of confined holes, i.e. on the diamond chosen for the Zeeman energy estimation (see Fig.2.13 c)).

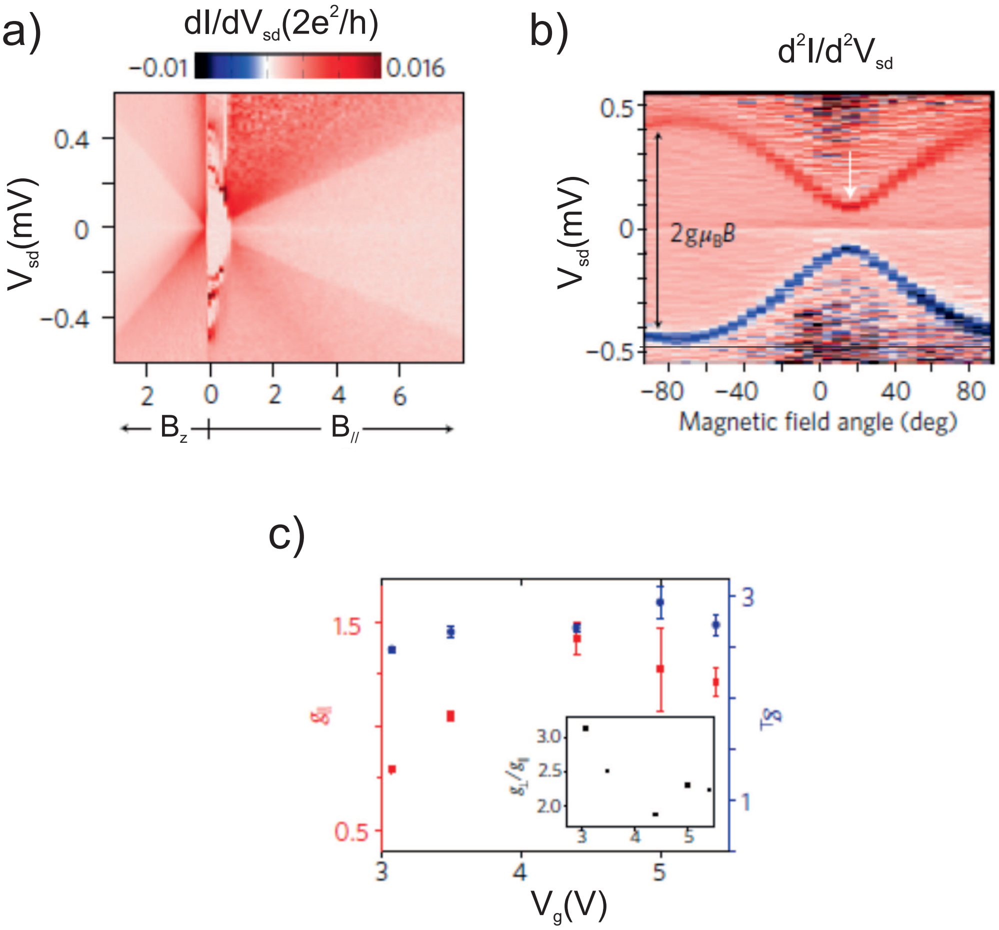

Figure 2.13: a) dI/dV_{sd} as a function of B_z and $B_\parallel$. To a good approximation, the Zeeman energy, given by the dI/dV_{sd} position of the inelastic-cotunneling steps, increases linearly with magnetic field, in agreement with Eq. 2.1. The features around $B = 0$ arise from the superconductivity of the aluminium contacts. b) Numerical derivative of dI/dV_{sd} as a function of the magnetic field angle with respect to the substrate plane. The minimum Zeeman energy, which does not correspond to a parallel B, is indicated by a white arrow. At this angle, $g_{min} \sim 0.5$ is estimated. c) Absolute values of $g_\perp$ and $g_\parallel$ measured for the same device at different number of confined charges. a), b) and c) were taken from [13].

Chapter 3

Electrically tunable g-factor

By means of *electron spin resonance* (ESR) techniques, coherent spin rotations can be induced. Usually, for an ESR to occur, the confined spin is exposed to an alternating magnetic field [43, 44, 45, 46]. However, because strong local oscillatory electric fields are easier to obtain than strong local oscillatory magnetic fields, interest has focused in spin resonance induced by electric fields. As mentioned in Chapter 1, spin-orbit coupling has been used to achieve an electric-dipole induced spin resonance (EDSR) in QDs [22, 23, 21]. For this technique, an external electric field is applied to the QD via a gate electrode to which an ac signal is supplied from an external circuit. An external static magnetic field induces the Zeeman splitting and secures the spin-electric coupling via the spin-orbit interaction [21]. As shown in [47], spin manipulation can also be achieved through fast control of the exchange coupling.

Another possibility for electric-field spin manipulation is the *g-tensor modulation* resonance, which has been used on ensembles of spins in two-dimensional electron systems [48, 49]. This technique relies on anisotropic and electrically tunable g-factors.

Recently, several experiments have addressed the g-factor modulation by means of external electric fields [50, 51], and different mechanisms were evoked to explain the observed g-factor tunability, such as compositional gradients [50] and quenching of the angular momentum [51, 52].

In this chapter, the experimental observation of an exceptionally large and non-monotonic electric-field modulation of the hole g-factor in SiGe QDs is discussed. To interpret this finding we invoke a new mechanism that applies to hole-type low-dimensional systems. This mechanism relies on the existence of an important, yet overlooked correction term in the g-factor whose magnitude depends on the mixing of heavy and light holes. The work presented in this chapter has lead to two publications [53, 54].

3.1 Device description

For this experiment, the complexity of the devices described in Chapter 2 was increased by placing a top gate electrode. A sketch of the device is shown in Fig.3.1 a).

In order to fabricate the top gate electrodes, the device was covered by a thin layer of hafnium oxide (HfO_2), also known as *hafnia*, which is an electrical insulator with a high dielectric constant. While silicon dioxide has a dielectric constant of 3.9, the dielectric constant of hafnia is around 25 [55].

This hafnia layer was deposited by *atomic layer deposition* (ALD), a technique that uses two chemicals, typically called precursors, that react with a surface one at a time in a sequential, self-limiting way. By repeatedly exposing the precursors to the growth surface, a conformal thin film is deposited. In our case, 60 cycles, which correspond to a 6 nm-thick layer, were performed. A Cr/Au gate electrode for each device was then defined, by ebeam lithography, on top of the hafnia layer (see Fig.3.1 b)). In Fig.3.1 c), a SEM image of the resulting device is shown.

We noticed that the writing of the top gate electrode on the hafnia layer induces charges that shift the threshold voltage of the devices. This shift can be compensated by properly tunning the back gate electrode.

3.2 Experiment

The top gate electrode, together with the degenerately-doped Si back-gate, allows a perpendicular electric field (F) to be applied while maintaining a constant number of holes in the SiGe QD. This concept is depicted in Fig.3.2.

These dual-gate devices allow us to measure the dependence of the g-factor on the perpendicular electric field for a constant number of confined charges. The principle of such a measurement is illustrated in Fig.3.3 a). The Zeeman splitting is given by the distance between the blue and the red circles along V_{bg}, multiplied by a calibration factor α. The latter is the *lever arm*, obtained by dividing V_{sd} by the distance between the green and the red circles. In order to investigate the F-dependence of the g-factor, we apply perpendicular magnetic field, $B_z = 4$ T, we set $V_{sd} = 2.6$ mV and sweep V_{bg} for different values of V_{tg}. The data is shown in Fig.3.3 b) and the extracted g-factors are displayed in Fig.3.3 c). All measurements shown in this chapter were done in a ^{3}He refrigerator with a base temperature of 250 mK.

We observe an exceptionally large g-factor modulation ($\delta g/g \sim 1$) denoting a strong effect of the applied F. The g-factor increases slowly to a maximum value of 2.6 and then drops rapidly till the Zeeman splitting can

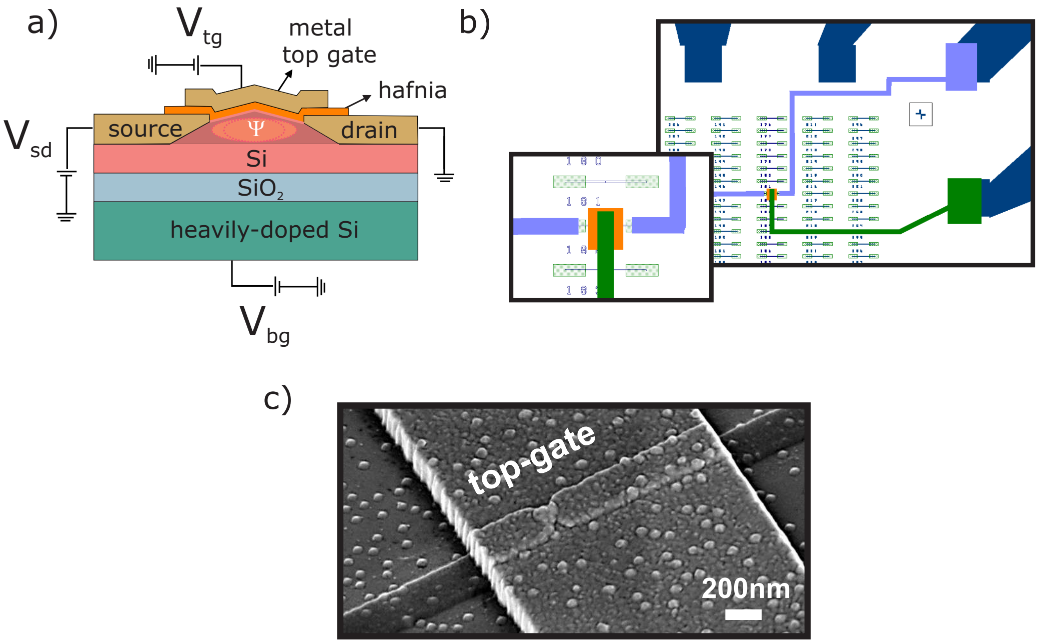

Figure 3.1: a) Schematic cross section of the device. b) Design of a write-field inner area with a contacted SiGe island for which a top gate electrode is defined. The orange square delimits the area covered with hafnia. Ebeam lithography, development, ALD deposition and lift-off in hot acetone for about 10 min is performed in order to define this area. The green line represents the Cr/Au top gate electrode that is afterwards defined by another lithographic step. In the inset, a zoom-in on the design. c) SEM image of a device.

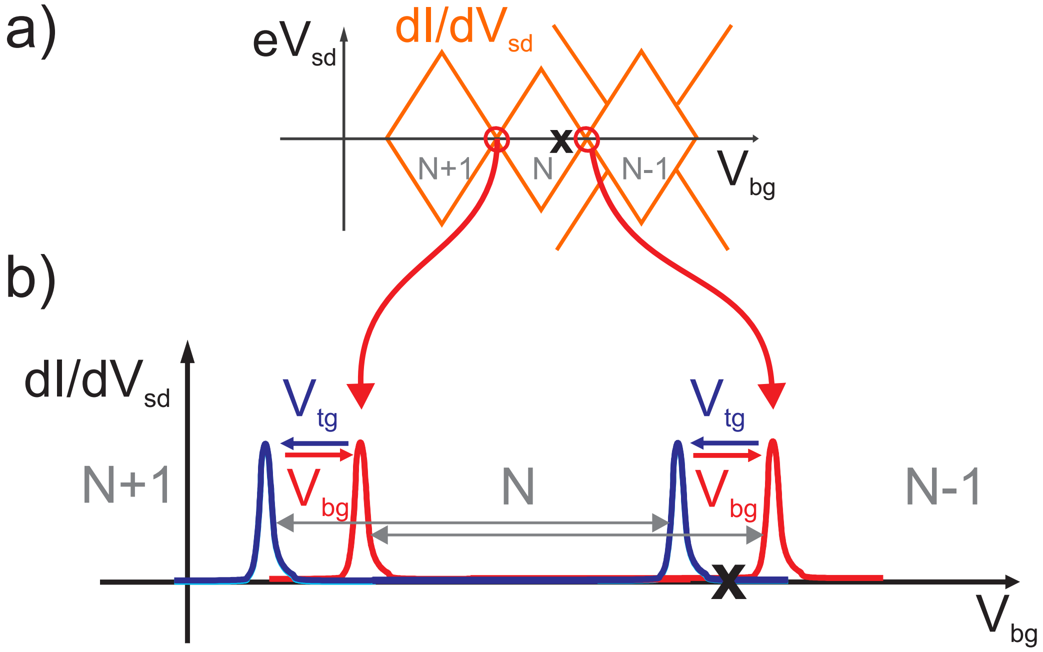

Figure 3.2: a) Scheme of the stability diagram of a device confining holes, being V_{bg} the voltage applied to the back-gate. Red circles highlight the degenerate points. A V_{bg} value for $V_{sd} = 0$ is indicated with a black cross, where the amount of charges in the QD is fixed and equal to N. b) Red curves depict the resonances in conductance in a) at $V_{sd} = 0$. By applying a voltage to the top-gate electrode, V_{tg}, these resonances can be shifted away from depletion (blue curves). In this case, the V_{bg} value indicated by a cross does not correspond any longer to N confined carriers, but to $N-1$. However, a V_{bg} can be applied to bring the resonances back to its initial position. In this way, the position of the cross in V_{bg} corresponds again to N confined charges and the difference between V_{bg} and V_{tg} gets bigger. The external electric field, proportional to this difference, can thus be enlarged while the number of charges inside the island is kept unchanged.

no longer be resolved.

It is known that thermal cycling can change the characteristics of a device and thus different set of data can be obtained for the same device [26]. A drastic change in V_{tg} (of about 3 V) appeared to produce a similar effect in our system. In this way, we could perform the g-factor measurements on two devices with completely different characteristics. This time, a slightly different type of measurement, based on the mechanism described in Fig.3.2 b), was performed in order to extract the g-factors.

The same conductance peak can be very easily followed since for each mV applied to V_{tg}, the resonances move $\sim$ 13.2 mV in V_{bg}. This ratio reflects the difference in coupling between the QD and the two gates. Fig.3.4 a) shows how two resonant peaks shift by sweeping V_{bg} for different values of V_{tg};$V_{tg} \simeq -583$ mV (blue trace) and $V_{tg} \simeq -620$ mV (red trace). The reason why the resonant peaks appear to be split is that dI/dV_{sd} was measured under $V_{sd} = 1$ mV.

By following a particular peak in conductance we could, for different values of V_{tg}, sweep V_{sd} as a function of V_{bg}, and obtain a stability diagram for the same number of confined holes under different applied electric fields. From the Zeeman split lines observed in the stability diagrams, the g-factors for 11 different values of V_{tg} and V_{bg} were obtained, see Fig.3.4 b). The inset which is surrounded by a blue rectangle shows the dI/dV_{sd} as a function of (B_z,V_{sd}) for $V_{tg} \simeq -583.2$ mV. This plot demonstrates that the parallel to the ground state line seen in the stability diagrams insets (orange rectangles), is indeed the Zeeman splitting. The features at small fields are due to the superconducting nature of the Al contacts [13].

From Fig.3.4 b) it becomes clear that the external electric field has a very strong effect on the g-factor value. It reaches a minimum value of (2.3 ± 0.2) and a maximum value of (3.7 ± 0.4). This is, to our knowledge, the biggest g factor value measured in SiGe nanostructures. Even larger g-factors can be obtained for QDs with higher Ge content, as has been shown by theoretical calculations [39].

3.3 Analysis

In order to uncover the origin of this unusual behavior, our starting point is the Luttinger Hamiltonian [56]. This Hamiltonian was devised to construct an effective mass description of the valence band structure taking into account its threefold degeneracy ($l = 1$). This may be done using symmetry considerations: a scalar Hamiltonian should be constructed, which must be quadratic in k, the linear momentum. If we require invariance under rota-

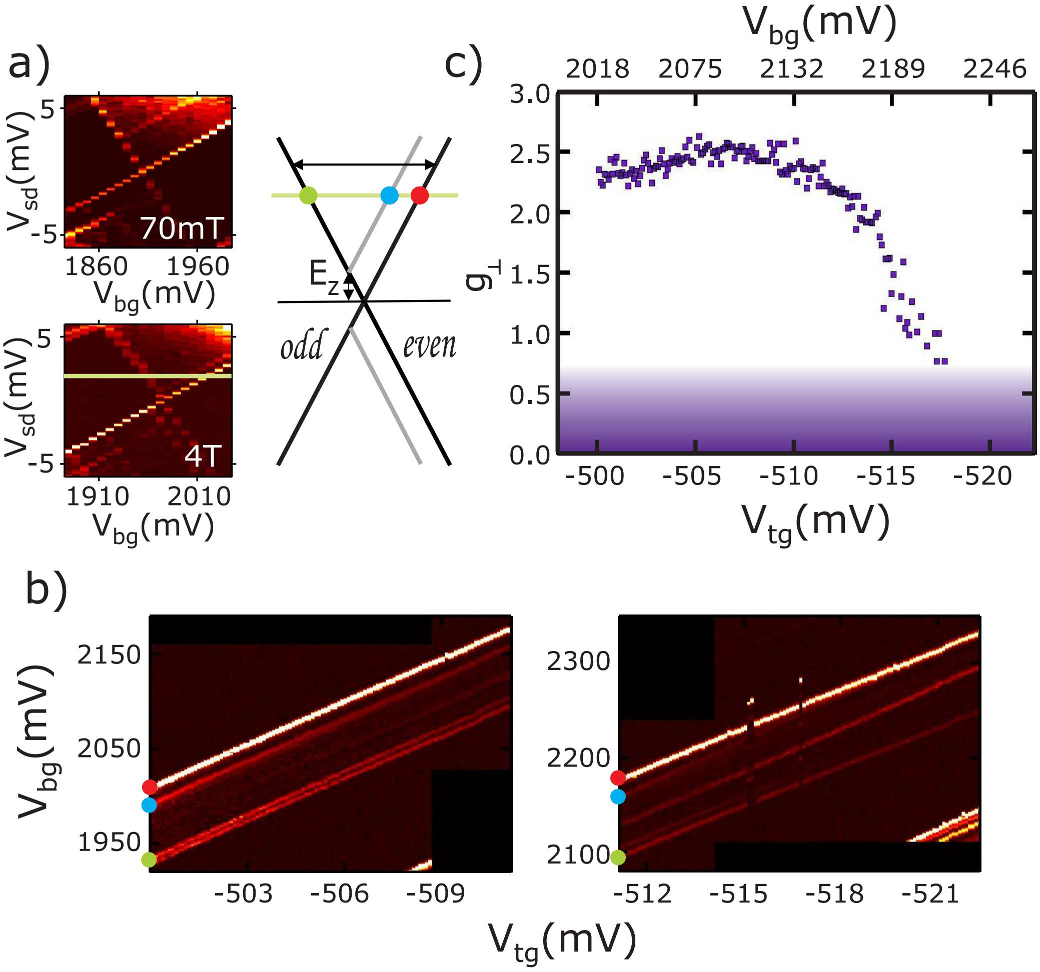

Figure 3.3: a) Left: Color plots of $dI/dV_{sd}(V_{bg}, V_{sd})$ for $B_z = 70$ mT and 4 T. At 4 T the Zeeman splitting is clearly visible. Right: Corresponding schematic diagram illustrating the measurement principle to extract the Zeeman energy splitting (and hence the g-factor) from gate-voltage sweeps at constant V_{sd} (see the horizontal green line). b) Color plots of $dI/dV_{sd}(V_{bg}, V_{tg})$ for a fixed $V_{sd} = 2.6$ mV. These data sets demonstrate the modulation of $g_\perp$ by the top and back gates. c) $g_\perp(V_{bg}, V_{tg})$ as extracted from b). Below $g_\perp \approx 0.75$ the Zeeman splitting cannot be resolved any more due to the finite broadening of the tunneling resonances.

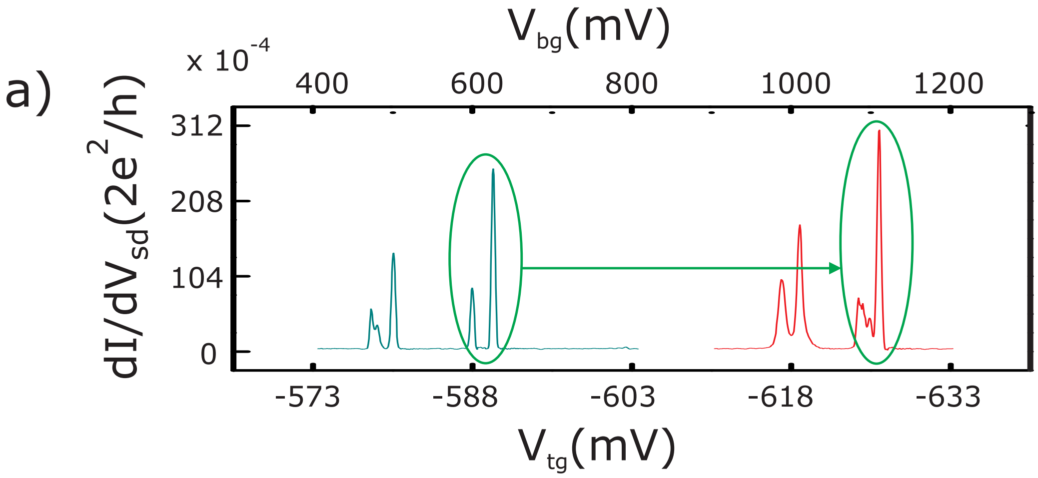

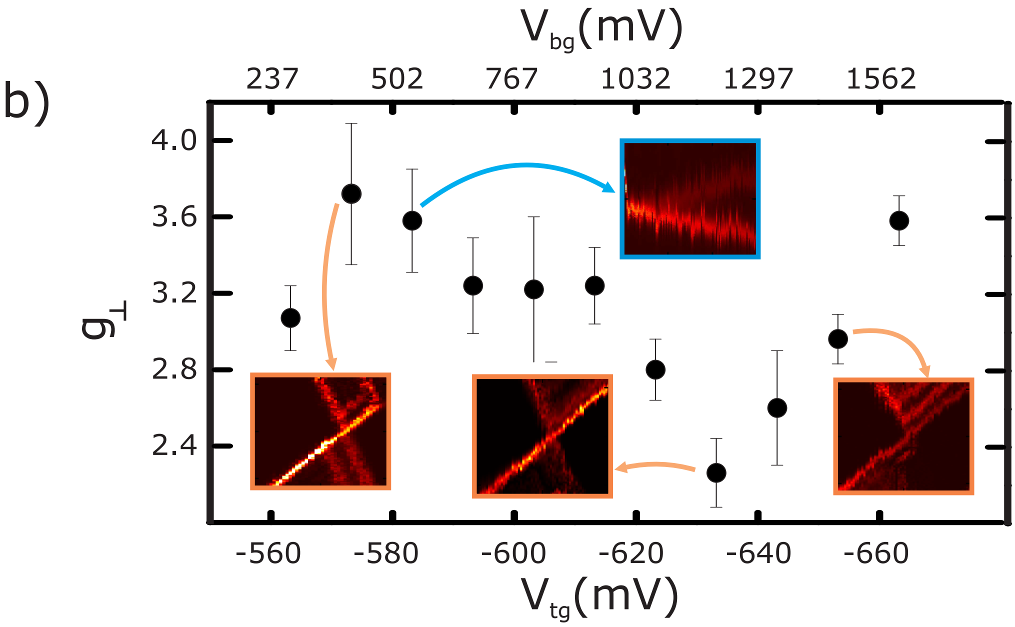

Figure 3.4: a) Plot of dI/dV_{sd} versus V_{bg} (swept) and V_{tg} (estimated from V_{bg}) for $V_{sd} = 1$ mV showing how two resonant peaks move while changing the value of the external electric field, i.e. while applying different values of V_{tg} ($\simeq -583$ mV for the blue trace and $\simeq -620$ mV for the red trace). b) Plot of the g-factor versus V_{bg} and V_{tg} showing a non monotonic behaviour of the g-factor value for different perpendicularly applied electric fields. The insets show stability diagrams at $B_z = 1.5$ T. V_{bg} is swept by 50 mV while V_{sd} by 2.4 mV. The blue inset demonstrates that indeed the parallel to the ground state line is the Zeeman splitting since it merges with the ground state for vanishing magnetic fields.

tions, the only possibility is the Luttinger Hamiltonian. This Hamiltonian is a 3×3 matrix, and the energy spectrum in the valence band is found by diagonalizing this matrix [57].

Due to the spin-orbit interaction, the six-fold degeneracy at the Gamma-point of the valence band is lifted. This leads to a four-fold degenerate valence-band edge, formed by heavy-hole and light-hole states with angular momentum $J = 3/2$, and a two-fold degenerate split-off band with angular momentum $J = 1/2$. The split-off band lays below the valence-band edge by an energy Δ_{SO}, which is known as the spin-orbit splitting (see Chapter 1). For semiconductors with large Δ_{SO}, the split-off band is far away in energy and thus, we can focus on the light and heavy hole bands.

We have thus modelled the QD electronic states in terms of HH and LH subbands. Given the relatively large anisotropy of dome-shaped QDs, we initially considered the two-dimensional (2D) limit resulting from confinement along the growth axis (see appendix I). The top-most subband has HH character and its in-plane dispersion relation is then described by the effective 2D Hamiltonian

$$\begin{aligned} H_{\text{eff}} &= \frac{1}{2m_{\parallel}}\left(k_x^2 + k_y^2\right) + \frac{1}{2} g_{\parallel} \mu_B \left(\sigma_x B_x + \sigma_y B_y\right) \\ &\quad - \frac{1}{2} g_{\perp} \mu_B \sigma_z B_z + U(x,y), \end{aligned} \tag{3.1}$$

where k_x and k_y are the in-plane momentum operators, $m_{\parallel} = m/(\gamma_1 + \gamma_2)$ is the in-plane effective mass [58], $g_{\parallel} = 3q$ and $g_{\perp} = 6\kappa + \frac{27}{2}q$ are, respectively, the in-plane and transverse g-factors [58, 59], $\boldsymbol{\sigma}$ are the Pauli matrices in the pseudospin space [1], and $U(x,y)$ is the in-plane confining potential in the QD. We use standard notations for the Luttinger parameters γ_1, γ_2, γ_3, κ, and q [56]. Since $q \ll \kappa$, it is appropriate to assume $g_{\perp} \approx 6\kappa$. As we have mentioned in Chapter 2, $g_{\perp}$ appears to be negative for SiGe dome islands, considering their Ge content (Fig.1.4 b)) and the values of the Luttinger parameters correspondent to these alloys [60]. Noteworthy, the minus sign in front of $\frac{1}{2}g_{\perp}$ in Eq. (3.1) is introduced for the convenience of having $g_{\perp}$ positive for Ge.

First we consider the possibility that the observed g-factor modulation arises from a compositional gradient. This mechanism was exploited in $\mathrm{Al_xGa_{1-x}As}$ quantum wells to implement electrical control of electron spins [49, 48]. In Stranski-Krastanow QDs, Si and Ge form a $\mathrm{Si_{1-x}Ge_x}$ alloy in

---

[1] We choose the pseudospin basis described in appendix I; namely, $|\Uparrow\rangle_h = |3/2, -3/2\rangle$ and $|\Downarrow\rangle_h = |3/2, +3/2\rangle$.

which x increases monotonically with z, being zero at the base ($z = -w$) and approaching unity at the apex ($z = 0$) of the QD [19]. Since $\kappa_{\mathrm{Si}} = -0.42$ and $\kappa_{\mathrm{Ge}} = 3.41$, one would expect that $g_\perp$ increases with F following a vertical shift of the HH wave function towards the apex.

To find an upper bound for the g-factor variation resulting from the compositional gradient, we take the steepest dependence reported for the Ge content across the QD [19],

$$\mathsf{x}(z) = \mathsf{x}_{\max}\sqrt{1 + \frac{z}{w}}. \qquad -w < z < 0. \tag{3.2}$$

To account for the existing uniaxial strain, we assume that the in-plane lattice constant $a_\parallel$ increases linearly from 5.47 Å at the base to 5.59 Å at the apex [19]. The resulting valence-band profiles $E_v(z)$ for all types of holes are calculated using interpolation schemes devised for SiGe [18, 61] (see inset of Fig.3.5). The HH ground state is thus confined to a triangular potential well arising from the compositional gradient. An electric field applied along z adds a term $-eFz$ to $E_v(z)$. For a given F, the HH wave function $\psi(z)$ is obtained by solving the Schrödinger equation numerically. The HH g-factor is found as a weighted average

$$g_\perp \approx 6\,\langle\kappa\rangle = 6\int \kappa\left[\mathsf{x}(z)\right]\left|\psi(z)\right|^2 dz, \tag{3.3}$$

where $\kappa\,(\mathsf{x})$ is obtained as described in [60]. The resulting $g_\perp(F)$ dependence is shown in Fig. 3.5. We distinguish two regimes: that of a strongly asymmetric (triangular) potential well and that of a symmetric potential well. The modulation of the g-factor is largest in the latter regime (see dotted line), where $dg_\perp/dF \approx 0.41\,\mathrm{m/MV}$. While the magnitude of the modulation is close to what is observed in the experiment, the sign of $dg_\perp/dF$ is opposite. We conclude that the compositional-gradient cannot explain our data. Therefore, from now on, we shall discard this mechanism and assume the Ge content to be constant within the QD.

We revisit the derivation of Eq. (3.1), starting from the 4×4 Luttinger Hamiltonian, which, in the 2D limit, separates into 2×2 HH and LH blocks (see appendix I). To leading order in $w/d \ll 1$, the HH and LH sectors are connected by the off-diagonal mixing blocks

$$H_{hl} = \left(H_{lh}\right)^\dagger = i\frac{\sqrt{3}\gamma_3}{m}\left(k_x\sigma_y + k_y\sigma_x\right)k_z, \tag{3.4}$$

where k_x and k_y are 2D versions of momentum operators (insensitive to in-plane magnetic fields), $k_z \equiv -i\hbar\partial/\partial z$, and σ_x and σ_y are the Pauli matrices in a pseudospin space.

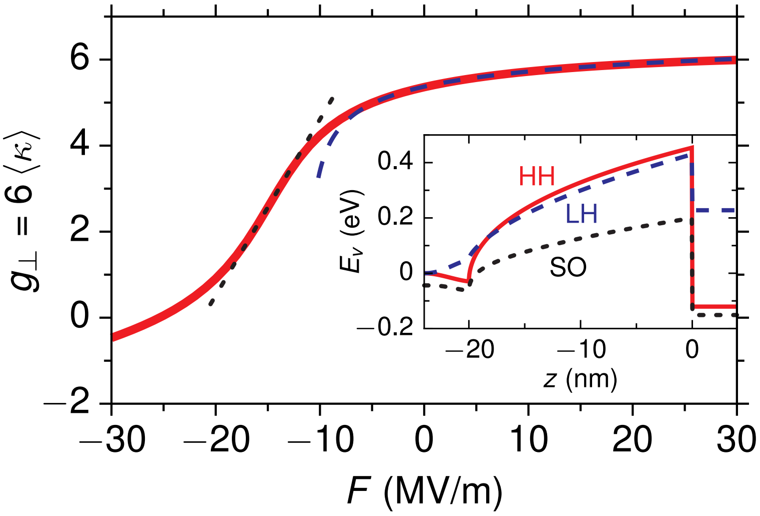

Figure 3.5: Expected $g_\perp(F)$ dependence for a SiGe QD with strong compositional gradient. The numerical result (solid line) has two regimes: the dashed line shows a fit to the expression $\langle\kappa\rangle = \kappa_\infty - \Delta\kappa\,(1 + F/F_{\rm intr})^{-1/3}$, derived for a triangular potential well with an intrinsic field $F_{\rm intr}$ for $z < 0$ and an infinite barrier for $z > 0$; the dotted line is a fit to a linear dependence, obtained for a symmetric potential well. In the latter regime, $g_\perp$ is most sensitive to F, with $dg_\perp/dF = 0.41\,$m/MV. At large negative F, the wave function is pushed into the Si-rich region, where $g_\perp < 0$. Inset: Energy profiles for the heavy-hole (HH), light-hole (LH), and split-off (SO) bands as calculated from Eq. (3.2) with $\mathsf{x}_{\rm max} = 0.8$. We set $\mathsf{x} = 0$ for $z < -20$ nm to account for the Si substrate, and $\mathsf{x} = 0$ for $z > 0$ to account for the existence of a strained, few-nm-thick Si capping layer.

The mixing blocks in Eq. (3.4) are proportional to k_z. In spite of the fact that k_z averages to zero for each type of hole separately, it cannot be discarded in Eq. (3.4), because matrix elements of the type $\langle\psi_h|\, k_z\, |\psi_l\rangle$ are, in general, non-zero and scale as $1/w$ for $w \to 0$. Here, $\psi_h(z)$ and $\psi_l(z)$ obey two separate Schrödinger equations, for heavy and light holes, respectively (see below). This observation allows us to anticipate that in second-order perturbation theory the mixing blocks lead to an energy correction containing $H_{hl}H_{lh} \propto k_z^2$ in the numerator and $H_{ll} - H_{hh} \propto k_z^2$ in the denominator. This correction does not vanish in the 2D limit ($k_z \to \infty$). At the same time, the correction to the wave function vanishes as $k_\parallel/k_z \sim w/d$.

Using second-order perturbation theory, we recover Eq. (3.1) for the topmost hole subband. Yet, at the leading (zeroth) order in $w/d \ll 1$, we obtain the following modified expressions for the effective mass and the perpendicular g-factor,

$$m_\parallel = \frac{m}{\gamma_1 + \gamma_2 - \gamma_h}, \quad g_\perp = 6\kappa + \frac{27}{2}q - 2\gamma_h. \tag{3.5}$$

The in-plane g-factor remains unchanged ($g_\parallel = 3q$) at this order. In Eq. (3.5), γ_h is a dimensionless parameter sensitive to the form of the confinement along z,

$$\gamma_h = \frac{6\gamma_3^2}{m}\sum_n \frac{\left|\langle\psi_n^l|\, k_z\, |\psi_1^h\rangle\right|^2}{E_n^l - E_1^h}. \tag{3.6}$$

Here, the sum runs over the LH subbands and the wave functions $\psi_n^{h/l}(z)$ and energies $E_n^{h/l}$ obey

$$\left[\frac{k_z^2}{2m_\perp^{h/l}} + V_{h/l}(z)\right]\psi_n^{h/l}(z) = E_n^{h/l}\psi_n^{h/l}(z), \tag{3.7}$$

where $m_\perp^{h/l} = m/(\gamma_1 \mp 2\gamma_2)$ and $V_{h/l}(z)$ is the confining potential seen by the heavy/light hole. The electric field contributes to $V_{h/l}(z)$ with the term $-Fz$ [2].

When $V_h(z)$ and $V_l(z)$ are infinite square wells, an analytical derivation yields

---

[2] In piezoelectric materials (not in SiGe), the application of an electric field may change the strain distribution inside the nanocrystal, giving rise to additional terms in $V_h(z)$ and $V_l(z)$ proportional to the electric field.

$$\gamma_h = \frac{12\gamma_3^2}{\gamma_1 + 2\gamma_2}\left[\frac{1}{1-\beta} - \frac{4\sqrt{\beta}}{\pi\,(1-\beta)^2}\cot\left(\frac{\pi}{2}\sqrt{\beta}\right)\right], \tag{3.8}$$

where $\beta = m_\perp^l/m_\perp^h + \delta E_{001}/E_1^l$, with $\delta E_{001} \equiv V_h - V_l$ being the splitting of the valence band due to uniaxial strain and $E_1^l = \pi^2\hbar^2/2m_\perp^l w^2$. Notably, one has $\psi_n^h(z) = \psi_n^l(z)$ in this case, because the masses $m_\perp^h$ and $m_\perp^l$ drop out of the expressions for the wave functions. An electric field causes $\psi_n^h(z)$ and $\psi_n^l(z)$ to shift relative to each other, because of the different effective masses, $m_\perp^h \neq m_\perp^l$. Although γ_h can only be numerically computed, its qualitative F-dependence can be inferred from Eq. (3.6). The $n = 1$ term dominates the sum due to its smallest energy denominator. For a square-well potential, however, this term vanishes by symmetry. As a result, the symmetric point $F = 0$ corresponds to a minimum in $\gamma_h(F)$, since $E_n^l > E_1^h$. Away from $F = 0$, γ_h increases quadratically, $\gamma_h \propto F^2$, up to the point where the electric field is strong enough to shift the HH wave function ($eFw \simeq E_2^h - E_1^h$). Then, γ_h increases roughly linearly up to the point where the LH wave functions begin to shift ($eFw \simeq E_2^l - E_1^l$). Upon further increasing F, γ_h increases weakly and saturates to a constant. We remark that $g_\perp$ is modified by γ_h even at $k_\parallel = 0$, despite the absence of HH-LH mixing at $k_\parallel = 0$. In fact, since $g_\perp$ is sensitive to in-plane orbital motion [62], even a small B_z translates to $k_\parallel \neq 0$, leading to HH-LH mixing.

Our result in Eq. (3.5) represents the zeroth-order term in the expansion $g = g^{(0)} + g^{(2)} + \ldots$, where $g^{(2)} \propto (w/d)^2$ is the subleading-order term. Unlike the main term, the correction $g^{(2)}$ is sensitive to the in-plane confining potential $U(x, y)$ and it originates from the HH-LH interference terms in the wave function. In Fig. 3.6, we fit the experimental data using only the leading, zeroth-order term. The HH and LH wave functions, $\psi_1^h(z)$ and $\psi_1^l(z)$, shift upon application of the electric field. The transition from square well (central inset) to triangular well (highest insets) occurs in two steps. First, $\psi_1^h(z)$ shifts by $\delta z \sim w$, while $\psi_1^l(z)$ remains nearly unaffected (lowest insets). Then, $\psi_1^l(z)$ shifts as well (highest insets). At even larger F (not shown) $g_\perp$ saturates to $g_\perp \approx 0.6$. The calculated $g_\perp(F)$ dependence, taking into account γ_h, qualitatively reproduces the experimental data. We have also verified that the inclusion of an electric-field gradient into our model (as result of screening by source and drain electrodes) improves the agreement between theory and experiment, see dashed line in Fig. 3.6. To a first approximation, we had dispensed with the screening effect of the source and drain electrodes and assumed the electric field to be homogeneous in space.

Finally, we remark that the correct 2D limit of the Luttinger Hamiltonian has been largely overlooked. Although our main result in Eq. (3.5) bears

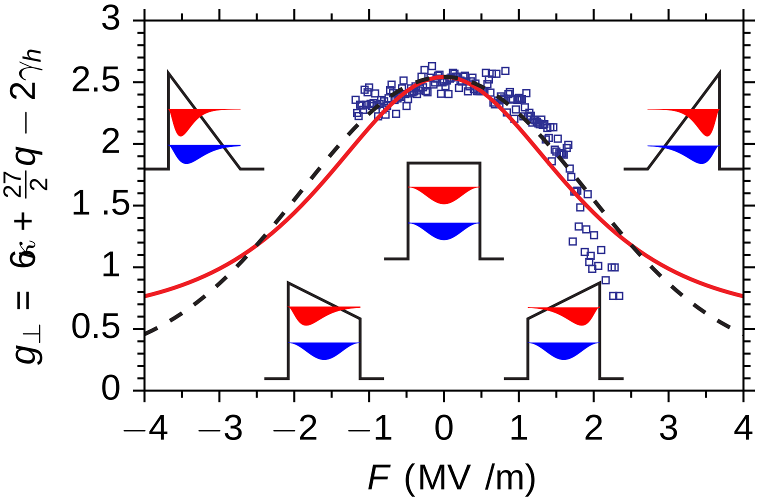

Figure 3.6: The $g_\perp(F)$ dependence according to Eq. (3.5) (solid line) superimposed on the experimental data (squares) of Fig. 3.3(c). Since the variations in V_{bg} and V_{tg} are proportional to each other, we take $F = aV_{tg} + b$, with fitting parameters a and b. The dashed line is an improved fit obtained with a model that allows for a field gradient across the SiGe nanocrystal (such a gradient is expected as a screening effect of the source and drain electrodes). For $z \in [-w, 0]$, we assume an electrostatic potential of the form $V(z) = -cF(z + w/2)^2 - Fz$, where c is a fit parameter. Insets: Schematics of the HH (red) and LH (blue) wave functions at different F. At finite, intermediate fields (lowest insets) the two wave functions are shifted relative to each other resulting in the largest $|dg_\perp/dF|$.

some relation to earlier works [3], the relation of $m_\parallel$ and $g_\perp$ to an additional parameter γ_h and the fact that γ_h is sensitive to F have been missing from the general knowledge of 2D hole systems.

In conclusion, we showed that an external electric field can strongly modulate the perpendicular hole g-factor in SiGe QDs. By a detailed analysis, we ruled out the compositional-gradient mechanism as the origin of this electric-field effect. By analysing the Luttinger Hamiltonian in the 2D limit, we found a new correction term γ_h which had not been considered before in the literature. This new term, which corrects the "standard" expression for the HH g-factor, reflects the effect of a perpendicular magnetic-field on the orbital motion, and it is ultimately related to the atomistic spin-orbit coupling of the valence band.

Moreover, according to the given theoretical description of the g-factor variation, we should be able to observe a strong effect just when the applied electric field drives the system from the triangular to the flat band configuration. This is the case shown in Fig.3.3 c). In Fig.3.7 the g-factor variation is shown for the same device but in an electric field regime in which the potential well configuration is always triangular. Although the range of V_{tg} and V_{bg} is similar in both Fig.3.3 c) and Fig.3.7, there is no obvious change in the g-factor value for the latter case, as expected.

Finally, from the second set of data shown in Fig.3.4, two different behaviours are distinguished. From $V_{tg} \approx -560$ mV to $V_{tg} \approx -630$ mV, the modulation in the g-factor resembles the one shown in Fig.3.3 c). It can be explained by the dependence of γ_h on F. However, from $V_{tg} \approx -630$ mV to $V_{tg} \approx -660$ mV an abrupt increase of the g-factor for increasing electric field can be observed. This behaviour is not compatible with the devised theoretical model. A careful inspection of the stability diagram of Fig. 3.4 b) for $V_{tg} \approx -650$ mV shows that additional levels are present close the studied level. No closely-lying levels are present in the range $V_{\text{tg}} \in [-560, -630]$. We believe that the data in the range $V_{tg} \in [-630, -660]$ refers to a different size-quantization level than the data in the range $V_{tg} \in [-560, -630]$. Indeed, the ground-state level might have changed in going from one range to the other, which is presumably signified by the pronounced cusp in the g-factor data at $V_{tg} \approx -630$ mV in Fig. 3.4 b). Such transitions are expected to occur when the Fermi level is placed sufficiently deep in the valence band. Then, ladders of levels belonging to different heavy-hole subbands move with respect to each other when the electric field is varied. Since these levels have very

---

[3] D'yakonov and Khaetskii [63] studied the Luttinger Hamiltonian in an infinite square well and used the spherical approximation ($\gamma_2 = \gamma_3$). They derived an expression for $m_\parallel$ that agrees with our result in the appropriate limit. We also verified that Eqs. (3.5) and (3.6) can be obtained from a general $\boldsymbol{k} \cdot \boldsymbol{p}$-approach [64, 65] after a lengthy calculation.

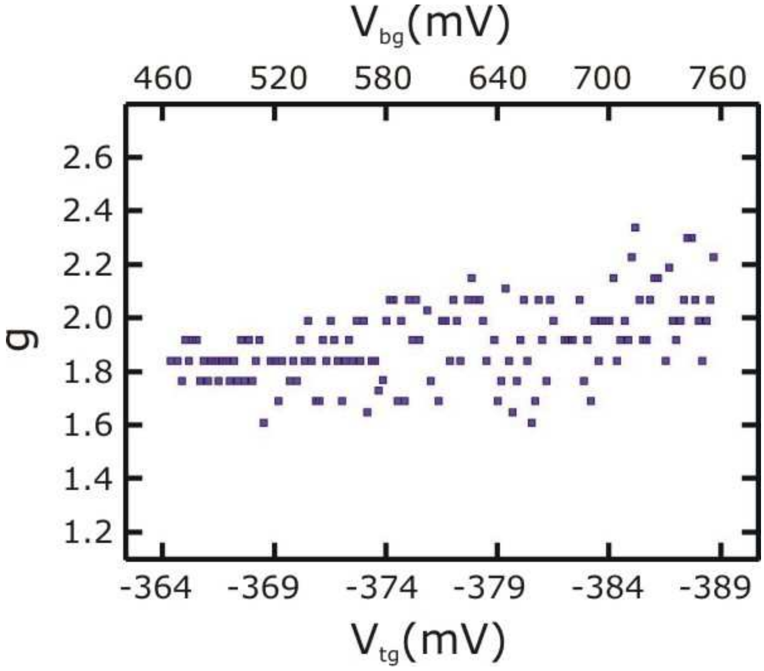

Figure 3.7: Measured g-factor vs V_{tg} and V_{bg} for the triangular potential well configuration. There is no clear variation in the g-factor value.

different z-components of the wave function, they interact weakly and can come close to each other without a sizeable level repulsion. Levels belonging to one ladder cannot come close to each other when the electric field is varied. We therefore speculate that the data in the range $V_{tg} \in [-630, -660]$ refers to a level from the second heavy-hole subband.

The following question arises: How can the two heavy-hole subbands have different characteristic values of the electric field at which the g-factor reaches maximum?. It is important to note that our theoretical model is strongly simplified. The real confining potentials $V_h(z)$ and $V_l(z)$ in the nanocrystals are, most likely, never perfectly symmetric and differ from each other. Therefore, it is natural to expect that the alignment along z of wave functions of the two heavy-hole subbands with respect to each other and, at the same time, with respect to the light-hole subbands is not perfect. The data in Fig.3.4 b) is consistent with the assumption that the wave function of the second heavy-hole subband is shifted towards the base of the nanocrystal and it begins to align with the light-hole wave functions at a later value of the electric field.

It is important to remark that higher-order corrections to the expansion of the g-factor of the top-most subband cannot explain the abrupt increase taking place for $V_{tg} \in [-630, -660]$, because their contribution is small by $\sim (w/d)^2$, which amounts to only a 10%-correction to the main term for our devices.

3.4 Electrically tunable g-factor as a control mechanism

In the g-tensor modulation technique, spin rotations result from an electrically induced oscillation of the Zeeman vector. An ac signal can then be applied to the top gate electrode in order to generate this effect. Devices with no back gate electrode were tested in order to verify if just a top gate electrode would be sufficient for the devised experiment. For that purpose, the fabrication procedure described in section 3.1 needed to be revised, as in the absence of a second gate electrode, the shift in the threshold voltage (induced by the charging of the hafnia layer during ebeam) cannot be compensated.

Thus, to avoid the ebeam writing on hafnia, first the top gate electrode area for a given device was defined, then a thin layer of hafnia was deposited and finally, the Cr/Au was evaporated. The subsequent lift-off step was extremely hard, but we have found out that it could be greatly improved by

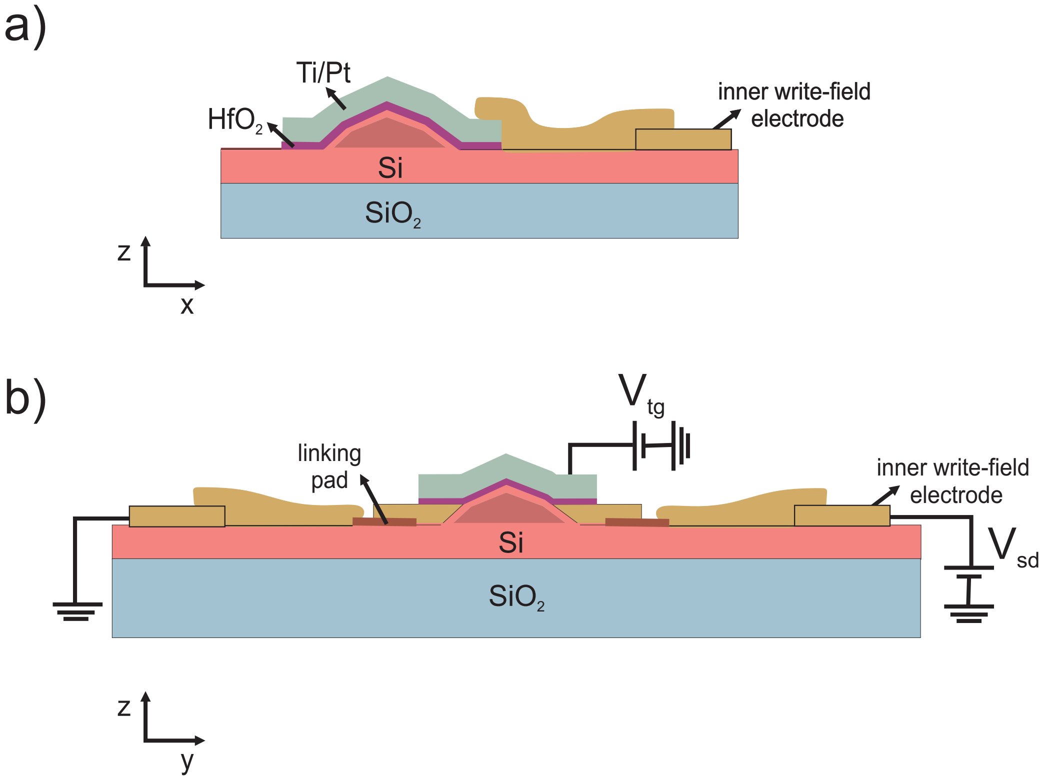

Figure 3.8: a) Scheme of the device in the (x,z) plane showing the top gate electrode formed by deposition of hafnia followed by evaporation of a Ti/Pt layer. b) Scheme of the same device in the (y,z) plane.

depositing Ti/Pt 10/90nm instead of Cr/Au in the same proportion. Another lithographic step was then needed in order to contact the top gate electrode with the inner write-field electrodes (see Fig.3.8 a) and b)).

The differential conductance of one of such devices was studied for an odd diamond in order to gain insight into the Zeeman-split states. Figs. 3.8 a) and 3.8 b) show a stability diagram of this diamond for $B = 0.6$ T applied perpendicular and parallel to the growth plane, respectively. Steps due to the presence of inelastic cotunneling processes are observed.

By fixing V_{tg} within the Coulomb blockade regime and sweeping the magnetic field, the behavior of the cotunneling steps was investigated. These measurements are shown in Figs.3.8 c) and d). As the cotunneling steps merge together when B approaches zero, we can confirm that the observed steps correspond to the Zeeman splitting of the ground state (ΔE_Z). The g-factor value perpendicular ($g_\perp$) and parallel ($g_\parallel$) to the substrate plane can be extracted from these measurements. The extracted values are $g_\perp = (2.0 \pm 0.2)$ and $g_\parallel = (1.2 \pm 0.2)$.

Let us now remark on the fact that in both diamonds in Figs. 3.8 a) and b), the inelastic cotunneling steps are not parallel to the V_{tg} axis. This slope in the cotunneling steps demonstrates that both g-factors values are voltage and thus electric-field dependent. From the reported measurements we extract $\frac{\partial g_\parallel}{\partial V_{\mathrm{tg}}} = (0.008 \pm 0.001)\frac{1}{mV}$ and $\frac{\partial g_\perp}{\partial V_{\mathrm{tg}}} = (0.007 \pm 0.001)\frac{1}{mV}$.

Below, we present an estimate of the *Rabi frequency* for this device configuration, i.e. a magnitude that tells us how efficiently a spin transition can be driven. For this purpose, we consider an oscillating voltage V_{ac} superimposed to a constant value V_{tg}. Provided that V_{ac} is sufficiently small, the dependence of $g_\parallel$ and $g_\perp$ on V_{tg} can be assumed to be linear and the Rabi frequency of the induced spin rotations reads (see appendix II)

$$\begin{aligned} f_R &= \frac{\mu_B V_{\mathrm{ac}}}{2h}\left[\frac{1}{g_\parallel}\left(\frac{\partial g_\parallel}{\partial V_{\mathrm{tg}}}\right) - \frac{1}{g_\perp}\left(\frac{\partial g_\perp}{\partial V_{\mathrm{tg}}}\right)\right] \\ &\quad \times \frac{g_\parallel g_\perp B_\parallel B_\perp}{\sqrt{\left(g_\parallel B_\parallel\right)^2 + \left(g_\perp B_\perp\right)^2}}, \end{aligned} \tag{3.9}$$

where h is the Planck constant. In this expression, $B_\parallel \equiv B_z = B\cos\theta$ and $B_\perp = B\sin\theta$, where the angle θ is measured with respect to the growth plane. Further, it can be shown that f_R is maximal if θ is chosen such that

$$\theta_{max} = \arctan\sqrt{\frac{g_\parallel}{g_\perp}}. \tag{3.10}$$

The experimental values obtained for $g_\parallel$, $g_\perp$, $\frac{\partial g_\parallel}{\partial V_{\mathrm{tg}}}$ and $\frac{\partial g_\perp}{\partial V_{\mathrm{tg}}}$, were used to estimate f_R for a given value of the Larmor frequency (f_L) and for different values of θ (see Fig.3.10).

By considering a driving frequency $f_L \approx 20$ GHz, which corresponds to $B \approx 0.9$ T applied at an angle θ_{max}, we obtain a Rabi frequency $f_R \sim 100$ MHz for $V_{\mathrm{ac}} \approx 7$ mV. Taking the lever-arm parameter of the gate electrode, $\alpha \approx 0.07$, this value of V_{ac} corresponds to an energy shift of ≈ 500 μeV, which is of the same order of typically energy-level modulations in EDSR experiments [66, 23]. We note that the estimated value for the Rabi frequency is comparable to values recently reported for electrons confined in InSb nanowires [66].

We have thus demonstrated that a single top-gate electrode, defined close to the SiGe island, may enable us to perform spin manipulations by means of the g-tensor modulation technique. Our measurements demonstrate that

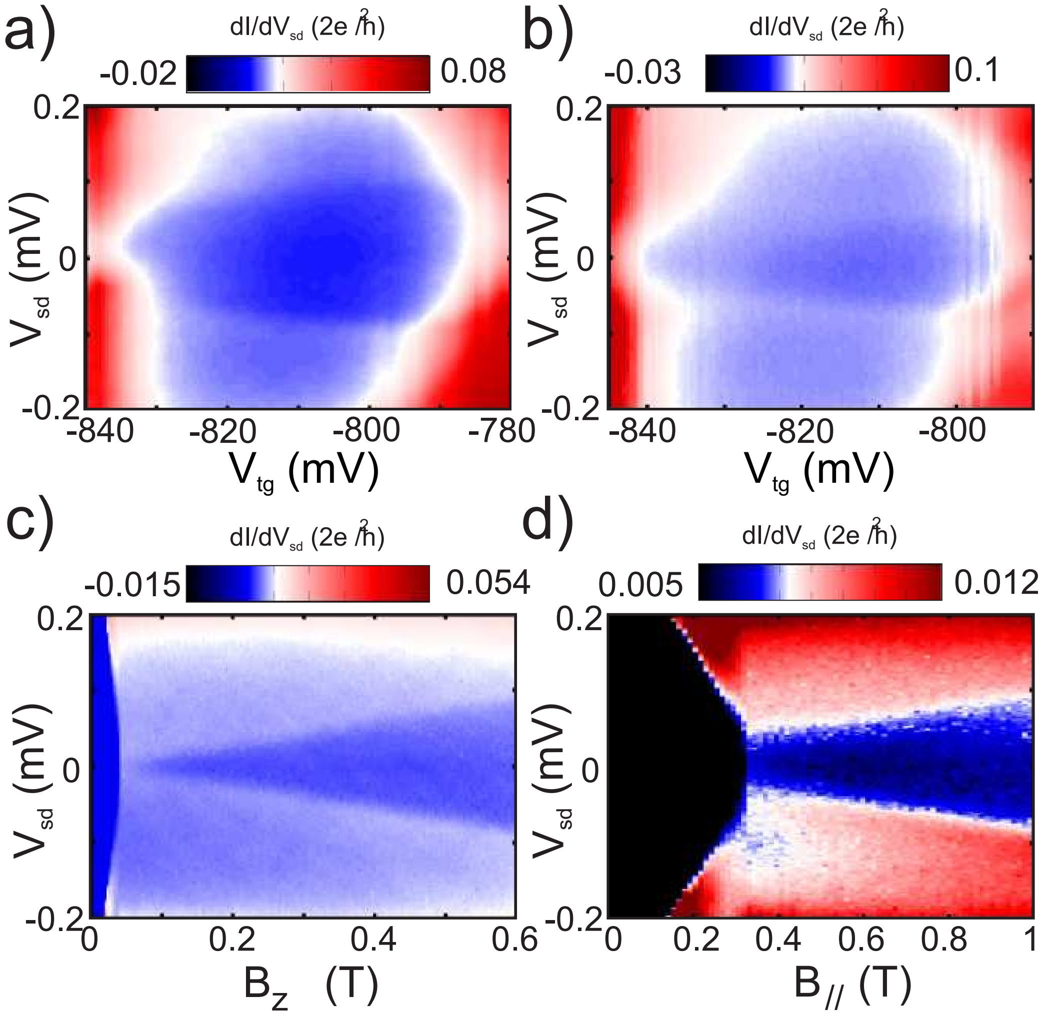

Figure 3.9: a)- b) dI_{sd}/dV_{sd} vs. V_{tg} and V_{sd} for $B = 0.6$ T, applied perpendicular and parallel to the substrate plane, respectively. c)- d) dI_{sd}/dV_{sd} vs. B and V_{sd} for perpendicular and parallel magnetic fields, respectively, demonstrating that the inelastic cotunneling steps are due to the Zeeman splitting of a spin $\frac{1}{2}$ ground state. From the measured Zeeman energies we estimate $g_\perp = (2.0 \pm 0.2)$ and $g_\parallel = (1.2 \pm 0.2)$.

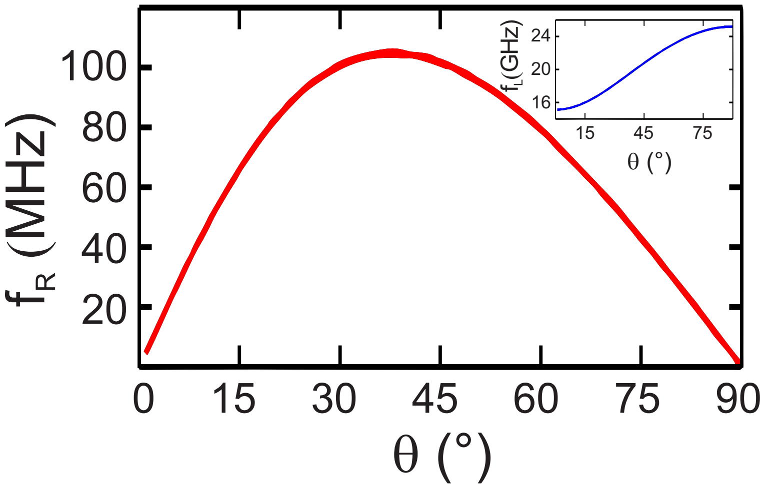

Figure 3.10: Rabi frequency dependence on the magnetic field angle with respect to the substrate plane (θ). It reaches $\sim$ 100 MHz at $\theta_{max} \approx 38°$. The estimated value corresponds to $B = 0.9$ T and $V_{ac} = 7$ mV. Inset: Larmor frequency as a function of θ for the same experimental conditions. A driving frequency of $\sim$ 20 GHz is estimated for $B = 0.9$ T.

fast Rabi frequencies can be achieved for realistic experimental conditions. The obtained values together with the expectedly long spin coherence times for carriers in Ge underline the potential of holes confined in SiGe QDs as fast spin qubits.

Chapter 4

Spin selective tunneling

To detect single-electron spins in electrical measurements, and, moreover, to distinguish between the two spin eigenstates, is undoubtedly a challenging task. A technique called *spin-to-charge conversion* permits to correlate the spin states to different charge states and, consequently, the spin state can be determined by measuring the charge on the dot [1].

Two methods for such a spin-to-charge conversion have been demonstrated experimentally; the *energy-selective read-out*, which profits from the difference in energy between spin states, and the *tunnel-rate-selective read-out*, which exploits the difference in tunnel rates of the different spin states to the contact leads [2]. The first approach is temperature limited since it requires $\Delta E_z >> k_B T$. The second approach does not have this limitation. Yet, it has only been demonstrated for two electrons in a QD, where either both electrons occupy the lowest orbital (the spin singlet state) or one of the electrons is in the first excited orbital (the spin triplet state). In this case, since the wave function in this excited orbital has more weight near the edge of the dot [30], the tunnel rate from a triplet state to the reservoir is much larger than the rate from the singlet state [67].

For single-electron spins, the realization of efficient temperature independent spin injection is needed in order to enable high-fidelity spin read-out. However, this has proven to be a very difficult task [68, 69]. Only recently, high spin-injection efficiencies were reported for ferromagnetic contacts to semiconductors [70, 71, 72]. In nanostructures, however, experimental evidence of spin injection is not as strong and clear [73, 74, 75, 76, 77].

In this chapter it is discussed that the spin-orbit interaction in the valence band, quantified by the spin-orbital splitting Δ_{SO}, provides an alternative way to obtain spin-selective tunneling without requiring ferromagnetic electrodes. The work presented in this chapter has lead to one publication [78].

4.1 Experiment

SiGe devices as the ones described in Chapter 2 were analysed. The measurements were performed in a dilution refrigerator with a base temperature of 15 mK. The stability diagram of the device is shown in the inset of Fig.4.1 a). This device has a charging energy of about $1 - 2$ meV, and the orbital level separation is some hundreds of μeV. The diamond-shape region delimited by dashed lines highlights the Coulomb blockade regime for an odd number of confined holes. While the conductance is generally suppressed within this Coulomb diamond, a conductance resonance can be identified at $V_{sd} = 0$, providing a clear signature of Kondo effect [79, 80]. The Kondo effect arises from the coherent, many-body interaction between a localized spin and the surrounding Fermi seas of the metal contacts. At finite B, this resonance is split into two peaks at $eV_{sd} = \pm g\mu_B B$ [81]. This splitting is observed in Figs.4.1 b) and c) for perpendicular and parallel B, respectively.

For perpendicular B (Fig.4.1 a)), the splitting of the Kondo peak is clearly asymmetric with respect to a sign change in V_{sd}. The asymmetry in G arises at the onset of inelastic cotunneling (i.e., for $|eV_{sd}| > \Delta E_Z$). For parallel B, however, the asymmetry is practically absent (Fig.4.1 b)).

To further investigate this anisotropy, a sequence of $G(V_{sd})$ traces was taken while rotating a 3 T field in a plane perpendicular to the substrate. The resulting data, $G(\theta, V_{sd})$, are shown in Fig.4.1 c), with θ being the angle between the magnetic field and the substrate plane. Along with a variation in the Zeeman splitting of the Kondo peak, caused by the θ-dependent hole g factor [13], the asymmetry becomes progressively more pronounced when going from $\theta = 0°$ (or 180°) towards $\theta = 90°$.

The asymmetry observed in $G(V_{sd})$ can be quantified by $A = \frac{G_- - G_+}{G_- + G_+}$, where $G_\pm = G(\pm\Delta E_Z/e)$. The detailed $A(\theta)$ dependence, extracted from Fig.4.1 c), is shown in Fig.4.2 a). $A \approx 0$ for $\theta = 0°$ (or 180°) and it increases monotonically up to 0.2 for θ approaching 90°; the $A(B)$ dependence is shown in Fig.4.2 b). By sweeping the magnetic field from negative to positive values (see insets in Fig.4.2 b)), we further observe that the asymmetry A obeys the relation

$$A(B_Z) = A(-B_Z). \tag{4.1}$$

The same qualitative behaviour described above was observed in another device, which did not display Kondo effect (see Fig.4.3). The asymmetry A reaches 0.4 at 3 T for that device. To exclude experimental artifacts, we verified that A changes sign upon exchanging the source and drain leads.

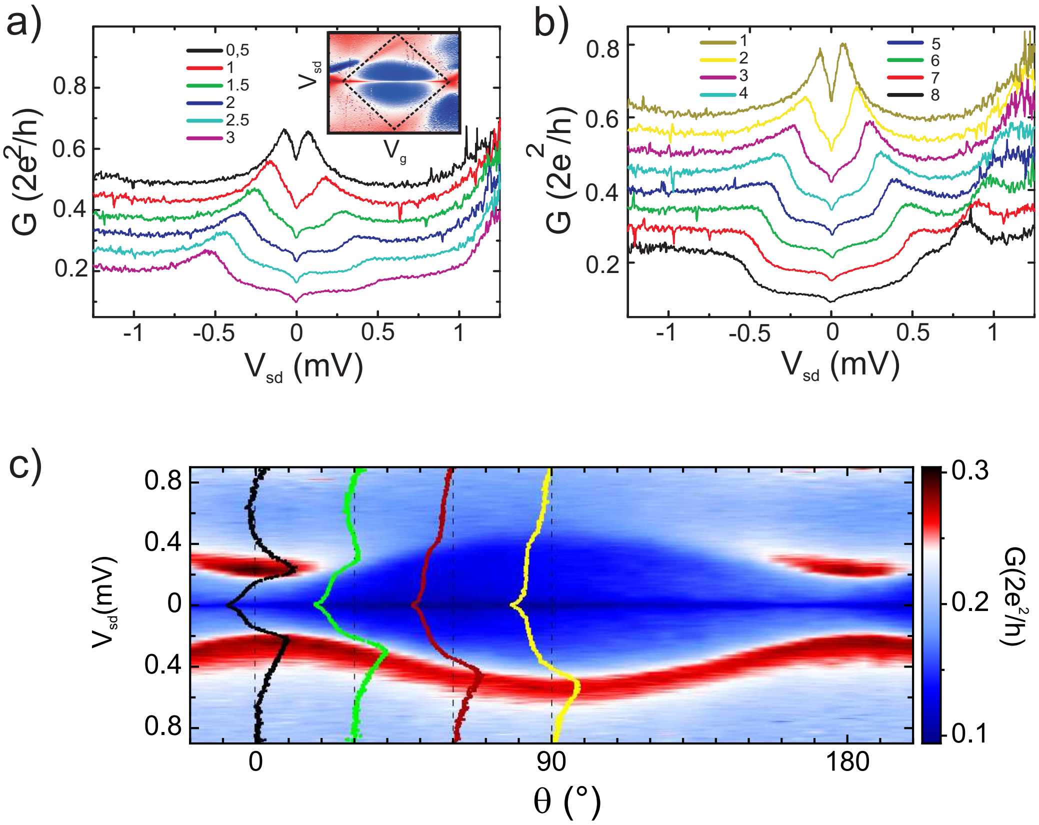

Figure 4.1: a) $G \equiv dI_{sd}/dV_{sd}$ for different perpendicular magnetic fields from 0.5 to 3 T. The traces have been vertically shifted by $0.06 \times 2e^2/h$ for clarity. Inset: $G(V_g, V_{sd})$ for a 75 mT perpendicular field needed to suppress the superconductivity of the Al electrodes. (V_g spans a range of 850 mV and V_{sd} ranges from -3.5 to 3.5 mV.) b) $G(V_{sd})$ for different parallel fields from 1 to 8 T. The traces have been shifted by $0.06 \times 2e^2/h$ for clarity. The Zeeman splitting of the Kondo peak is asymmetric in a) and symmetric in b). c) Angular dependence of the split Kondo peak for a fixed V_g and $B = 3$ T. Superimposed $G(V_{sd})$ traces for $\theta = 0°$, $30°$, $60°$, and $90°$. The V-shape dip of G at zero bias observed in a)-c) is caused by electron-electron interactions in the disordered leads [82, 83].

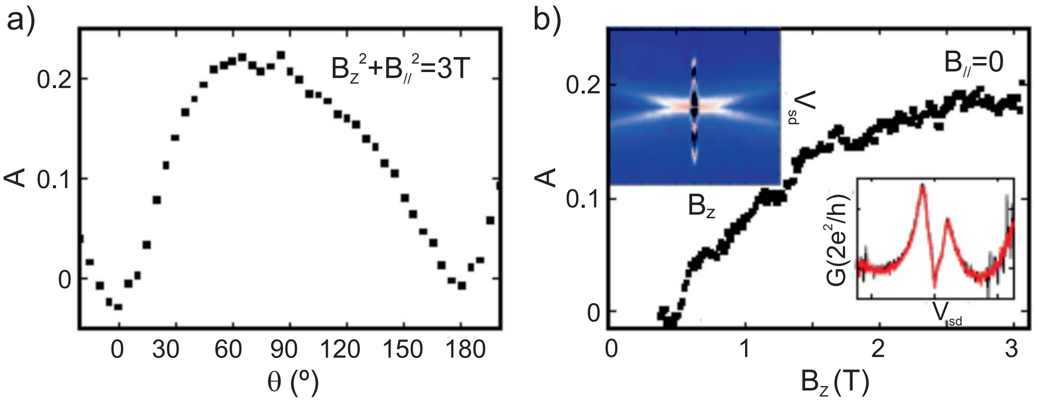

Figure 4.2: Asymmetry parameter A as a function of a) θ and b) perpendicular B. We note that, by subtracting the elastic cotunneling contribution from $G(V_{sd})$, A becomes larger than 0.5. The top inset in b) shows the evolution of the Kondo peak while sweeping B_Z from -1 to $1T$. The lower inset shows two characteristic line traces taken at -1 T (red) and 1 T (black) demonstrating that $A(B_Z) = A(-B_Z)$.

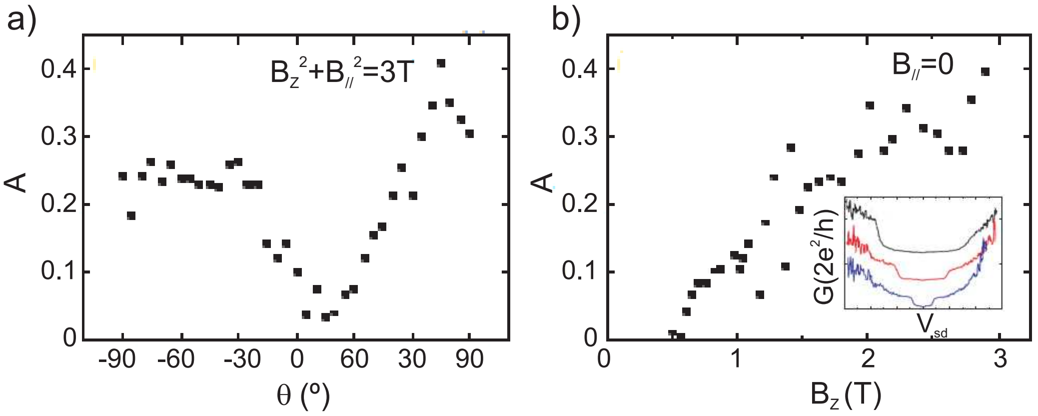

Figure 4.3: Asymmetry parameter A as a function of a) θ and b) perpendicular magnetic field, B_z. The inset shows characteristic traces of G vs. V_{sd} for $\theta = 20°$ (blue), $45°$ (red) and $90°$ (black), respectively. The traces have been shifted by $0.06 \times 2e^2/h$ for clarity.

4.2 Analysis

In order to understand the microscopic origin of the measured effect, we consider the 2D limit of the Luttinger Hamiltonian just as in Chapter 3. Focusing on the first HH subband (see appendix I, Eq.24), we obtain by perturbation theory:

$$\begin{aligned}
\Phi_1(\boldsymbol{r}) &= \frac{\sqrt{2}\gamma_3}{m}\mathcal{U}_- k_- \psi_h(x,y)\sum_n f_n^l(z)\frac{\langle f_n^l|\, k_z \,|f_1^h\rangle}{E_1^h - E_n^l}, \\
\chi_1(\boldsymbol{r}) &= \mathcal{U}_-\psi_h(x,y) f_1^h(z) + \frac{2\gamma_3}{m} Z k_- \psi_h(x,y) \\
&\quad \times \sum_n f_n^l(z)\frac{\langle f_n^l|\, k_z \,|f_1^h\rangle}{E_1^h - E_n^l},
\end{aligned} \tag{4.2}$$

and similar expressions for $\Phi_2(\boldsymbol{r})$ and $\chi_2(\boldsymbol{r})$, obtained from Eq. (4.2) by replacing $\mathcal{U}_- \to \mathcal{U}_+$, $k_- \to k_+$, and $\psi_h(x,y) \to \psi_h^*(x,y)$.

In our notation, $\mathcal{U}_\pm = \mp\frac{1}{\sqrt{2}}(X \pm iY)$ and $k_\pm = \mp\frac{1}{\sqrt{2}}(k_x \pm ik_y)$. The Bloch amplitudes X, Y, and Z describe the valence band in the absence of spin-orbit interaction. In blocks H_{hh} and H_{ll}, the motion along z separates; we denote the corresponding eigenenergies and eigenfunctions by $E_n^{h/l}$ and $f_n^{h/l}(z)$, respectively.

The tunneling amplitudes $t^i_{\sigma s}$ are found as

$$t^i_{\sigma s} = \sum_{u=X,Y,Z} T_u \langle u,\sigma|\Psi_s(\boldsymbol{r}_i)\rangle\,, \tag{4.3}$$

where T_u is the coupling strength between Bloch amplitude u and the lead, and $\langle u,\sigma|\Psi_s(\boldsymbol{r}_i)\rangle$ are the projections of the QD eigenstates $\Psi_s(\boldsymbol{r})$ (see appendix I, Eq.24), onto the product state of Bloch amplitude u and spinor $|\sigma\rangle$. The tunneling amplitudes in Eq. (4.3) depend on the point of tunneling, $\boldsymbol{r}_i = \boldsymbol{r}_L, \boldsymbol{r}_R$, the component of the true spin in the lead, $\sigma = \uparrow, \downarrow$, and the component of the *Kramers doublet* [1] on the dot, $s = \Uparrow, \Downarrow$. We remark that T_X, T_Y, and T_Z appear in Eq. (4.3) as phenomenological parameters. They depend on the details of the metal-semiconductor interface and cannot be determined within the theory used here. We find

$$t^i_{\sigma s} \propto \begin{pmatrix} \bar{\Phi}_1(\boldsymbol{r}_i) & \bar{\chi}_2(\boldsymbol{r}_i) \\ \bar{\chi}_1(\boldsymbol{r}_i) & \bar{\Phi}_2(\boldsymbol{r}_i) \end{pmatrix}, \tag{4.4}$$

---

[1] Kramers doublets are pairs of Bloch states that are spin-degenerate

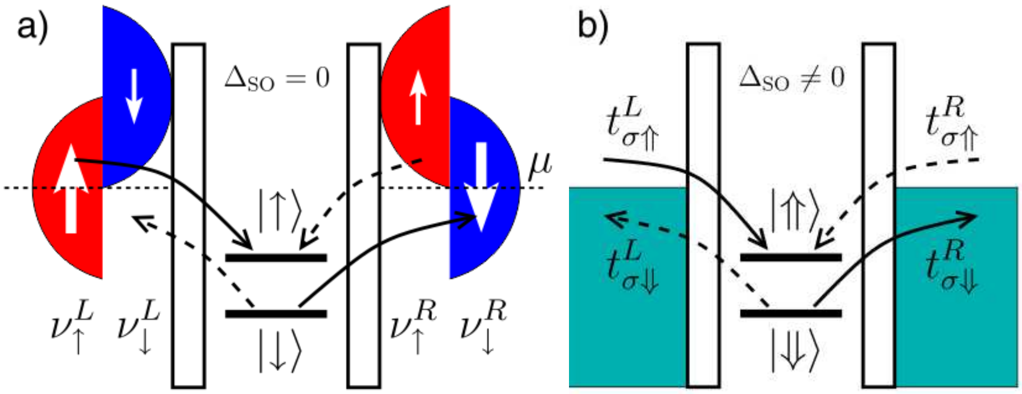

Figure 4.4: Spin-selective tunneling in a) a QD coupled to ferromagnetic leads and b) a QD with spin-orbit interaction coupled to non-magnetic leads. The solid (dashed) arrows indicate the tunneling processes involved in the inelastic cotunneling for forward (reverse) biasing, with solid (dashed) arrows representing stronger (weaker) tunnel rates. In both a) and b), the tunnel rate, $\Gamma \equiv \pi\nu\,|t|^2$, differs for each Zeeman sublevel of the QD. In setup a), it is the density of states ν that brings about the spin selectivity of the tunneling. In setup b), the spin selectivity is caused by the tunneling amplitude t, which is sensitive to the spinor wave functions at the point of tunneling. In the valence band, for energies $\lesssim \Delta_{SO}$, the B-field efficiently makes Γ spin-dependent by affecting the mixing between heavy and light holes. Since the inelastic cotunneling current is proportional to $\Gamma^L_\Uparrow\Gamma^R_\Downarrow$ for the forward bias and to $\Gamma^R_\Uparrow\Gamma^L_\Downarrow$ for the reverse bias, an asymmetric $G(V_{sd})$ is expected whenever $\Gamma^L_\Uparrow\Gamma^R_\Downarrow \neq \Gamma^R_\Uparrow\Gamma^L_\Downarrow$.

where $\bar{\Phi}_i(\boldsymbol{r})$ and $\bar{\chi}_i(\boldsymbol{r})$ are obtained from Eq. (4.2) by replacing $Z \to T_Z$ and $\mathcal{U}_\pm \to \mp\frac{1}{\sqrt{2}}(T_X \pm iT_Y)$.

The spin selectivity of the tunneling is best seen in the matrix of the tunnel rates, $\Gamma_{ss'} = \pi\sum_\sigma t^*_{\sigma s}\nu_\sigma t_{\sigma s'}$. With $\nu_\uparrow = \nu_\downarrow$ (case of non-ferromagnetic leads) we find, up to a common factor,

$$\begin{pmatrix} \Gamma_{\Uparrow\Uparrow} & \Gamma_{\Uparrow\Downarrow} \\ \Gamma_{\Downarrow\Uparrow} & \Gamma_{\Downarrow\Downarrow} \end{pmatrix} \propto \begin{pmatrix} \left|\bar{\Phi}_1\right|^2 + |\bar{\chi}_1|^2 & \bar{\Phi}^*_1\bar{\chi}_2 + \bar{\chi}^*_1\bar{\Phi}_2 \\ \bar{\Phi}^*_2\bar{\chi}_1 + \bar{\chi}^*_2\bar{\Phi}_1 & \left|\bar{\Phi}_2\right|^2 + |\bar{\chi}_2|^2 \end{pmatrix}. \tag{4.5}$$

At $B = 0$, time-reversal symmetry requires that

$$\Phi_2(\boldsymbol{r}) = [\Phi_1(\boldsymbol{r})]^* \quad \text{and} \quad \chi_2(\boldsymbol{r}) = -[\chi_1(\boldsymbol{r})]^*, \tag{4.6}$$

leading to $\Gamma_{\Uparrow\Uparrow} = \Gamma_{\Downarrow\Downarrow}$ and $\Gamma_{\Uparrow\Downarrow} = \Gamma_{\Downarrow\Uparrow} = 0$ in Eq. (4.5).

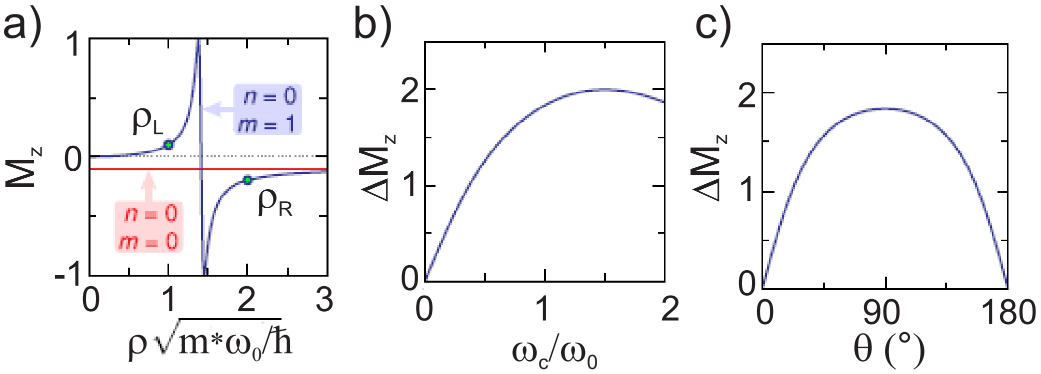

Figure 4.5: a) Tunneling polarization M_z as a function of the space coordinate ρ for two Fock-Darwin states (n, m) as indicated and for $\omega_c = 0.1\omega_0$. b) B-field dependence of the difference $\Delta M_z = M_z(\rho_L) - M_z(\rho_R)$, for the values of ρ_L and ρ_R indicated in a). c) ΔM_z as a function of θ for a fixed value of $|\boldsymbol{B}|$. The value of $|\boldsymbol{B}|$ corresponds to $\omega_c = \omega_0$ at $\theta = 90°$.

At $B \neq 0$, however, the orbital effect of the B-field modifies the functions $\Phi_i(\boldsymbol{r})$ and $\chi_i(\boldsymbol{r})$, such that the relations in Eq. (4.6) are no longer satisfied. In general, the matrix $\Gamma_{ss'}$ has nonzero off-diagonal elements.

Since it is a hermitian matrix, there exists a direction in space, $\boldsymbol{M}$, such that a rotation of the quantization axis to the direction of $\boldsymbol{M}$ makes the rate matrix diagonal, $\Gamma = \mathrm{diag}(\Gamma_\Uparrow, \Gamma_\Downarrow)$, with $\Gamma_\Uparrow \geq \Gamma_\Downarrow$. To quantify the spin selectivity of the tunneling, we define

$$|\boldsymbol{M}| = \frac{\Gamma_\Uparrow - \Gamma_\Downarrow}{\Gamma_\Uparrow + \Gamma_\Downarrow}. \tag{4.7}$$

In respect to transport, $\boldsymbol{M}$ is analogous to the polarization vector of the ferromagnetic lead. Indeed, the maximum of spin selectivity in tunneling from a ferromagnet is achieved when the ferromagnet is a half-metal, *e.g.*, $\nu_\uparrow \neq 0$ and $\nu_\downarrow = 0$. This extreme case corresponds to $M = 1$ and can be approached in our case by increasing B_z.

It is interesting to note that the transport characteristics of a QD with spin-orbit interaction coupled to normal leads are similar to those of a QD without spin-orbit coupled to ferromagnetic leads [84, 85, 86]. We depicted this similarity in Fig.4.4, where we consider the simplest case, in which the Zeeman interaction and the two spin-dependent tunnel contacts have collinear quantization directions.

In order to illustrate the origin of the spin selectivity, we focus on the special case: $T_X = T_Y = 0$ and $T_Z \neq 0$ and refer to this tunneling model as the Z-model. In the Z-model, vector $\boldsymbol{M}$ is parallel to the z-axis. Tunneling to the hole states is possible only due to the admixture of the light hole subbands.

Furthermore, in this model, the spin selectivity is determined by the fact that $\bar{\chi}_1(\boldsymbol{r}) \propto k_- \psi_h(x, y)$ and $\bar{\chi}_2(\boldsymbol{r}) \propto k_+ \psi_h^*(x, y)$, whereas $\bar{\Phi}_i(\boldsymbol{r}) \equiv 0$. Using this information in Eqs. (4.5) and (4.7), we specify $\psi_h(x, y)$ to the Fock-Darwin states [87]. Therefore, we assume that $U(x, y)$ in Eq. (6.2) is given by $U(\rho) = m^* \omega_0^2 \rho^2/2$, where m^* is the effective mass for in-plane motion, ω_0 is the oscillator frequency of the harmonic potential, and $\rho^2 = x^2 + y^2$.For the first two states ($n = 0$ and $m = 0, -1$), we obtain

$$M_z = -\frac{\omega \omega_c}{\omega^2 + \omega_c^2/4}, \tag{4.8}$$

where $\omega = \sqrt{\omega_0^2 + \omega_c^2/4}$, and $\omega_c = eB_z/m^* c$. For these states, M_z depends on B_z but not on ρ, see Fig.4.5 a). For $B_z \neq 0$, the contacts will exhibit spin-dependent tunnel rates with the same polarization value M_z regardless of the point-tunneling position. In such a case, no asymmetry in the inelastic cotunneling is expected.

For higher energy levels, M_z may depend on ρ,

$$M_z = \left[\frac{\omega}{\omega_c} f(\rho) + \frac{\omega_c}{4\omega} \frac{1}{f(\rho)} \right]^{-1}, \tag{4.9}$$

where $f(\rho)$ is given for arbitrary integers n and m. We consider further the state $n = 0$ and $m = 1$, for which $f(\rho) = 2\hbar/(m^* \omega \rho^2) - 1$.

Now M_z depends both on B_z and on ρ, see Fig.4.5 a). The spin polarization of two contacts positioned arbitrarily on a QD may differ significantly from each other, see, *e.g.*, points ρ_L and ρ_R in Fig.4.5 a). The asymmetry in the inelastic cotunneling is related to $\Delta M_z = M_z(\rho_L) - M_z(\rho_R) \neq 0$. ΔM_z increases with B_z (Fig.4.5 b)), displaying at the same time strong dependence on the B-field direction (Fig.4.5 c)), in good qualitative agreement with the results in Fig.4.2.

Our theory also explains the symmetry relation in Eq. (4.1). On the one hand, the spin-selective part of $\Gamma_{ss'}$ is proportional to B_z and therefore it changes sign when flipping the direction of the magnetic field. On the other hand, the Zeeman energy also changes sign when flipping the direction of the magnetic field, exchanging thus the roles of the ground and the excited state. Therefore, A does not change upon $B \to -B$.

To summarize, in spite of a predominant heavy hole character, symmetry considerations on the constituent Bloch functions imply that, for a realistic device geometry, tunneling to and from the QD states take place via the light hole wave functions. Since light holes cannot be factorized into orbital and spin components, an applied magnetic field induces a spatial variation in the relative orbital weights of the two spin species. Therefore, the ratio of tunneling amplitudes for up and down spins will depend on the position of the contacts. In a 2D geometry, this effect is highly anisotropic since only a perpendicular field has an effect on the orbital motion.

The described joint effect of spin-orbit coupling and Zeeman splitting explains our experimental findings and it may allow for spin read-out in single dot devices. Yet, the spin-selectivity that we have measured appears to be too low to permit a high fidelity read-out. Other types of device functionalities may nevertheless base on it, such as the Rabi spin pump to be discussed in Chapter 5.

Chapter 5

A Rabi electron pump

Charge pumping has been realized in diverse nanoscale devices [88, 89, 90, 91, 92, 93, 94, 95]. In this chapter, an electron pump based on the spin selectivity discussed in Chapter 4 is presented.

This electron pump scheme relies on the asymmetric tunnel couplings that different spin species can experience; see Fig.5.1. Let us assume a QD in a magnetic field of a few T, to be tuned to a Coulomb blockade regime for a spin-1/2 ground state. For $V_{sd} = 0$, no current flows through the QD, which is to a large probability in its spin-down ground state. By means of ESR techniques, the $\Uparrow$ state can be populated as a result of coherent spin rotations. Most likely, inelastic relaxation back to the ground state will occur through an inelastic cotunneling process. Because $\Uparrow$ and $\Downarrow$ states can have tunnel couplings with opposite asymmetries, in a configuration such as the one depicted in Fig.5.1, the most favourable cotunneling relaxation process would involve the transfer of a charge carrier from the right to the left contact. The ESR signal plays the role of the bias in a normal inelastic cotunneling process and hence a net DC current could be driven by a continuous resonant irradiation.

We have fabricated InAs/InP core/shell nanowire (NW) devices for this experiment, as the growth of SiGe islands was going through some difficulties. The scheme is, in any case, applicable to any material system that experiences a strong spin orbit coupling. Yet, as electrons instead of holes are confined in the NWs, the mechanism responsible for the asymmetry in the conductance is of a different origin than the one relevant for SiGe quantum dots.

As discussed in Chapter 4, in the case of SiGe quantum dots, spin-selective tunneling is ultimately a consequence of the inherent spin-orbit mixing of the light-hole components in the QD wavefunctions. This mechanism works for both central-symmetric crystals and non-central-symmetric ones, and refers solely to the valence-band carriers.

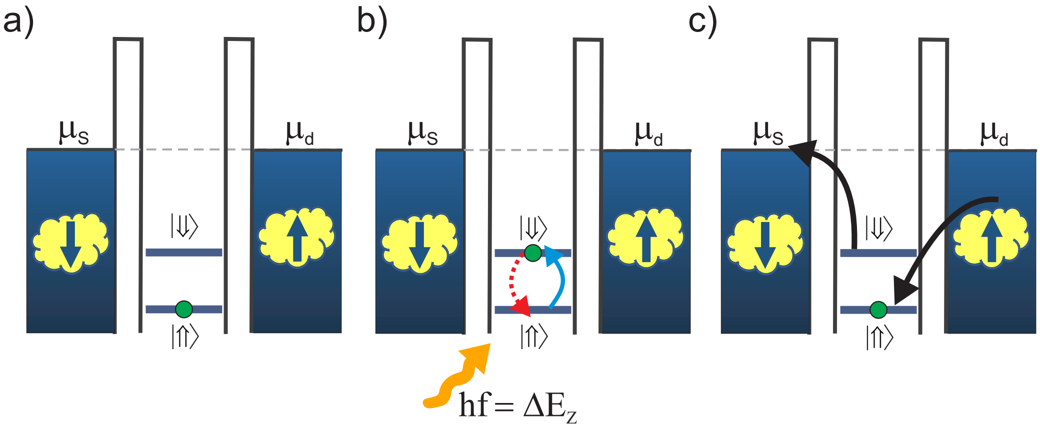

Figure 5.1: Operating principle of a Rabi electron pump. We consider the Coulomb blockade condition for a spin-1/2 ground state. A finite B is applied to split the Kramers degeneracy of the ground state and establish an asymmetric coupling of the two (pseudo)spin states. a) At zero-bias and without any external excitation, the QD is in its lowest energy spin state, $\Uparrow$, and no current is expected across the QD. b) A resonant RF field, at frequency $f = \Delta E_Z/h$, is capable of inducing coherent oscillations such that the excited spin state, $\Downarrow$, can be occupied with a sizeable probability. c) The excited spin state can decay through spin-flip cotunneling processes. Due to the asymmetric couplings, one type of cotunneling process (shown in the figure) will be favoured leading to net current across the QD.

In contrast, spin-selective tunneling for conduction-band electrons relies on a different type of spin-orbit interaction. This spin-orbit interaction arises from the fact that an electron moving through the solid experiences an alternating electric field due to the periodic lattice potential. In the reference frame that moves together with the electron this alternating electric field is 'felt' by the electron as a magnetic field and it gives rise to spin precession. In the absence of external magnetic fields, this spin precession is bound precisely to the orbital motion of the electron; two electrons, one moving forward and one backward at a constant average speed, undergo similar spin precessions in opposite directions. Thus, in a bound state consisting of equal amount of forward and backward propagating waves, the net effect of the spin-orbit interaction is cancelled exactly, and hence it does not result in spin-selective tunneling. In a magnetic field that breaks time reversal symmetry the situation is different. The spin precession for forward and backward motion of the electron is not exactly opposite. Spin-orbital mixing can thus lead to spin-dependent tunnel probability and to an asymmetric conductance.

This mechanism is possible only in materials that lack crystal inversion symmetry. To distinguish between spin-orbit terms originating from the bulk inversion asymmetry (BIA) and the structure inversion asymmetry (SIA), the terms Dresselhaus spin-orbit interaction and Rashba spin-orbit interaction are often used [2].

Spin-selective tunneling for conduction-band electrons has been studied both experimentally [96] and theoretically [97]. In [98], a generic model for spin-selective tunneling, comprising both the case of holes and electrons, has been given.

Besides the different mechanisms involved, the operating principle of this Rabi pump applies to any QD system displaying an asymmetric cotunneling conductance. This is why, to provide an experimental demonstration of this device concept, we used InAs-based NWs.

5.1 Device description

The devices were fabricated from individual InAs/InP core/shell NWs with a total diameter of approximately 30 nm, grown by thermal evaporation. The InP shell is about 2 nm thick and it acts as a confinement barrier resulting in an enhanced mobility of the one-dimensional electron gas in the InAs core (see Fig.5.2) [99].

On an undoped silicon substrate with a SiO_2 surface layer, a set of alignment crosses, fine alignment markers and bottom-gate electrodes are defined by a 100 kV ebeam writer. In a subsequent step, the bottom gates are cov-

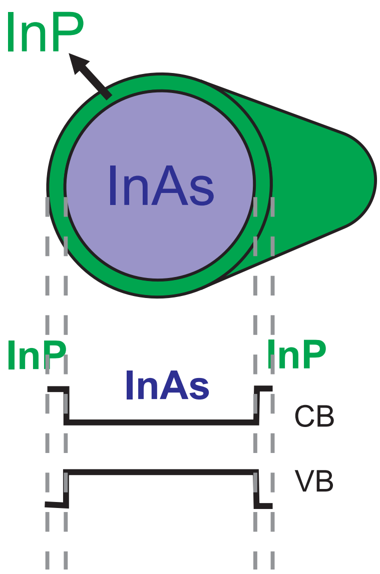

Figure 5.2: InAs/InP core/shell nanowire and corresponding conduction-band (CB) and valence-band (VB) profiles along a radial direction.

ered by a 10-nm-thick hafnia layer deposited by atomic-layer deposition. The NWs are randomly dispersed on this pre-fabricated substrate and imaging of the write field inner areas is performed using a 5 kV electron beam (see Fig.5.3 a)).

NWs crossing the prefabricated bottom-gate electrodes are then contacted by means of source/drain metal electrodes. At the same time, metal connections between the necessary bottom gates and outer bonding pads are realized. An example of the designed pattern is shown in Fig.5.3 b). This design is exposed at 100 KV and 1 nA on PMMA 4% spun at 6000 rpm, 2000 rpm/s for 30 s and baked for 5 min at 180° C. The development of the exposed resist, 30 s MIBK:IPA $1:3+1$ min IPA, is followed by an argon milling at 250 V for 45 s in order to remove native oxides from the NW's surface. This argon milling takes place inside the evaporator, where a metal layer of Ti/Au 2.5/45 nm is deposited right after. Lift-off in hot acetone is afterwards performed. A SEM image of a finalized device is shown in Fig.5.4 a).

A QD is naturally formed in the NW section between the source and drain contacts. A scheme of the device is shown in Fig.5.4 b). Gate electrodes on the sides, lg and rg, permit the tuning of the tunnel barriers while the central gate, cg, is used as a plunger gate to control the electrostatic potential and hence the charge state of the QD.

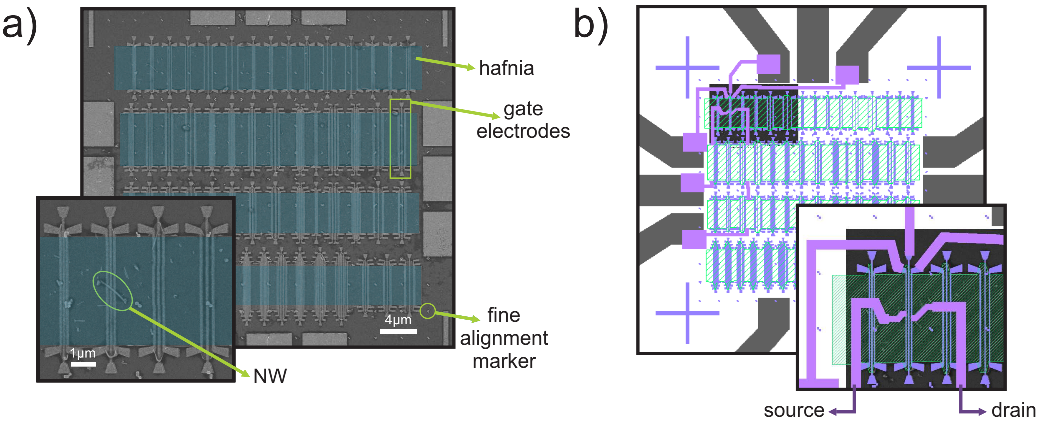

Figure 5.3: a) SEM image of a write field inner area. Different sets of gate electrodes are covered by a thin layer of hafnia, artificially coloured in the image in order to improve the contrast. A NW laying on top can be distinguished by zooming-in (inset). b) Source and drain leads and connections of the gate electrodes to the write field inner pads designed on the aligned SEM image. The design software is again KLayout. Inset: zoom-in on the device design.

The magnetic field B, essential for the realization of the proposed scheme, was applied at 30° from the substrate plane. Having both parallel and perpendicular components of B, enables us to fulfil the conditions for the achievement of coherent spin rotations both by means of EDSR and electric g-tensor modulation [1] (see Chapter 3).

5.2 Experiment

According to the scheme in Fig.5.1, electrons can be transported from source to drain by applying a signal at a frequency such that $hf = \Delta E_Z$ where h is Planck's constant. An *Anritsu* radio frequency (RF) signal generator MG3690C was used in order to generate a microwave modulation of the gate voltage applied to the central gate electrode.

The high frequency signal is guided by coaxial lines installed in the dilution refrigerator. These lines are connected to a specially designed sample holder equipped with SMP connectors (Fig.5.5). The SiO_2/Si chip with NW devices is mounted on this sample holder. Central-gate electrodes are connected both to DC and RF lines. All transport measurements were carried

---

[1] It has been shown that the g-tensor in InAs NWs is highly anisotropic [100]

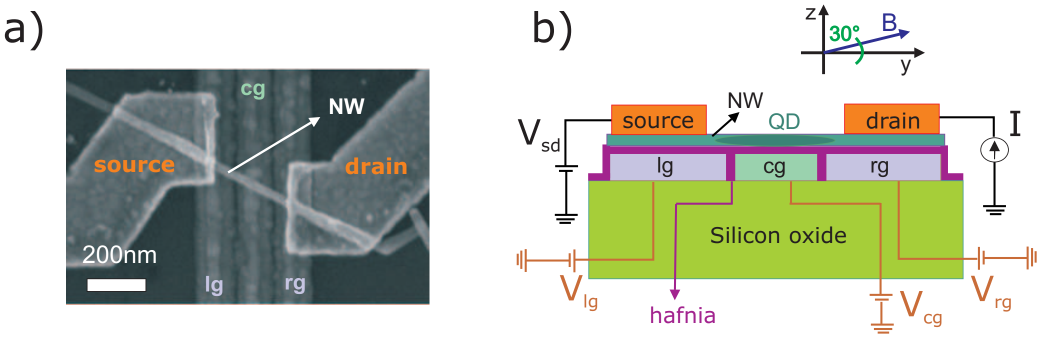

Figure 5.4: a) SEM image of the NW device. The gap between the source and the drain is about 250 nm. b) Schematics of the device, lg being the side gate on the left and rg the one on the right, both designed to allow the tuning of the tunnel barriers. cg is the central gate dedicated to shift the energy levels of the QD. A magnetic field B was applied at 30° from the substrate plane.

out in a dilution refrigerator at a base temperature of 15 mK.

Following the scheme in Fig.5.1, the QD should be tuned in a Coulomb blockade regime corresponding to a spin-1/2 ground state. A Coulomb diamond for $B = 0$ is shown in Fig.5.6 a). The charging energy, which defines the extension of the diamond along the V_{sd} axis, is around 5 meV. Therefore, the central low-conductance (blue) region in Fig. 5.6 a) corresponds just to the low-V_{sd} portion of the Coulomb diamond. V_{rg} and V_{lg} were tuned in such a way that a small cotunneling contribution could be observed; $V_{rg} = -500$ mV, $V_{lg} = -535$ mV.

Steps in dI/dV_{sd} appear for a static $B = 130$ mT (see Fig.5.6 b)), denoting the onset of inelastic cotunneling processes. These processes correspond to spin excitations of the QD. In order to verify this, we have measured the B-evolution of the cotunneling steps. The results are shown in Fig. 5.7 LEFT, where the dI/dV_{sd} is measured as a function of (B, V_{sd}) for three different values of V_{cg} taken inside the odd Coulomb diamond.

Fig.5.7 LEFT shows how the inelastic-cotunneling steps move apart linearly with B, following the expected behaviour for a spin doublet. Given $\Delta E_z = g\mu_B B$, $g = (11.5 \pm 0.7)$ is extracted from these three measurements.

Fig.5.7 RIGHT shows a $dI/dV_{sd}(V_{sd})$ trace at fixed B from each measurement on the left. These characteristics appear to have the desired asymmetry. In Chapter 4, the asymmetry in the $dI/dV_{sd}(V_{sd})$ characteristic was defined as $A = (G_- - G_+)/(G_+ + G_-)$, where $G \equiv dI_{sd}/dV_{sd}$ and $G_\pm = G(\pm\Delta E_z/e)$. Interestingly, the asymmetry in the characteristics shown in Fig.5.7 RIGHT,

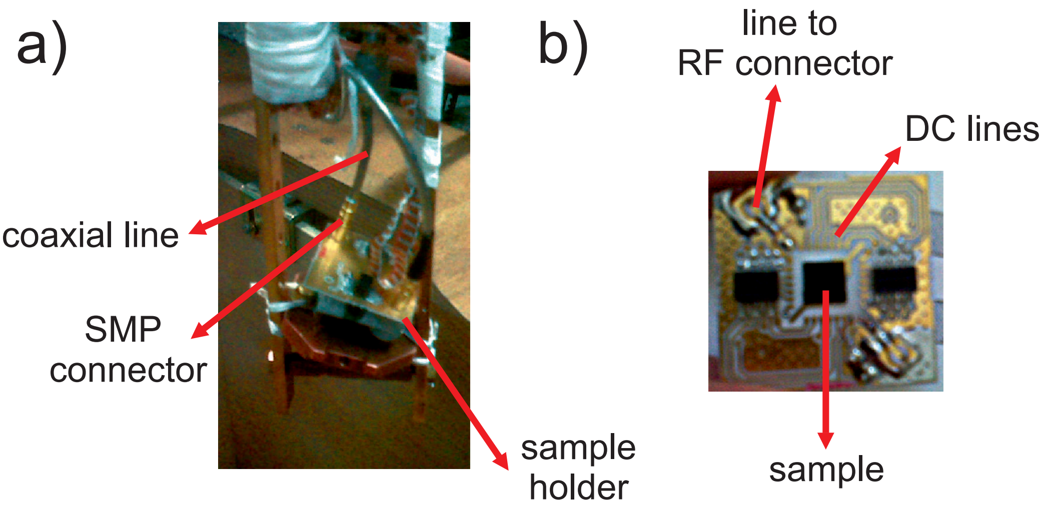

Figure 5.5: a) Coaxial lines assembled by SMP connectors to the PCB board that serves as sample holder. b) Top view of the chip carrier. 24 DC lines are accessible, two of them connected to a RF line.

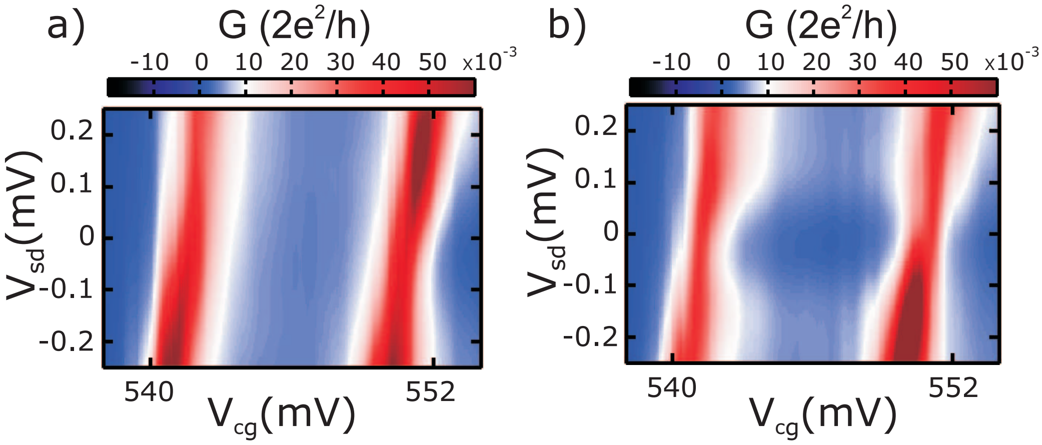

Figure 5.6: a) dI/dV_{sd} as a function of V_{cg} and V_{sd} for $B = 0$, $V_{rg} = -500$ mV and $V_{lg} = -535$ mV. b) Same as a) for $B = 130$ mT. Inelastic cotunneling steps in conductance are evidenced.

varies in modulus and sign with V_{cg}.

A fixed value of V_{cg} corresponding to $A > 0$ was chosen to test the operating principle of the Rabi electron pump. This test was conducted as follows.

The bias voltage was set precisely to zero, after evaluating the offset voltage of our DC voltage source. This way, with no RF power applied, the source-drain current was below the noise threshold. The integration time used was 10 PLC (power line cycles) and the current noise level in this case was below 2 pA.

The RF power was then turned on and set to a fixed frequency. While monitoring the current flow through the device, B was swept; whenever the Zeeman energy would coincide with the frequency of the applied RF signal, a finite current would be observed. Noteworthy, the alternative option of sweeping the frequency of the RF signal and fixing B was discarded due to the presence of transmission resonances in the coaxial lines. To perform the experiment, we have thus chosen a RF power and a set of frequencies for which the transmission amplitudes were similar. The RF power was set to -10 dBm [2].

It is also important to remark that the current measured in resonance depends on the spin selectivity of the contacts, and thus, it is typically in the order of a few pA. In order to distinguish this signal from the back-ground level, an averaging of many current traces is needed. From the average of 10 consecutive traces, measured by sweeping B back and forth between -300 and 300 mT at a rate of 2.3 mT/s, we could observe a sizeable current consisting of peak-shape structures superimposed on a rather featureless background level.

The results are shown in Fig.5.8 a) LEFT, after having removed the background current. For each RF frequency we observe three peaks. The outer peaks move apart proportionally to the RF frequency. This is clearly shown in Fig.5.8 a) RIGHT, where the half-distance $\Delta B(f)$ between the outer peaks is plotted against f. From a linear fit to the relation $\Delta B = \frac{hf}{g\mu_B}$ we extract an electron g-factor of (10.6 ± 0.9). This value agrees with the value extracted from a linear fit of the field-induced splitting of the inelastic cotunneling steps in Figs.5.7 a) to c) ($g = (11.5 \pm 0.7)$).

Besides the outer peaks, expected from the spin resonance, an additional peak of comparable height is found approximately in the middle. The existence of this central peak may have to do with a nuclear-polarization effect, but the exact mechanism remains currently unclear.

---

[2] Considering the attenuation of the high frequency signal along the coaxial lines, we estimate that the RF power reaching the cg was about -50 dbm.

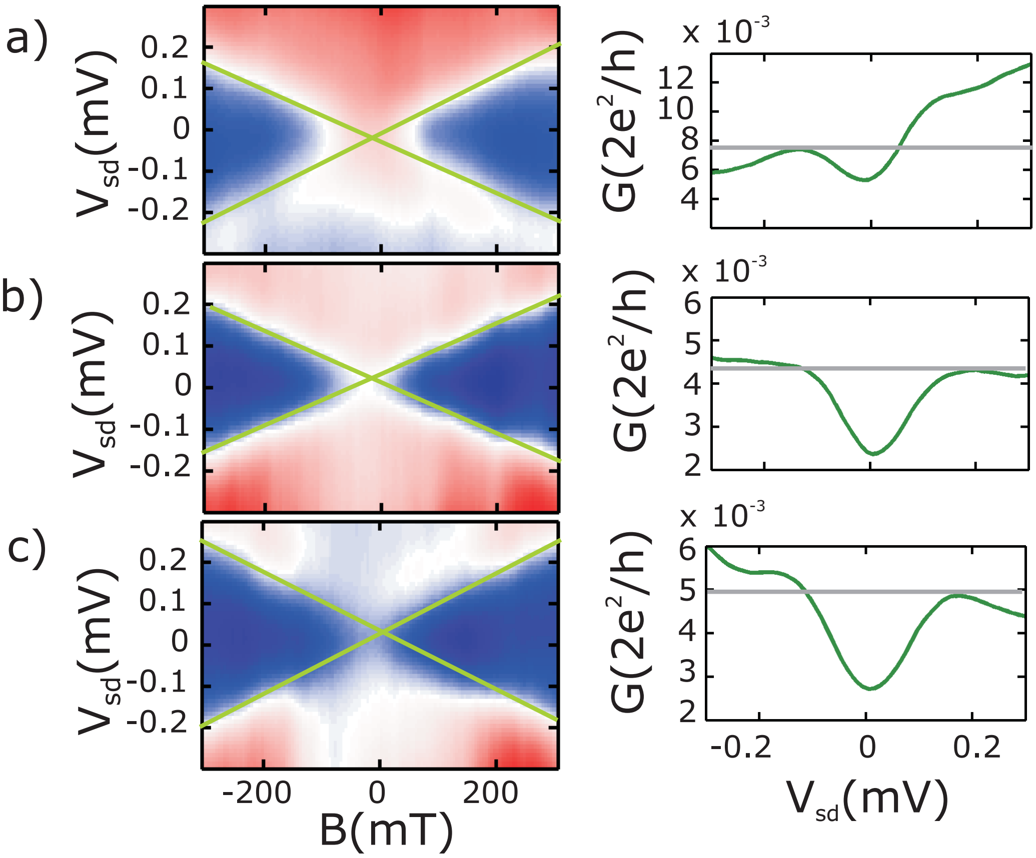

Figure 5.7: LEFT: G as a function of V_{sd} and B for different V_{cg} values: a) V_{cg} = 543.6 mV, b) V_{cg} = 547 mV and c) V_{cg} = 549 mV. Green lines are added as a guide to the eye. The extracted g-factor value is $g = (11.5 \pm 0.7)$ for this three cases. RIGHT: Corresponding traces in conductance for $B = 65$ mT. $A = -0.2$, $A = 0.01$ and $A = 0.1$ are estimated from top to bottom.

The experiment was repeated for a fixed value of V_{cg} where $A < 0$. In this case, dips instead of peaks appear close to the resonant condition (see Fig. 5.8 b)). This is the expected behavior, as an opposite asymmetry in bias voltage leads to an opposite current flow in the resonance configuration (see Fig.5.9).

From the half-distance $\Delta B(f)$ between the resonant dips, we determine a g-factor of (10.7 ± 0.5), which is again close to the one obtained from Figs.5.7 a) to c).

5.3 Discussion

Clearly, higher asymmetric conductances of the inelastic cotunneling steps should result in more pronounced resonant peaks; to maximize this asymmetry is thus essential. In this experiment, the measured asymmetries were smaller than those found in SiGe QDs (see Chapter 4) and also smaller than those measured by Csonka et al. for InAs NWs [100].

In addition, as already mentioned, further studies are required to investigate the origin of the central peak observed in Figs.5.8 a) and b). This central peak, if due to the nuclear spin polarization, may be strongly suppressed in SiGe QDs due to the lower content of nuclear spins.

Finally, it is important to remark that pump mechanism at play extracts preferentially one spin species (say up) from one of the leads (say right) and it injects the opposite spin species (down) in the other lead (left). As a result, the pump current effectively injects the same spin polarization in both reservoirs.

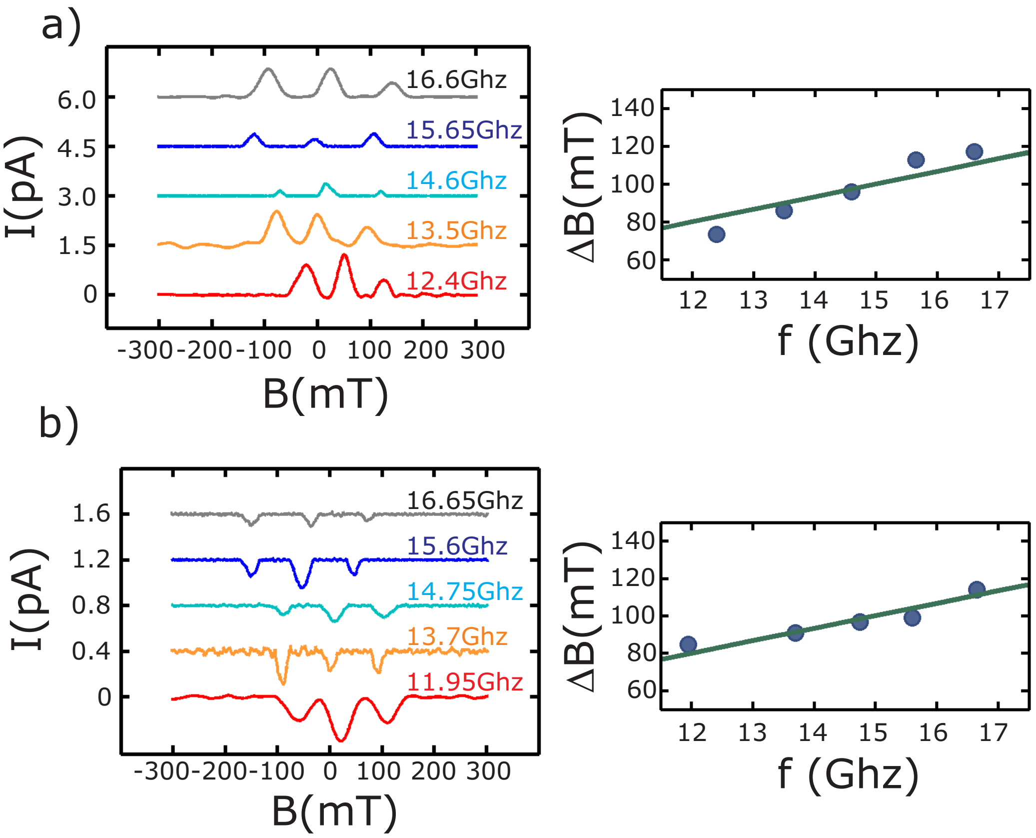

Figure 5.8: LEFT: Averaged I as a function of B for different microwave frequencies. a) $V_{cg} = 549$ mV, $A > 0$; we observe peaks around the resonant value of B for each considered frequency. b)$V_{cg} = 544$ mV, $A < 0$; dips instead of peaks are found around the resonant condition. RIGHT: Half-distance in B between the resonant features, $\Delta B(f)$, as a function of the chosen frequencies. From a linear fit to the relation $\Delta B = \frac{hf}{g\mu_B}$, we extract $g = (10.6 \pm 0.9)$ for $A > 0$ (upper plot), and $g = (10.7 \pm 0.5)$ for $A < 0$ (bottom plot).

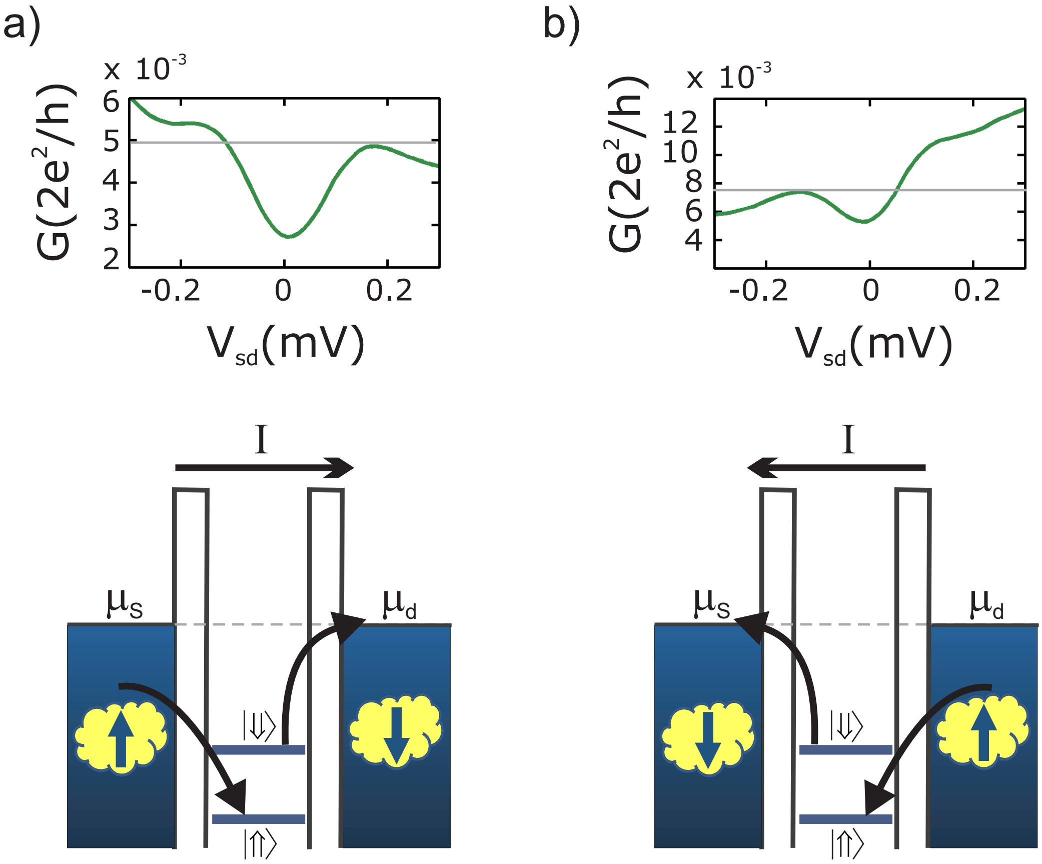

Figure 5.9: Traces displayed in Fig.5.7 with their corresponding scheme for the decay phase (phase shown in Fig.5.1 c)). a) $A > 0$ and thus a negative bias enhances inelastic cotuneling processes, implying that it should be more favourable to tunnel out from the excited state to the right lead. We can then conclude that the right lead is better coupled to the down spin species. b) In this case $A < 0$, so a positive bias is needed to favour inelastic cotuneling processes. In this case, the left lead should be the one that is better coupled to the excited state, and thus it is the one associated with the down spin species.

.

Chapter 6

Coupled SiGe self-assembled quantum dots

Semiconductor quantum dots may be connected to each other in appropriate configurations to implement diverse quantum scenarios, where fundamental charge and spin-related phenomena such as charge sensing, spin-spin coupling between neighboring QDs, quantum entanglement of carriers and transfer of spin information can be addressed.

Self-assembled QDs provide a promising playground for realizing coupled QD devices, as the confinement potential is already given by the nanocrystal structure and only deposition of interconnecting electrodes is needed. In Fig.6.1 different device configurations are shown, which could enable different functionalities and serve to a variety of original experiments. Below, examples of the phenomena that can be explored in each of the structures illustrated in Fig.6.1 are discussed.

1. Two independently contacted QDs next to each other could form a combined qubit-detector system (Fig. 6.1 a)). One QD acts as a spin qubit, while the other QD acts as an electrometer to sense the charge occupation of the QD qubit. Through well-established schemes of spin-to-charge conversion [101], charge information is then used to read-out the spin state of the qubit. The necessary capacitive coupling between the QD qubit and the QD detector could be enhanced by means of a floating gate electrode extending between the two QDs (Fig.6.1 b)).

2. In the most typical double QDs, the coupling between the respective QD states occurs by direct tunneling. In qubit applications, inter-dot tunneling allows for a sizeable exchange interaction between two adjacent qubits, the necessary ingredient for scalable qubit architectures. In the case of SiGe self-assembled QDs direct tunneling between two

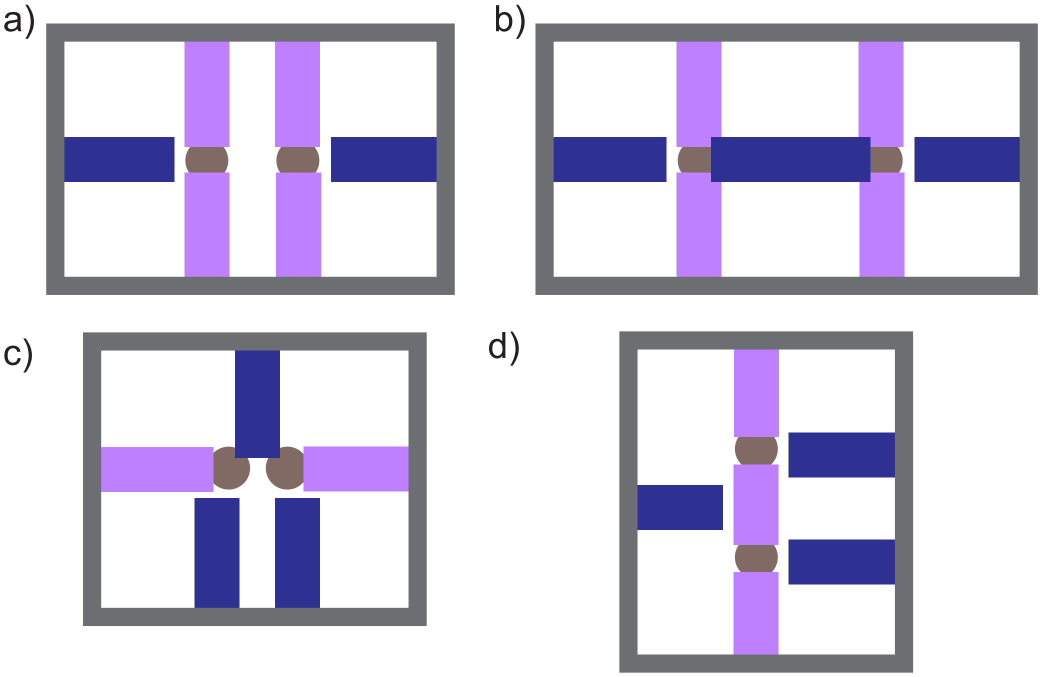

Figure 6.1: Diverse configurations in which self-assembled islands could be coupled. The gate electrodes are represented in blue and the source-drain contacts, in violet. a) Nearby QDs contacted to perform charge sensing experiments. No direct tunneling between the islands is allowed. b) Distant QDs coupled by a floating gate electrode. This configuration would also allow to probe charge sensing mechanisms. Again, no direct tunneling should take place. c) In this configuration, direct tunneling between the QDs would be enabled by a plunger gate. The QDs would then be connected in series and spin-spin coupling mechanisms could be explored. d) Direct tunneling between the islands is, in this case, mediated by a metallic bridge. Spin transfer and entanglement at a distance could be studied in this type of devices.

QDs has not been observed yet, and it is unclear whether it would be possible at all.

Self-assembled QDs are known to be surrounded by a ring-shape depression in the crystal surface whose width is in the order of a few nm. This depression originates from a mechanism of strain release [20]. The presence of this ring structure may prevent the possibility to position two QDs in contact with each other. Yet, a gate positioned between the two QDs could be sufficient to enforce a sizeable tunnel coupling. This type of device is depicted in Fig.6.1 c).

3. Should a suitable tunnel coupling between adjacent QDs be impossible to achieve, another interesting possibility exists for a finite exchange coupling between two spins sitting on different QDs. This possibility relies on the spin-orbit interaction [102].

   The simplest situation where this effect can occur involves two neighbouring QDs, each occupied by a single spin. In this picture, an electric dipole is induced on the QDs as a consequence of the Coulomb interaction between the two charge carriers. The resulting electric dipole moment couples to the spins via the spin-orbit interaction. In this way, an indirect spin-spin coupling between distant electron spins is created. Structures of the type shown in Figs. 6.1 a) and b) would allow us to gain a deeper understanding about this subtle effect based on spin-orbit mediated spin-spin interaction.

4. Replacing a floating gate with a connecting electrode whose edges are tunnel coupled to the respective QDs (see Fig.6.1 d)) could also lead to interesting applications. For instance, the metal bridge could couple the spins of two distant QDs via the so-called RKKY interaction [103]. This effect, while potentially interesting at a fundamental level, would not be particularly useful for spin-qubit applications. A second interesting possibility could emerge from the use of superconducting bridges, especially if made of superconductors with low spin-orbit coupling and hence long spin diffusion length (e.g. aluminium).

   QDs could be operated as spin filters if the splitting of the spin states exceeds the width of the energy levels [104, 105]. In this case, the transport through the dot is, for certain regimes, spin polarized and the polarization of the spin filter can be reversed electrically by tuning the dot to the relevant transition. Then, one spin-polarized QD could be used as ‘emitter’ to send a spin-polarized carrier into the unoccupied quasiparticle band of a BCS superconducting bridge. The quasiparticle is collected by the second spin-polarized QD ('receiver') provided it has the corrected spin polarization. This event is detected as a charge switch measured by an electrometer coupled to the second QD. Because the spin polarization of the QD receiver can be adjusted by its control gate voltage, this experiment would allow testing of the efficiency of this spin polarized transfer as a function of a (in principle) tunable dwell time of the transmitted quasiparticle.

Having described the motivation, the following sections are devoted to the description of my efforts directed to the realization of coupled QD devices based on SiGe self-assembled nanocrystals.

6.1 Directed approach

In order to contact the SiGe nanocrystals, a 'random' approach, described in detail in Chapter 2, was developed by the group. In few words, this approach is based on the deposition of source-drain contacts all over the sample surface followed by the identification of the contacted SiGe islands by SEM imaging.

This technique, although relatively simple, is hardly extendible to multiple-QD devices due to the very little chance to simultaneously 'catch' two QDs within the same device. More complex device configurations require to be able to deposit the source, drain and gate electrodes on a particular island chosen on the sample surface.

Due to the small lateral size (< 100 nm) of the SiGe self-assembled QDs, this *directed* lithography approach requires an alignment accuracy of 10 nm. To face this challenging goal, I took advantage of a 100 kV ebeam writer (JBX 6300FS) able to achieve a realignment precision in the order of our needs. In order to contact preselected SiGe nanocrystals with high accuracy, a strategy based on the characteristics of this ebeam writer was then developed.

The first step of this fabrication process is to define a set of *global* and *local alignment crosses* and a set of *fine alignment markers*, shown in Fig.6.2 a), b) and c), respectively.

In order to obtain the best alignment accuracy, the alignment markers need to be sharply defined. To accomplish this, the alignment markers were defined using the 100 kV ebeam writer, which has a resolution of ~ 8 nm. In addition, the size of the inner write-fields was chosen to be sufficiently small such that the electron beam is able to write in this region with no need of moving the sample stage, i.e. with no need of *stitching* (under this condition the maximal field area for our ebeam writer is 62.5×62.5 μm^2). Therefore, 9 inner write fields with a lateral size of 62.5 μm were defined.

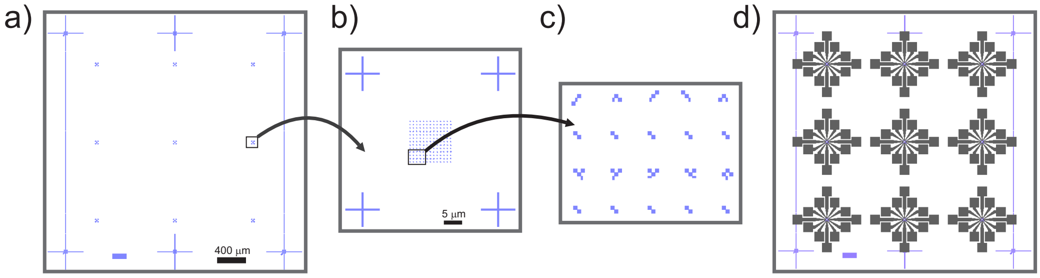

Figure 6.2: a) First step of ebeam lithography. 6 global alignment crosses are defined together with 9 write-field inner areas. The bar on the bottom indicates the orientation of the sample and the lines on the sides simplify the search of the alignment crosses when realigning in successive lithographic steps. b) Close-up of one of the write field inner areas. 4 local alignment crosses are defined at a 40μm distance from each other. c) Fine alignment markers composed of 50×50 nm^2 squares and 25×50 nm^2 and 50×25 nm^2 rectangles. The distance between adjacent markers is 1 μm d) Second step of ebeam lithography in which bonding pads are defined around each inner write field.

Each of these fields contains a set of regularly spaced *fine alignment markers*, which serve as a system of coordinates in the write-field. They are spaced 1μm apart and they are unique in a combination of 4. With these markers we are thus able to identify in the write field area a specific region of $1 \times 1\mu$m^2.

Once the alignment crosses and markers are defined, a second step of ebeam lithography is performed in order to define 9 write fields, each of them with 12 bonding pads (Cr/Au 10/65 nm) of $150 \times 150\mu$m^2 (see Fig.6.2 d)) [1].

SEM images of the write field inner area are afterwards taken. At least 4 fine alignment markers should be visible, as shown in Fig.6.3 a). As already mentioned before, these 4 markers provide a code that enable us to identify the specific write field area to which the image corresponds. This SEM imaging is done at 5 kV. Low resolution images are taken in order to avoid carbon contamination on the nanocrystals surface.

The next step is to select, on the SEM images of a particular write field, those SiGe islands that we would like to contact. Then, in order to design its source and drain electrodes, the SEM images should be imported in a layout

---

[1] This step of ebeam lithography does not require the same resolution than the one that defines the fine alignment markers, and consequently, the resist layer is chosen to be highly sensitive in order to economize on the exposure time of such big areas.

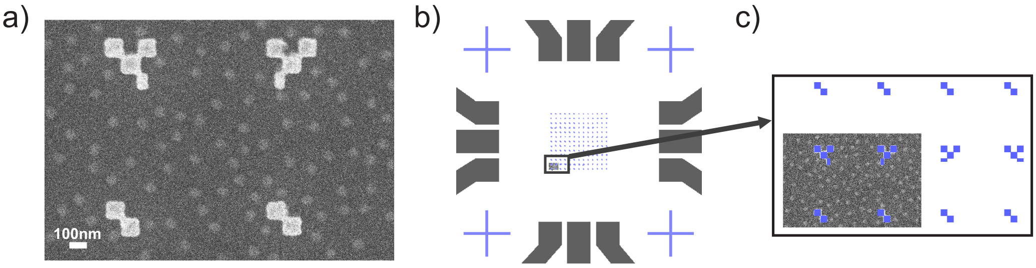

Figure 6.3: a) Low resolution SEM image of a specific area on the sample surface. This area corresponds to a particular write field, inside which it can be accurately placed thanks to the four fine-alignment markers forming a unique combination. b) SEM image loaded in the layout corresponding to a write field inner area. c) Zoom-in on b), the fine-alignment markers on the SEM image should be accurately aligned with respect to the ones in the layout.

editor. The software used for this purpose was *KLayout*, an open-source design platform with image overlay capabilities, i.e. image files (.jpg, .png, .gif) can be loaded and placed at an arbitrary position in a given layout. Fig.6.3 b) shows the layout corresponding to a inner write field area and an imported SEM image. The coordinates, rotation angle and dimensions of this image should be chosen in such a way that the fine-alignment markers on it match those of the layout (see Fig.6.3 c)).

Finally, the source and drain contacts can be drawn on the selected islands, as shown in Fig.6.4 a). As the described approach guaranties that they will be accurately placed on top of the nanocrystal, these contacts can directly reach the write field electrodes (see Fig.6.4 b)), in contrast to the case described in Chapter 2.

Once the design of the source and drain contacts is ready, the ebeam lithography can be performed. The parameters chosen for this delicate lithographic step are those described in Chapter 2, with the difference that the electron beam exposure is carried out by a 100 kV ebeam writer at ~ 1 nA.

Fig.6.4 c) shows the design of the source and drain electrodes for a selected SiGe island and Fig.6.4 d), the outcome of the ebeam lithography after development, etching, metal deposition and lift-off. A satisfactory alignment accuracy (around 10 nm) can be achieved. In Table 6.1 the described process flow is summarized.

For the 'random' approach described in Chapter 2, the source and drain electrodes are designed to be 250nm wide. However, more complex device configurations require narrower electrodes. Therefore, in the described 'di-

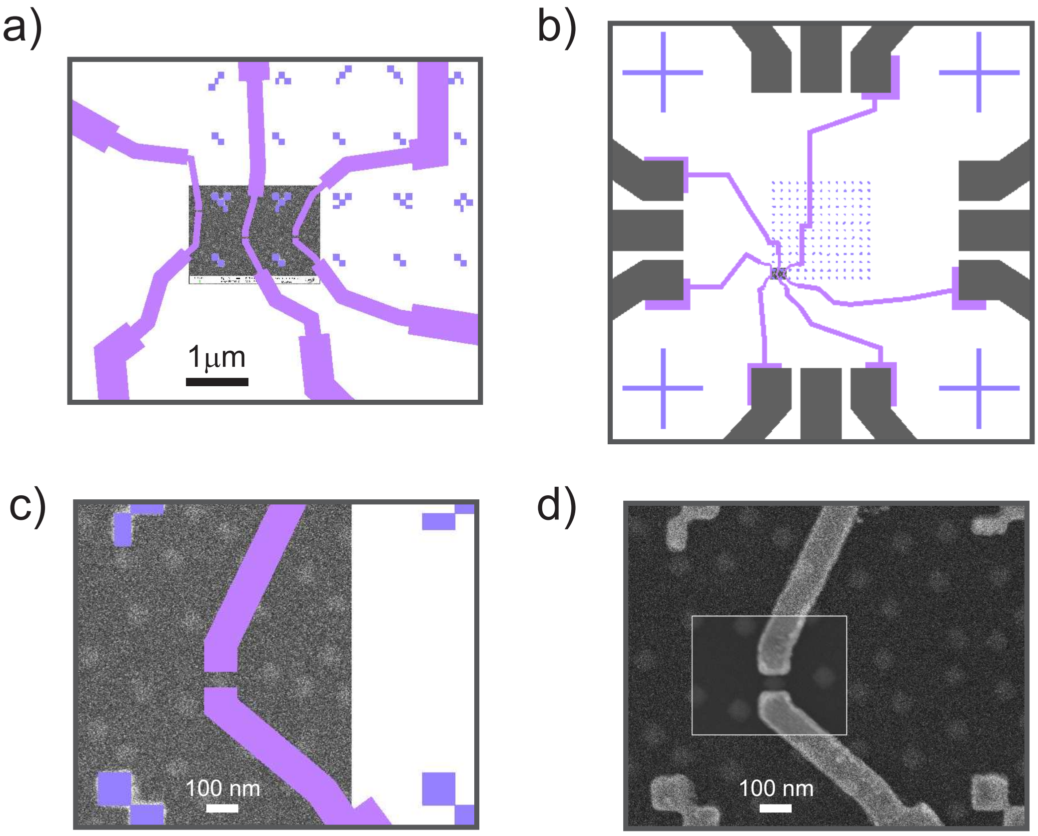

Figure 6.4: a) Design of the source and drain electrodes for selected SiGe nanocrystals on a SEM image aligned to the layout. The electrodes have a 100 nm width, becoming wider as they get further away from the nanocrystal. This widening of the electrodes is intended to make them more robust. b) The source and drain contacts are directly connected to the write field electrodes. c) Design of the source and drain contacts on a SiGe island to be compared with the outcome of the lithographic process shown in d).

Table 6.1: Process flow

1.	Alignment crosses and fine alignment markers	Ti/Au 10/50 nm + lift off	see Figs.6.2 a), b) and c)
2.	Write field electrodes	Ti/Au 10/65 nm + lift off	see Fig.6.2 d)
3.	SEM imaging and pattern design		see Fig. 6.3 and Figs. 6.4 a), b) and c)
4.	Source and drain leads to write field electrodes	Al 30 nm + lift off	see Fig. 6.4 d)

rected approach' the source and drain electrodes are defined to be at most 100 nm wide.

In order to realize the device configurations illustrated in Fig.6.1, narrow gate electrodes should also be defined. In principle, side gates could be defined in the same lithographic step as the source and drain contacts (see Fig.6.5 a)). However, in this case the gates end up showing significant leakage to the source and drain leads; we have noticed that when two metal electrodes are placed less than 2 μm away from each other, a significant conduction can be observed between them at voltage differences of the order of 1 V. This conduction occurs via the silicon substrate. On the other hand, it is important to remark that leakage between the source and drain contacts is not a problem since low bias voltages are usually applied. We have also verified that gates cannot be placed more than a few nanometers away from the QD contacts, as the coupling to the island becomes too weak and no gating effect is observed.

For the fabrication of these narrow gate electrodes, an approach identical to the one described in Chapter 3 section 3.4 was then explored. This approach, based on the deposition of 6 nm of hafnia by ALD followed by a 10/90 nm layer of Ti/Pt, leads to very bad results when it comes to lift-off of narrow patterns and small gaps. We have noticed that the deposition of a thinner layer of Ti/Pt (0.5/10 nm) improves the lift-off results (see Fig.6.5 b)), although it is not always successful and the metal layer is often peeled

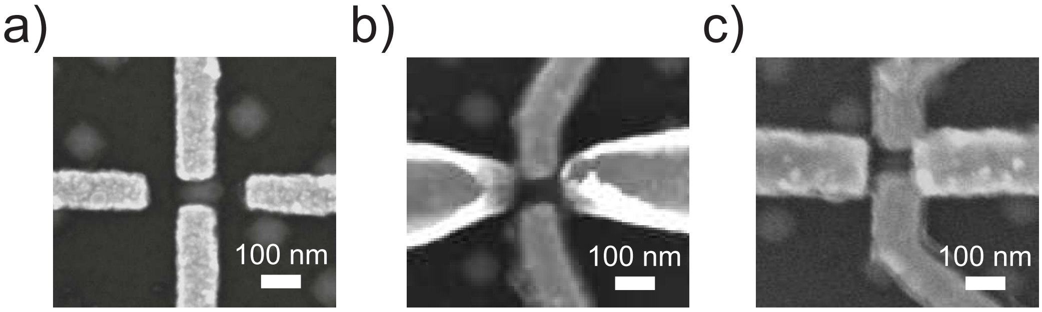

Figure 6.5: Narrow gate electrodes (∼ 100 nm) on each side of a contacted SiGe nanocrystal. a) The gates were deposited directly on top the silicon surface; they have been defined in the same lithographic step as the source and drain contacts. b) The gate electrodes were fabricated by ALD deposition of 6 nm of hafnia followed by a 0.5/10 nm layer of Ti/Pt. As this metal strip lies on top of a dielectric, the gates can overlap the source and drain contacts in order to increase the coupling to the nanocrystal. c) 4 thin layers of aluminium are oxidized, each at a time, to form an aluminium oxide layer that is covered by a 0.5/40 nm Ti/Au metal layer.

off from the areas where it should stick and sticks in areas where it should not.

We have then tested another approach in which gate dielectric and metal are defined in the same lithographic step. After ebeam lithography and resist development, the sample is loaded into the evaporator. Four 1.5-nm-thick aluminium layers are deposited and immediately oxidized in-situ using an oxygen pressure of 200 Torr for 10 min. These superimposed layers of aluminium oxide form a dielectric that is finally covered by a 0.5/40 nm Ti/Au layer. An easy lift-off is guaranteed by the non-conformal deposition of the dielectric and Ti/Au secures a proper adhesion of the metal strip (see Fig.6.5 c)).

It is possible to avoid the extra step of ebeam lithography required to link the defined gate electrodes to the bonding pads. To this aim, the gate electrodes are defined already with their own bonding pads as shown in Fig.6.6.

Finally, Fig.6.7 shows how the device configurations depicted in Fig.6.1 were realized within this ‘directed’ approach. Figs.6.8 a) and b) exhibit SEM images of some of these devices taken at an angle. Fig.6.9 offers further examples showing the potential of this nanofabrication approach for realizing a variety of device configurations.

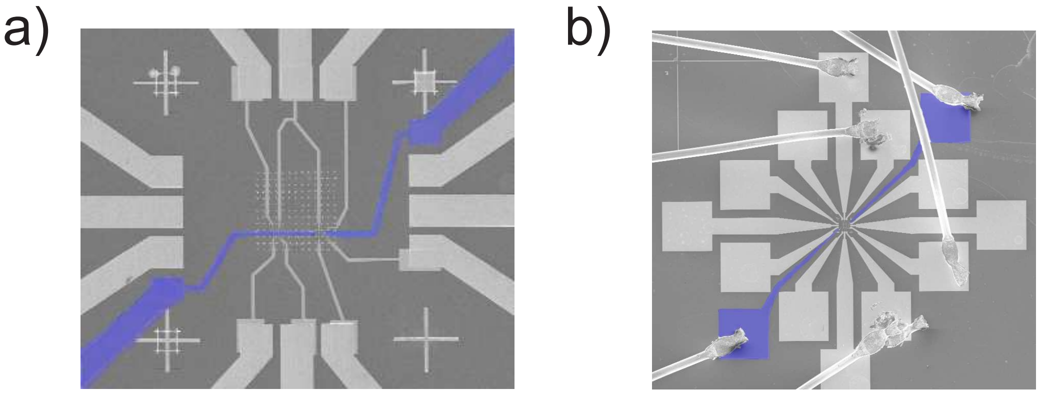

Figure 6.6: a) SEM image of an inner write-field area where narrow gate electrodes widen up to their bonding pads. These electrodes have been artificially colored. b) Zoom-out on a) showing those extra bond pads that correspond to the gate electrodes.

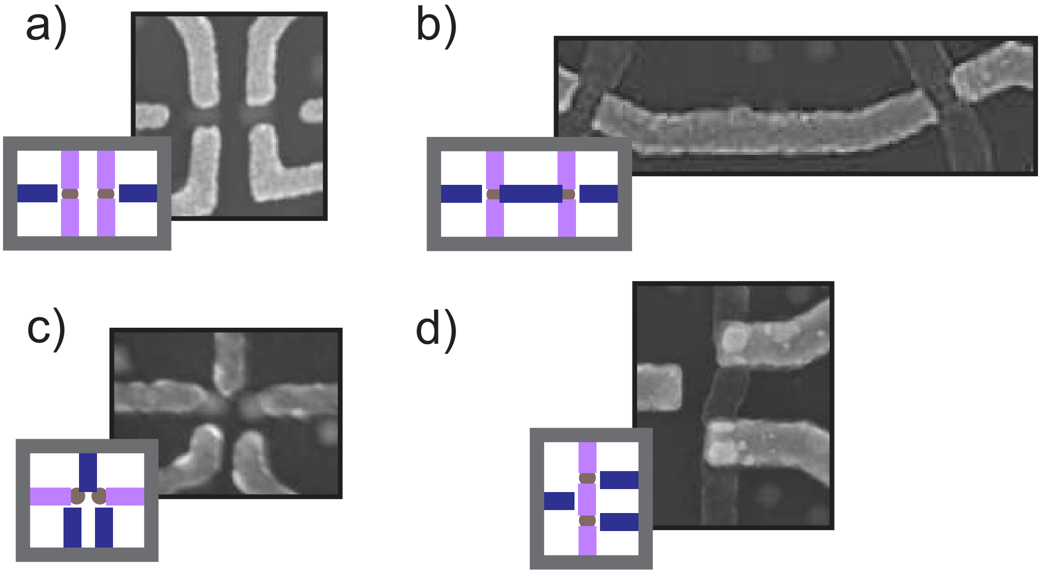

Figure 6.7: a)-d) Envisaged configurations shown in Fig.6.1 a)-d), and the correspondent SEM images of the actual realization of these devices. The scale of the SEM images is given by the dot diameter, which corresponds to 80 nm. In a) and c) the gate electrodes have been deposited directly on the sample surface, while in b) and d) they are formed by an aluminium oxide layer covered by a Ti/Au metal layer. The gate electrodes corresponding to the SiGe islands in d) are directly placed on top of the nanocrystals.

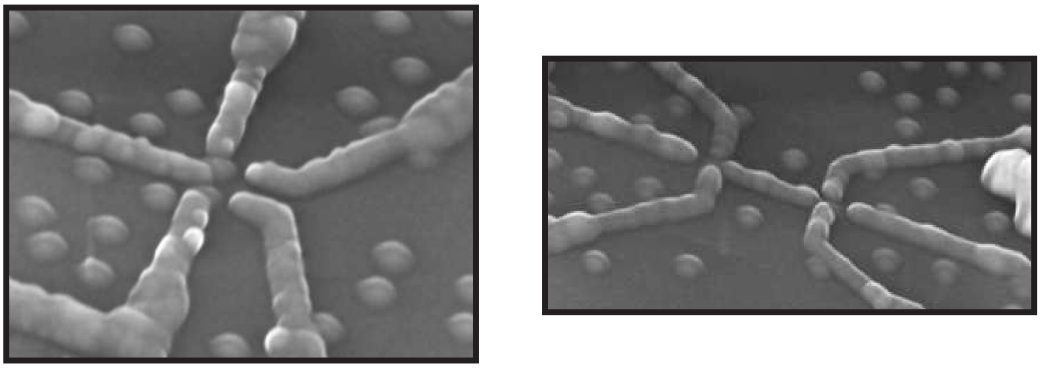

Figure 6.8: SEM images taken at an angle of two of the coupled device configurations that were achieved. The scale of the SEM images is given by the dot diameter, which corresponds to 80 nm.

Difficulties and remedies

Although the ‘directed’ approach was successfully implemented, the contact resistances of the source and drain leads to the SiGe islands were found to be extremely high and the yield of working devices very poor when compared to devices fabricated within the ‘random’ approach. The new fabrication procedure turned out to embed subtle differences sufficient to compromise the contact properties. In order to unveil the cause of the exceedingly high contact resistances, several tests were performed.

In Table 6.2 we have displayed a comparison between the fabrication steps of the ‘directed’ and the ‘random’ approach leaving aside the fabrication of gate electrodes. The steps that could affect the contact resistances are those that define the properties of the contact area between the metal leads and the nanocrystal, i.e. those steps that take place before the definition of the contacts (1^{st} step), or those that have to do with the ebeam exposure and subsequent treatments before metal deposition (2^{nd} and 3^{rd} step).

In order to study the impact of the 1^{st} step in the contact resistances of the devices, we have fabricated samples for which the 1^{st} step of the fabrication process was performed as for the ‘random’ approach (the contact width was designed to be 250 nm and no imaging was performed before the deposition of the leads). The contact resistances did not show any improvement, implying that the 1^{st} step is not responsible for the deterioration of the contact resistances. Given the fact that the 3^{rd} step is shared by the two approaches, the differences in the 2^{nd} step appear then as main suspects.

Unfortunately, in order to achieve the realignment precision needed to

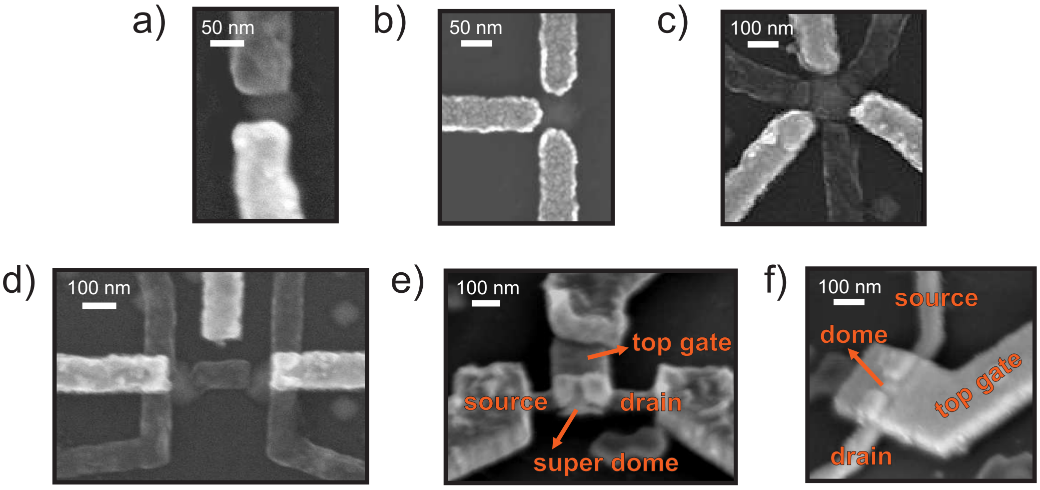

Figure 6.9: a) Source and drain contacts made of different metals, being Pt and Al for this SEM image. This device would allow us to explore the transport properties resultant of an island coupled to one superconducting and one normal lead. The possibility of combining semiconducting nanostructures with different metallic leads of normal, ferromagnetic, or superconducting type, creates a great wealth of new physical scenarios. b) Three terminal device; interference of scattered electrons could be explored in a weakly coupled regime. c) Three terminals on a super dome island with three gate electrodes (brighter). Different confinement potentials can be generated in this way. d) Coupled super dome islands. Gate electrodes appear brighter. e),f) Devices on a silicon on insulator substrate in which the Si upper layer has been etched away in order to suppress parallel conductive paths. In this way, room temperature transistors could be build.

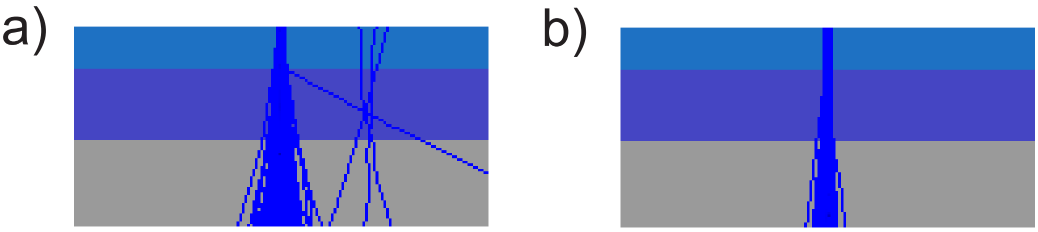

Figure 6.10: Monte Carlo simulations of the electron trajectories on a silicon substrate coated with a bilayer of PMMA resist are shown (a software called *CASINO*, developed in *Univeristé de Sherbrooke, Canada*, was used for this purpose.). The scale of the images is 500 nm in width and 250 nm in high. The electron beam energy is 20 kV in a) and 100 kV in b). In a) some back-reflected trajectories are observed.

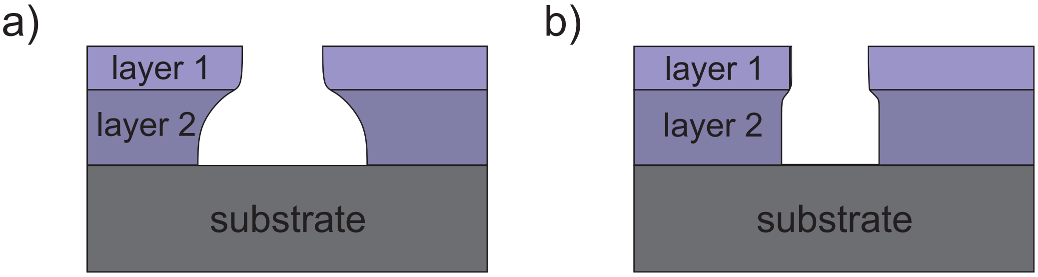

Figure 6.11: Illustration of different profiles of a bilayer resist after exposure and development. The two cases correspond to different acceleration voltages, case a) corresponding to lower acceleration voltage than case b).

contact selected self-assembled islands, the 100 kV ebeam writer should replace the 20 kV modified SEM employed within the 'random' approach. Consequently, we have to deal with the properties of the 100KV electron beam and revise other factors related to the lithographic step in which source and drain leads are defined.

Fig.6.10 a) and b) shows how the penetration of the electron beam varies for acceleration voltages of 20 kV and 100 kV, respectively. The resist profiles after development, illustrated in Figs.6.11 a) and b), are thus very different in these two cases. Fig.6.12 a) shows a SEM image of source and drain leads defined by a 100 kV electron beam on a bilayer resist; after development and before metal deposition, a very small undercut of about 10 nm can be distinguished.

Table 6.2: ‘Directed’ and ‘random’ fabrication steps comparison

	‘Random’ approach	‘Directed’ approach
Chip preparation	Definition of alignment crosses, linking pads and bonding pads	Definition of alignment crosses, fine alignment markers and bonding pads
1^{st} step, conditions	lead width: ∼ **250nm**	SEM Imaging and pattern design 5 kV lead width: ∼ **100nm**
2^{nd} step, conditions	Definition of source and drain leads ebeam: **20kV**, **15pA** resist: bilayer PMMA 2% 950K / PMMA 4% 200K	Definition of source and drain leads ebeam: **100kV**, **1nA** resist: bilayer PMMA 2% 950K / PMMA 4% 200K
3^{rd} step, conditions	Development and etching 30 s MIBK:IPA $1:3+1$ min IPA 10 s BHF + rinse in water	Development and etching 30 s MIBK:IPA $1:3+1$ min IPA 10 s BHF + rinse in water
4^{th} step	Metal evaporation and lift-off	Metal evaporation and lift-off
5^{th} step, conditions	SEM Imaging 5 kV	
6^{th} step	Definition of the connections to the write field electrodes	
7^{th} step	Bonding and cool-down	Bonding and cool-down

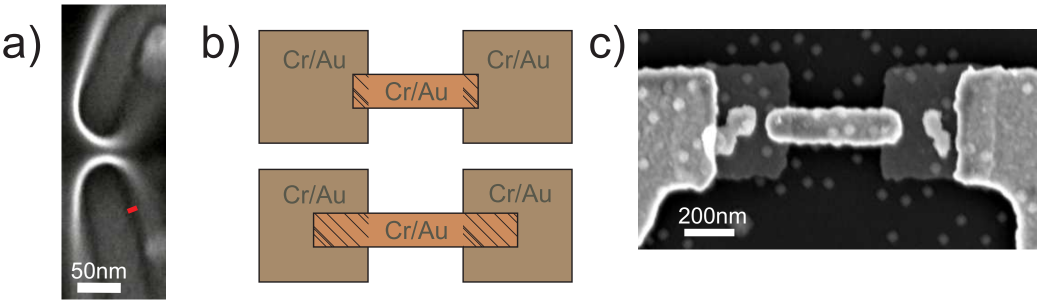

Figure 6.12: a) SEM image of a pattern exposed at 100 kV on a bilayer resist and developed under the conditions described in Table 6.2. No metal deposition was performed in order that a difference in contrast allows us to distinguish the resist undercut in the SEM image. The undercut, of about 10 nm, is indicated by a red trace at one of the sides of the pattern. b) Illustration of the metal surfaces with different contact areas (striped areas) designed to determine if resist residues could be responsible for the high resistances observed in those devices fabricated within the 'directed' approach. c) SEM image of the couples of metal pads of 2/8 nm Cr/Au connected between each other and to the write field electrodes by 10/80 nm Cr/Au strips defined in a later lithographic step.

The distinct resist profile that results from the 100 kV ebeam exposure could be then on the origin of the increased contact resistance between the metal leads and the nanocrystals, for instance due to the presence of resist residues at the edge of the patterned features. We have then fabricated some test samples to verify if PMMA residues were indeed present after development. For these samples, 2/8 nm Cr/Au pads were first defined in the inner write field area. Then, another lithographic step was performed in order to connect pairs of these pads by a narrow metal strip of different lengths and thus with a varying contact surface (see Fig.6.12 b)). At the same time, these pads were also connected to the write field electrodes, as shown in Fig.6.12 c). By applying a few mV to this conduction path, we have found out that when the contact surface of the metallic strips with the connected pads was small (in the order of $0.01\mu m^2$), no current was measured. Just for contact surfaces in the order of $0.04\mu m^2$ the expected short-circuit was observed.

The increased contact resistances of those devices fabricated within the 'directed' approach was then attributed to the presence of resist residues in the contact surface between the metal leads and the semiconductor island. Resist residues in the form of granular structures up to 10 nm thick, and background layers of approximately 3 nm have been reported in [106] for patterns defined with a 100 kV ebeam writer and similar development conditions. Fig.6.13 shows AFM images of the resist residues remaining after development for different exposure doses. In common with other studies, resist granules were observed at low doses, gradually decreasing in size and frequency as the dose increases. However, these granules clearly lie on a raised pedestal of the resist residue which remains even up to very high doses [106, 107]. From the AFM data shown in Fig.6.13, the thickness of this pedestal is around 2.5 nm.

Diverse recipes for an improved development of ebeam exposed patterns on PMMA are discussed in the literature [108, 109, 110, 111, 112]. We have increased the dose used for exposure from 1150 to $1725\mu C/cm^2$ in order to avoid the formation of resist granules and an ultrasonically-assisted development, considered in most of the latter works, has been tried out by modifying the 3^rd step conditions of the 'directed' approach as follows:

20 s MIBK:IPA 1 : 3 + 10 s MIBK:IPA 1 : 3 in an ultrasonic bath + 1 min IPA
10 s BHF + rinse in water

These modified conditions did not help to improve the contact resistances of the SiGe devices in a reproducible way.

In order to remove the remaining resist layer that obstructed the contacts

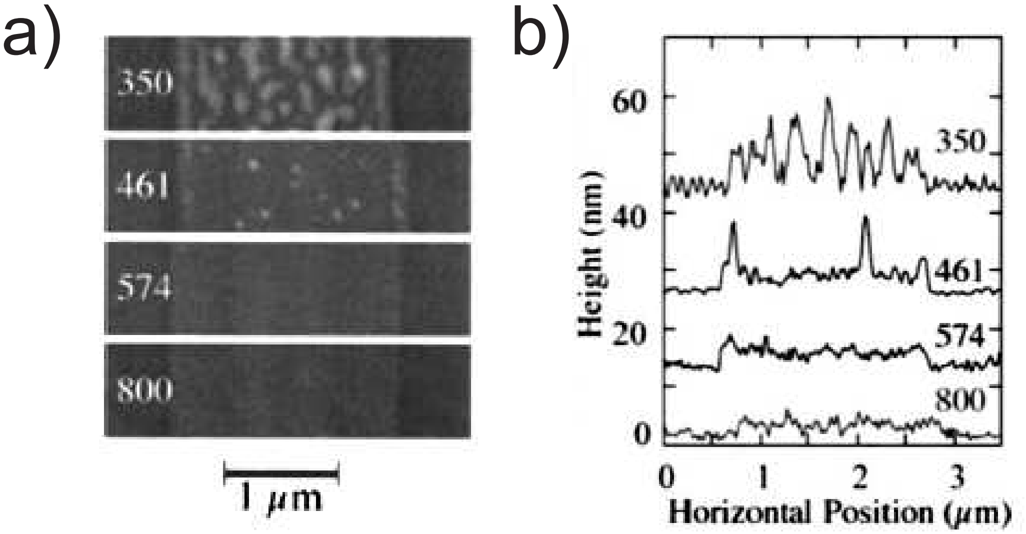

Figure 6.13: Taken from [106]. a) AFM micrographs for doses of 350, 461, 574, and $800\mu C/cm^2$. The doses are shown in each case. The micrographs show resist residues in the exposed regions after development alongside areas of bare silicon. b) AFM cross sections for each of the cases exposed in a). The granular structures are up to 10 nm thick, and an approximately 3 nm background layer is also apparent in the exposed regions.

to the semiconductor islands, we have then opted to add an extra etching step before the BHF dip. The removal of organic matter, such as PMMA, can be achieved by an *oxygen plasma* cleaning. The oxygen species created in the plasma react with organic contaminants, the products being carbon oxides and water vapor which are volatile and pumped away by the vacuum system. The 3^rd step conditions of the 'directed' approach was then:

30 s MIBK:IPA $1:3+1$ min IPA
Oxygen plasma: P : 40 mTorr, cp : 100 W, pp : 0 W, f : 10 sccm and t : 10 s
10 s BHF + rinse in water

being P the pressure inside the chamber, cp the coil power (applied to generate the plasma), pp the platen power or bias (power applied to a metal plate that determines the ion bombardment energy), f the gas flow and t the exposure time. The latter parameters were chosen in order to achieve a very mild etching that would remove just a few nm of the resist profile.

The devices fabricated within these conditions, showed a great improvement of the contact resistances (see Fig.6.14), which were comparable to those achieved within the 'random' approach. However, current switches in the current-voltage characteristic were frequently observed, even for devices in which no gate electrodes were defined. A representative example is shown in Fig.6.14. At constant bias voltage, such switches appear as *random telegraph noise.* This telegraph noise may affect the device properties and it has usually been attributed to defects [113, 114, 115].

Lattice defects in Si substrates have indeed been observed as a consequence of oxygen plasma treatments [116]. We have then explore an alternative procedure in order to etch PMMA residues. An ion gun integrated to the metal evaporator allowed us to replace the oxygen plasma etching by an argon milling. In simple terms the *ion beam milling* can be viewed as an atomic sand blaster; ion particles are accelerated and bombard the surface of the target while it is inside the vacuum chamber. Again, the parameters were chosen in such a way that a very mild etching that would remove just a few nm of resist was achieved. The 3^{rd} step conditions of the 'directed' approach was then modified as follows,

30 s MIBK:IPA $1:3+1$ min IPA
Argon milling: pp : 250 V and t : 10 s
10 s BHF + rinse in water

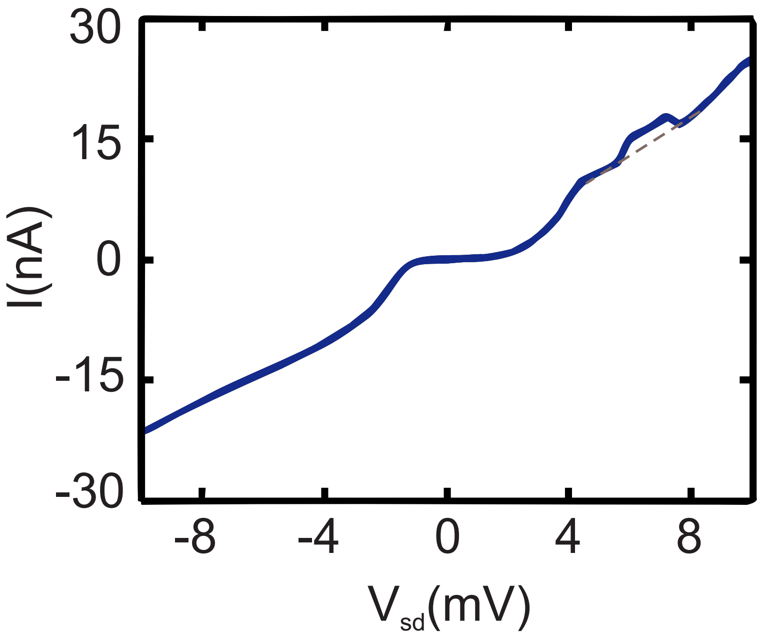

Figure 6.14: Current as a function of the source and drain bias applied to a device at 250 mK with aluminium leads defined within the 'directed' approach. To the latter, an extra step of oxygen plasma etching step was added prior to the BHF dip. For high bias voltages, a resistance of about 300 KΩ was estimated for this device. For $V_{sd} \sim 6$ mV, telegraph noise is observed.

The argon bombardment is performed perpendicular to the sample surface in order to ensure the etching of the PMMA residues in every edge of the resist pattern. The devices fabricated within these conditions had similar contact resistances to those fabricated within the 'random' approach and no switching events were observed in the absence of gate electrodes. Fig.6.15 shows a stability diagram for one of these devices at 4 K.

6.2 First transport measurements on double-dot devices

Once the difficulties of the 'directed' approach had been overcome, some of the coupled device configurations discussed in the introduction to this chapter were tested. However, just a few experiments were performed due to the emergence of difficulties on the growth of the SiGe islands.

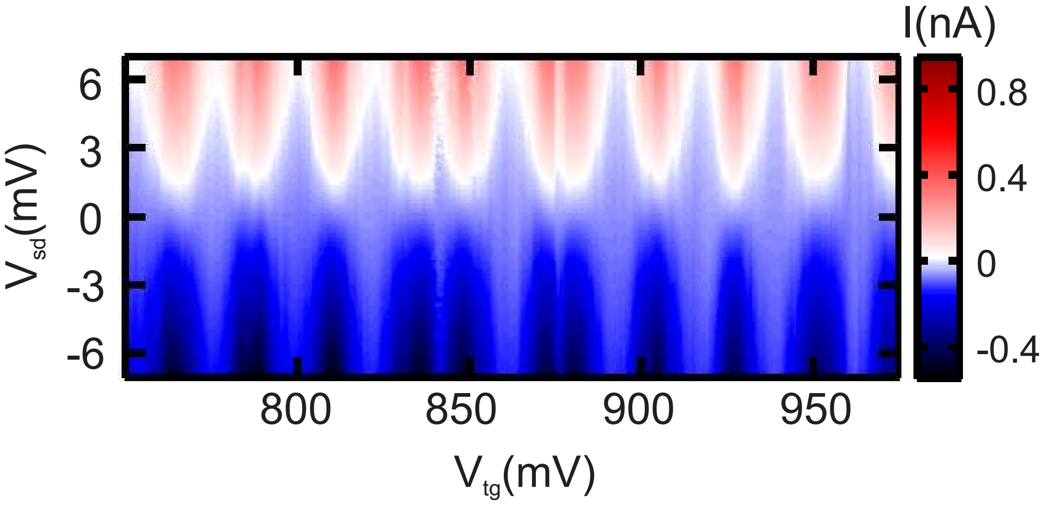

Figure 6.15: Stability diagram of a device at 4 K with aluminium leads defined within the ‘directed’ approach. To the latter, an extra argon bombardment step was added prior to the BHF dip.

Transport mediated by a metallic bridge

A device similar to the one shown in Fig.6.7 d) was fabricated and measured at 250 mK. The source/drain leads and the metal bridge were defined in the same step. A 30-nm-thick aluminium layer was used as contact metal. In a following step, three gate electrodes were defined as in Fig.6.5 c); 4 thin layers of aluminium were oxidized to form an aluminium oxide layer that was covered by a 0.5/40 nm Ti/Au metal layer. Unfortunately, the central gate facing the metal bridge was eventually broken and could not be used. The other two gates, on the other hand, worked properly. Gate voltages V_a and V_b were applied to control the electrostatic potential of QDs a and b, respectively (see Fig.6.16).

The current flow through the device as a function of V_a and V_b is shown in Fig.6.17 for $V_{sd} = 5$ mV. Given the fact that transport is activated just if at least one energy level of each QD is present in the bias window and if the energy level of QD a is above the one of QD b, there are just some combinations of V_a and V_b that allow for transport, as observed in Fig.6.17.

In this large range of gate voltages a sequence of almost horizontal current stripes can be noticed. This behaviour indicates that QD b is the dominant element in the series. The observed stripes correspond essentially to the Coulomb resonances of QD b, which is strongly sensitive to V_b, and weakly sensitive to V_a. To further support this first-level analysis, we show

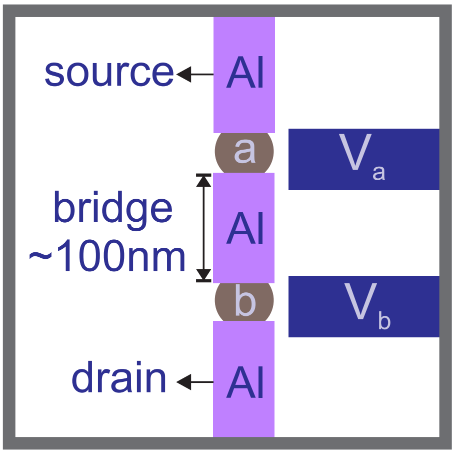

Figure 6.16: Scheme of the coupled-QD device. Two SiGe islands, a and b, are connected through an aluminium bridge.

in Fig.6.18 a) a plot of the source-drain current as a function of (V_b, V_{sd}) for a fixed $V_a = 500$ mV. This measurement, which follows the vertical line in Fig.6.17, resembles the stability diagram of a single QD device, namely QD b. A $I(V_{sd})$ trace for $V_a = 500$ mV and $V_b = 91$ mV is shown in Fig.6.18 b).

To a closer look, however, we can notice a bias window in which tunneling is suppressed. In the absence of an applied magnetic field (Fig.6.18 a)), the aluminium electrodes are superconducting and thus it is expected that tunneling is forbidden in an energy range determined by the gap in the density of states of the superconductors, Δ. Since both the source/drain leads and the bridge are made of superconducting aluminium, the minimal voltage for the onset of quasiparticle conduction would be 4Δ (see Fig.6.19).

This conduction gap should be washed out by applying a magnetic field larger than the critical field. In Fig.6.18 c) we show a similar stability diagram taken for a perpendicular field $B_z = 0.5$, i.e. well above the perpendicular critical field of the aluminium electrodes (a few tens of mT, as shown in Fig.2.13 a) of Chapter 2 section 2.5). By comparing panels a) and c), a clear, yet partial reduction of the conduction gap can be noticed. To analyze this effect more quantitatively, let's focus on the Coulomb diamond edges highlighted by dotted lines. At $B_z = 0$ T, the conduction gap extends from $-E_g$ to E_g, with $Eg \approx 2.2$ mV. At $B_z = 0.5$ T, the conduction gap is suppressed by approximately 0.9 mV, leading to $E_g \approx 1.3$ mV. Assuming this suppression to be equal to $4\Delta/e$, implies $\Delta \approx 0.22$ meV, which is compatible with typical values for aluminium films of 30-nm thickness [117].

The presence of a residual conduction gap at $B_z = 0.5$ T can be regarded

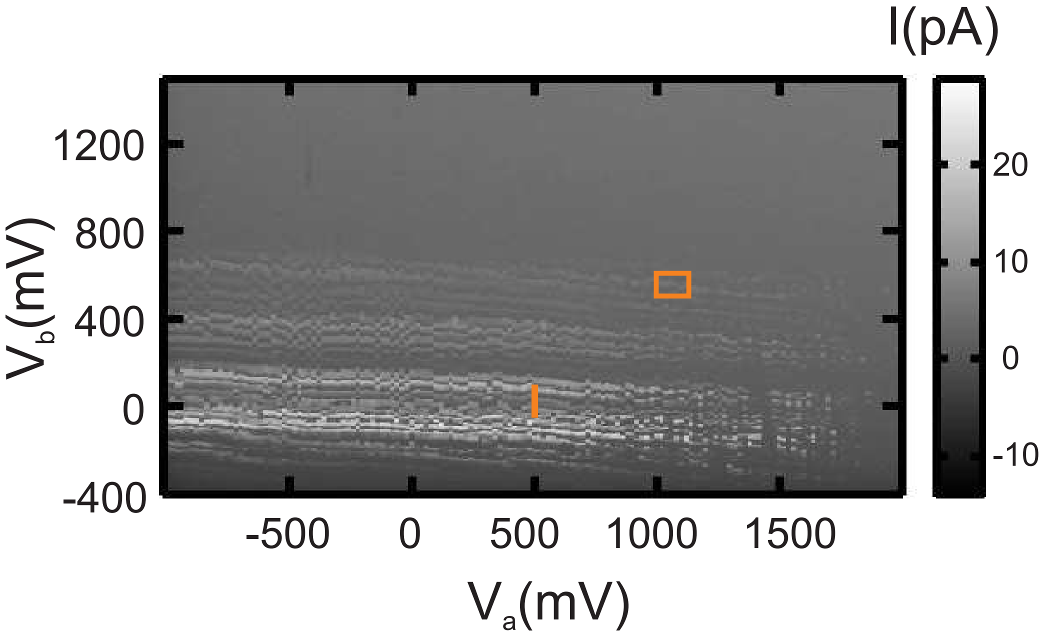

Figure 6.17: Current through the device as a function of V_a and V_b for $V_{sd} = 5$ mV in absence of an applied magnetic field. A vertical line indicates the gate parameter range considered in Fig.6.18 a). A rectangle shows the zoomed-in area presented in Fig.6.20 a).

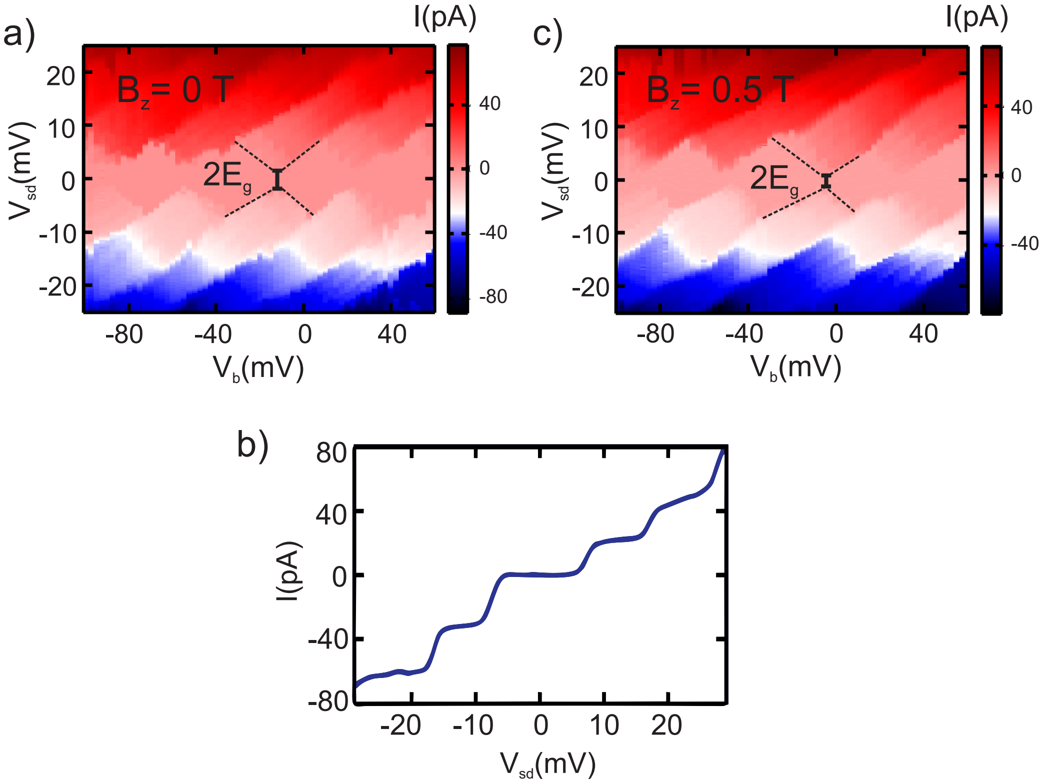

Figure 6.18: a) Current as a function of V_{sd} and V_b for $V_a = 500$ mV (vertical line shown in Fig.6.17). The diamonds do not appear to close; a bias window where transport is suppress can be observed. The width of one of these gaps is indicated as $2E_g$, being $E_g \sim 2.2$ mV. b) Current as a function of V_{sd} for $V_a = 500$ mV and $V_b = 91$ mV, fixed. c) Idem to a) under a perpendicular magnetic field $B_z = 0.5$ T. E_g appears reduced with respect to the measurement shown in a); $E_g \sim 1.3$ mV in this case.

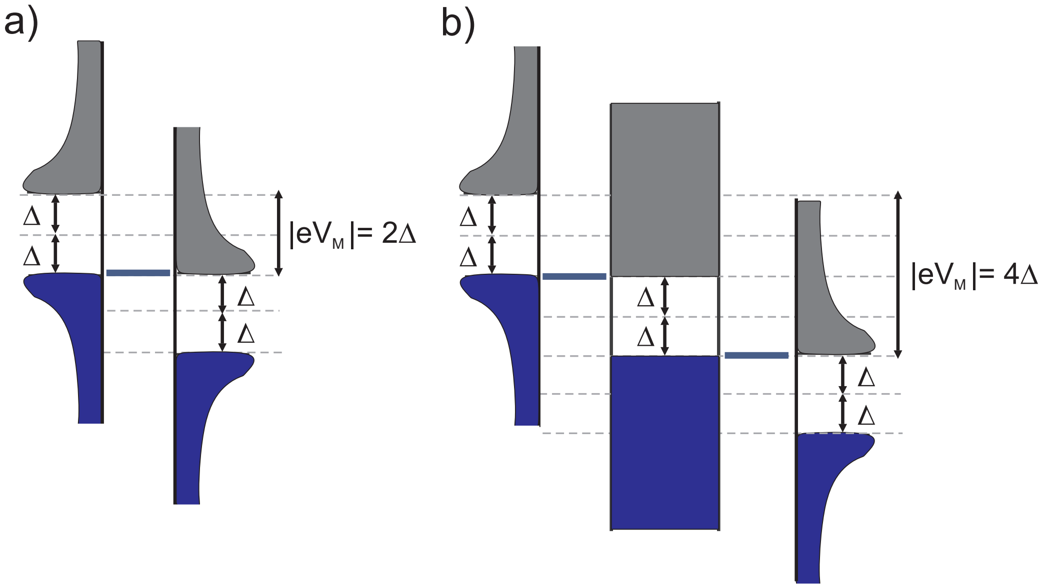

Figure 6.19: a) Qualitative electronic density of states (horizontal axis) versus energy (vertical axis) for a QD between superconducting leads. In the leads, an energy gap Δ separates the Fermi energy from occupied (blue) and unoccupied (gray) single-particle states. The minimal voltage for the onset of quasiparticle conduction, V_M, is 2Δ. b) Idem to a) in the case of the device under study (two QDs between superconducting leads connected through a superconducting bridge). V_M is expected to be 4Δ in this case.

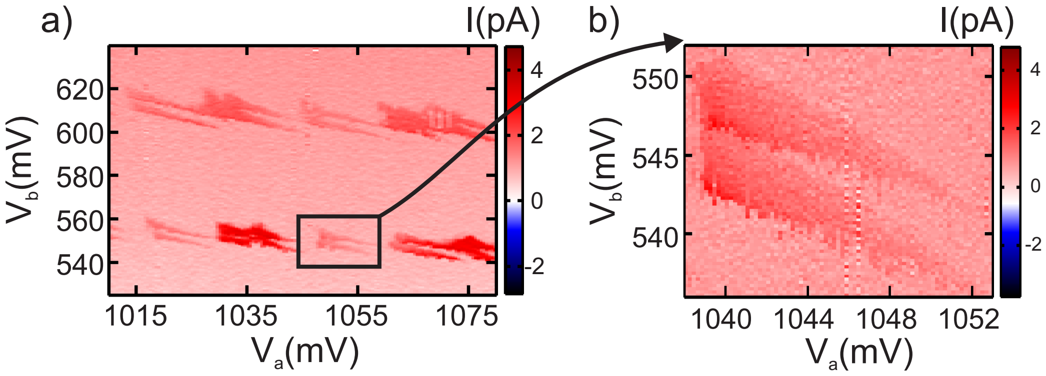

Figure 6.20: a) Region in the (V_a,V_b) plane indicated with a rectangle in Fig.6.17. Current through the device was measured for $B_z = 0$ T and $V_{sd} = 2.5$ mV. b) Zoom-in on the pair of triangles highlighted in a).

as a typical signature of Coulomb-blockaded transport through multiple dots in series; when the bias is small and just one gate electrodes is tuned, the energy levels of each QD are typically not aligned within this small window and thus no transport takes place.

In order to gain further insight on this multi-dot transport regime, a higher resolution measurement of $I(V_a, V_b)$ was taken in correspondence of the region highlighted by a rectangle in Fig.6.17 (see Fig.6.20 a)). This measurement was taken for $B_z = 0$ and $V_{sd} = 2.5$ mV, i.e. a lower bias voltage than the one applied in the measurement shown in Fig.6.17. Interestingly, the stripes in Fig.6.17 appear to be constituted by partially overlapping triangular structures. These types of structures are typically observed in double-QD devices.

For a double-dot configuration, a measurement of the current as a function of the voltages applied to two control gates results in tiny peaks positioned on the vertices, the so-called *triple points*, of a *honeycomb* pattern (see Fig.6.21). The tiny peaks at the triple points transform into triangles (often called *bias triangles*) when the bias voltage is increased, as illustrated in Fig.6.22 [2, 118].

It is expected that the bias triangles change orientation when the bias voltage is reversed (changing the sign of V_{sd}, corresponds to interchanging the roles of the two QDs and, therefore, interchanging the two gate-voltage axes, i.e. $V_{g1} \rightarrow V_{g2}$ and $V_{g2} \rightarrow V_{g1}$). This behaviour is indeed observed in our measurements as shown in Fig.6.23.

Noteworthy, groups of four overlapping triangles are quite often observed (see Fig.6.20 a) and Fig.6.23). We speculate that the appearance of such structures may be a signature of a triple-dot geometry [119, 120, 121, 122],

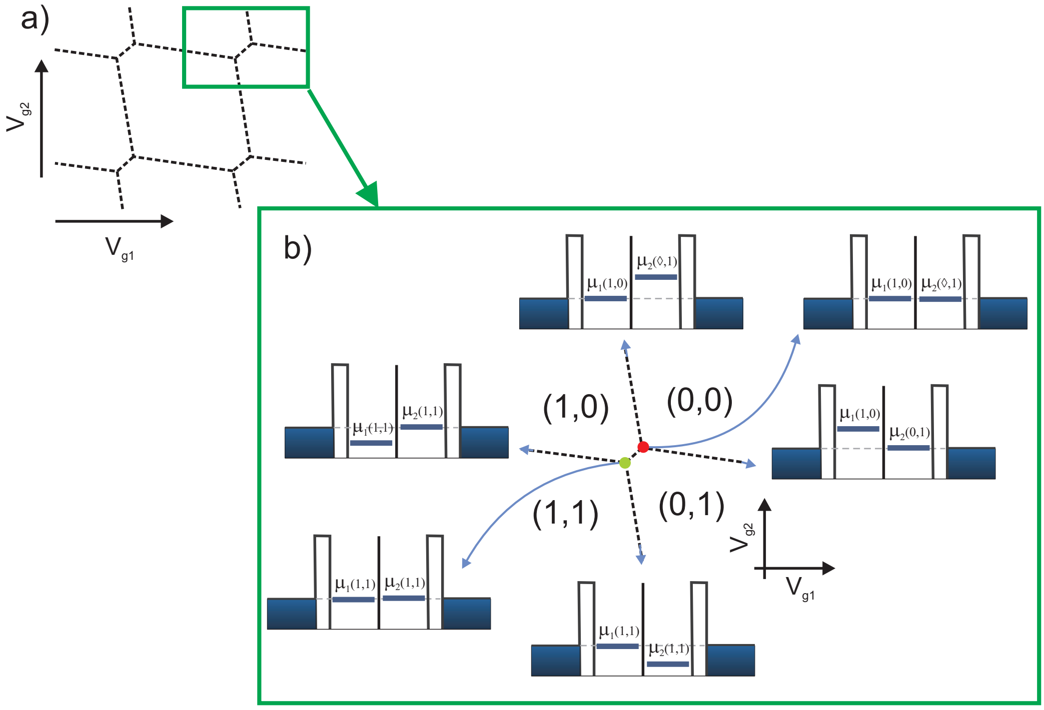

Figure 6.21: a) Honeycomb diagram of a double dot device at zero bias, V_{g1} and V_{g2} being the voltages applied to the gate electrodes of each QD. b) Zoom-in on a). Four different charge states can be distinguished, separated by dashed lines. At the dashed line connecting the two triple points (red and green circles), the charge states corresponding to have one charge in one QD and zero charges in the other $((0,1)$ and $(1,0))$ are degenerate. At the other dashed lines the electrochemical potential of at least one QD is zero and thus equals the electrochemical potential of the leads. The triple points lie on the crossing points between the dashed lines, where current flow through the device. The two kinds of triple points correspond to the electron transfer process (red circle) and the hole transfer process (green circle). The schematic diagrams show the configuration of the ground-state electrochemical potentials for each area of the honeycomb diagram.

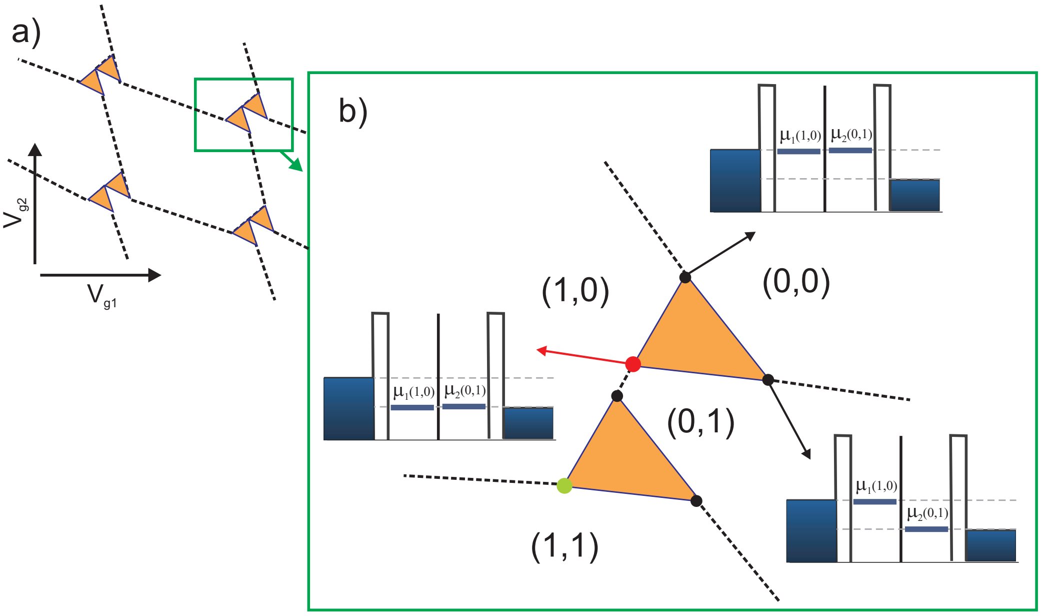

Figure 6.22: a) Honeycomb diagram of a double dot device at finite bias, V_{g1} and V_{g2} being the voltages applied to the gate electrodes of each QD. b) Zoom-in on a). The solid lines separate the different charge states. Classically, the regions of the stability diagram where current flows are given by the orange triangles. In the case of one discrete level per QD, as in the schematic pictures, resonant tunneling is only possible along the side of the triangle that coincides with the line connecting the original triple points (red and green circles). However, even in this case inelastic tunneling and cotunneling still contribute to a finite current within the triangles.

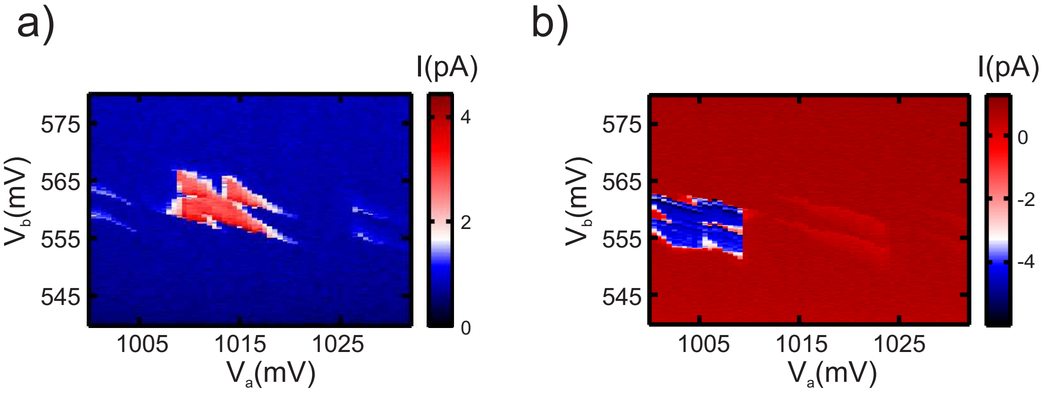

Figure 6.23: Zoom-in on a region of the stability diagram of the device under study. $V_{sd} = 2$ mV for a) and $V_{sd} = -2$ mV for b). When the bias is inverted, carriers move through the device in the opposite direction and thus the triangular features appear inverted and mirrored [2].

where the aluminium bridge plays the role of central QD. While this aluminium island can give rise to a sizeable Coulomb blockade effect, its metallic nature implies a continuum of energy states, so that one cannot speak of a 'true' QD.

To conclude, this work shows for the first time the possibility to establish an electrical connection between two SiGe self-assembled QDs a few hundred nm apart. In a later stage, this connection could be used for experiments aiming at the transfer of spin information between distant QDs. As already mentioned, aluminium is a promising candidate for this goal given its large spin diffusion length [2].

---

[2] The spin diffusion length of aluminium has been estimated to be 450 μm at $T = 4.3$k [123].

Conclusion

In addition to potential device applications, semiconductor quantum dots provide a versatile playground for investigating a variety of quantum phenomena. In this PhD thesis, we have presented electronic transport measurements and models that provide fresh insights into the potentialities of these structures.

SiGe self-assembled nanocrystals, supposed to have long spin coherence times, have been explored. We have gone through single-hole tunneling and two-hole cotunneling, the characteristics of the finite size quantum confinement in these structures and diverse spin-related phenomena.

We have characterized the hole g-tensor of SiGe dome islands and proven that an external electric field can strongly modulate its value, at least for magnetic fields perpendicular to the substrate plane. By a detailed analysis, we ruled out the compositional-gradient mechanism as the cause of this electric-field effect. A new correction term to the g-factor, which had not been considered before in the literature, seems to be on the origin of the observed modulation.

In addition, measurements on a device with a single top-gate electrode defined close to a SiGe self-assembled quantum dots, predict that fast spin manipulations can be achieved by means of this g-tensor modulation. Rabi frequencies in the order of 100 MHz, i.e. comparable to those obtained for electrons confined in InSb nanowires, were predicted for realistic experimental conditions.

These Rabi frequencies together with the expectedly long spin coherence times for carriers in Ge underline the potential of holes confined in SiGe quantum dots for spin-based quantum information processing.

Inelastic cotunneling processes that give rise to asymmetric steps in conductance have also been observed in these structures. A joint effect of spin-orbit interaction and Zeeman splitting leads to a spin selectivity of the tunnel contacts that appears to explain our experimental findings. In addition, it allowed us to devise an original scheme for a Rabi electron pump.

This Rabi electron pump is demonstrated in InAs NWs. Although the asymmetric steps in conductance for opposite bias voltages rely on a different type of spin-orbit interaction in the case of conduction-band electrons, the operating principle of the pump is the same to the one discussed for hole-confinement in SiGe quantum dots.

Finally, the development of a directed approach to the fabrication of devices from preselected self-assembled quantum dots was described. This approach, which relies on a precise alignment of the contact electrodes onto the quantum dot, was applied to the fabrication of both single and double quantum dot devices. In particular, the first prototype device composed of two SiGe QDs and an aluminium bridge between them was presented. This important development should now give us the possibility to investigate the transfer and coupling of spin states between relatively distant quantum dots.

Appendices

Appendix I

The Luttinger Hamiltonian in [56] reads,

$$
\begin{aligned}
H = &\frac{1}{2m}\left(\gamma_1 + \frac{5}{2}\gamma_2\right)k^2 - \frac{\gamma_2}{m}\left(k_x^2 J_x^2 + k_y^2 J_y^2 + k_z^2 J_z^2\right) \\
&-\frac{2\gamma_3}{m}\left(\{k_x k_y\}\{J_x J_y\} + \{k_y k_z\}\{J_y J_z\} + \{k_z k_x\}\{J_z J_x\}\right) \\
&+\frac{e\hbar}{mc}\kappa\, \boldsymbol{J}\cdot\boldsymbol{B} + \frac{e\hbar}{mc}q\left(J_x^3 B_x + J_y^3 B_y + J_z^3 B_z\right),
\end{aligned} \tag{1}
$$

where m is the mass of the electron in vacuum, γ_1, γ_2, γ_3, κ, and q are the Luttinger parameters, $\boldsymbol{k} = (k_x, k_y, k_z)$ is the momentum of the band electron,

$$\boldsymbol{k} = -i\hbar\frac{\partial}{\partial \boldsymbol{r}} + \frac{e}{c}\boldsymbol{A}(\boldsymbol{r}), \tag{2}$$

with $\boldsymbol{A}(\boldsymbol{r})$ being the vector potential due to the magnetic field, e the elementary charge ($e > 0$), and c the speed of light. Further, $\{\dots\}$ denotes the symmetrized product, e.g.

$$\{k_x k_y\} = \frac{1}{2}\left(k_x k_y + k_y k_x\right), \tag{3}$$

and $\boldsymbol{J} = (J_x, J_y, J_z)$ are 4×4 matrices representing the spin $J = 3/2$ in a basis of choice. We choose the basis [124]

$$\left\{\left|\frac{3}{2},+\frac{3}{2}\right\rangle,\quad \left|\frac{3}{2},+\frac{1}{2}\right\rangle,\quad \left|\frac{3}{2},-\frac{1}{2}\right\rangle,\quad \left|\frac{3}{2},-\frac{3}{2}\right\rangle\right\} \tag{4}$$

where

$$\begin{aligned}
\left|\frac{3}{2},+\frac{3}{2}\right\rangle &= -\frac{1}{\sqrt{2}}\left(X+iY\right)\uparrow, \\
\left|\frac{3}{2},-\frac{3}{2}\right\rangle &= \frac{1}{\sqrt{2}}\left(X-iY\right)\downarrow, \\
\left|\frac{3}{2},+\frac{1}{2}\right\rangle &= \frac{1}{\sqrt{6}}\left[-\left(X+iY\right)\downarrow+2Z\uparrow\right], \\
\left|\frac{3}{2},-\frac{1}{2}\right\rangle &= \frac{1}{\sqrt{6}}\left[\left(X-iY\right)\uparrow+2Z\downarrow\right].
\end{aligned} \tag{5}$$

Here, the Bloch amplitudes X, Y, and Z are chosen to be real. The states in Eq. (5) originate from the addition [125] $\boldsymbol{J}=\boldsymbol{I}+\boldsymbol{S}$, where $\boldsymbol{S}$ is the electron spin ($S=1/2$) in the usual basis $\{\uparrow,\downarrow\}$. The subspace of $J=3/2$ is shown in Eq. (5), whereas the subspace of $J=1/2$ is neglected, because it corresponds to the split-off band. The Luttinger Hamiltonian describes the very top of the valance band, at energies $E\ll\Delta_{\mathrm{SO}}$.

In the basis given by Eqs. (4) and (5), the matrices of $J=3/2$ read [124],

$$J_x=\begin{pmatrix} 0 & \frac{\sqrt{3}}{2} & 0 & 0 \\ \frac{\sqrt{3}}{2} & 0 & 1 & 0 \\ 0 & 1 & 0 & \frac{\sqrt{3}}{2} \\ 0 & 0 & \frac{\sqrt{3}}{2} & 0 \end{pmatrix}, \tag{6}$$

$$J_y=\begin{pmatrix} 0 & -i\frac{\sqrt{3}}{2} & 0 & 0 \\ i\frac{\sqrt{3}}{2} & 0 & -i & 0 \\ 0 & i & 0 & -i\frac{\sqrt{3}}{2} \\ 0 & 0 & i\frac{\sqrt{3}}{2} & 0 \end{pmatrix}, \tag{7}$$

$$J_z=\begin{pmatrix} \frac{3}{2} & 0 & 0 & 0 \\ 0 & \frac{1}{2} & 0 & 0 \\ 0 & 0 & -\frac{1}{2} & 0 \\ 0 & 0 & 0 & -\frac{3}{2} \end{pmatrix}. \tag{8}$$

In Eq. (1), the axes x, y, and z are fixed along the main crystallographic directions of the cubic crystal. We choose the axis $z\equiv[001]$ to point along the growth direction of the nanocrystal, making it the axis of the strongest size quantization.

We can then expand the Luttinger Hamiltonian around the 2D limit. This consists in regarding quantities like z and $\partial/\partial z$ as proportional to w and $1/w$, respectively. Here, w is the width of the 2D layer (i.e.the height of the nanocrystal), which is considered to be much smaller than the nanocrystal diameter d [3]. On the other hand, quantities like x and $\partial/\partial x$ are regarded as proportional to d and $1/d$, respectively (the same premise is made for y and $\partial/\partial y$).

Before expanding in powers of $w/d \ll 1$, it is convenient to represent the Luttinger Hamiltonian in a block form. We use two projection operators, p_h and p_l, which project on the subspaces of the heavy (h) and light (l) holes. In terms of J_z, they are written as

$$\begin{aligned} p_h &= \frac{1}{2}\left(J_z^2 - \frac{1}{4}\right), \\ p_l &= \frac{1}{2}\left(\frac{9}{4} - J_z^2\right). \end{aligned} \tag{9}$$

p_h and p_l resolve the unity, $p_h + p_l = 1$, and have the usual properties of projection operators: $p_h^2 = p_h$, $p_l^2 = p_l$, and $p_h p_l = p_l p_h = 0$.

The Luttinger Hamiltonian in Eq. (1) can then be written as follows

$$\begin{aligned} H &= (p_h + p_l)H(p_h + p_l) = H_{hh}\left|h\right\rangle\left\langle h\right| + H_{hl}\left|h\right\rangle\left\langle l\right| \\ &+ H_{lh}\left|l\right\rangle\left\langle h\right| + H_{ll}\left|l\right\rangle\left\langle l\right|, \end{aligned} \tag{10}$$

which makes up a matrix in the (h,l)-space,

$$H = \begin{pmatrix} H_{hh} & H_{hl} \\ H_{lh} & H_{ll} \end{pmatrix}. \tag{11}$$

Each element H_{ij} can be represented as a 2×2 matrix in the space of the pseudo-spin. The Pauli matrices $\boldsymbol{\sigma} = (\sigma_x, \sigma_y, \sigma_z)$ represent the remaining pseudo-spin degree of freedom in each block. The blocks on the diagonal read

$$\begin{aligned} H_{hh} &= \frac{\gamma_1 + \gamma_2}{2m}\left(k_x^2 + k_y^2\right) + \frac{\gamma_1 - 2\gamma_2}{2m}k_z^2 \\ &+ \frac{1}{2}\mu_B \boldsymbol{\sigma} \cdot g_h \cdot \boldsymbol{B} + U(x,y) + V_h(z), \\ H_{ll} &= \frac{\gamma_1 - \gamma_2}{2m}\left(k_x^2 + k_y^2\right) + \frac{\gamma_1 + 2\gamma_2}{2m}k_z^2 \\ &+ \frac{1}{2}\mu_B \boldsymbol{\sigma} \cdot g_l \cdot \boldsymbol{B} + U(x,y) + V_l(z), \end{aligned} \tag{12}$$

---

[3] For SiGe dome islands, $w/d \sim 0.2$.

where the g-factors g_h and g_l are tensors and $U(x,y)$ was included as an in-plane confinement potential. The motion along z is confined to an infinitely deep square well, with different offsets, V_h and $V_l > V_h$, due to strain. In the frame (x,y,z), g_h and g_l are diagonal:

$$g_h = \begin{pmatrix} 3q & 0 & 0 \\ 0 & 3q & 0 \\ 0 & 0 & -6\kappa - \frac{27}{2}q \end{pmatrix}, \tag{13}$$

and

$$g_l = \begin{pmatrix} 4\kappa + 10q & 0 & 0 \\ 0 & 4\kappa + 10q & 0 \\ 0 & 0 & 2\kappa + \frac{1}{2}q \end{pmatrix}. \tag{14}$$

It is important to remark that in Eq. 11 the off-blocks are related to each other by hermiticity,

$$H_{hl} = (H_{lh})^{\dagger}. \tag{15}$$

For H_{lh}, we have

$$\begin{aligned} H_{lh} \;=\; & -i\frac{\sqrt{3}\gamma_3}{m}\left(\{k_x k_z\}\sigma_y + \{k_y k_z\}\sigma_x\right) \\ & -\frac{\sqrt{3}\gamma_2}{2m}\left(k_x^2 - k_y^2\right) + i\frac{\sqrt{3}\gamma_3}{m}\{k_x k_y\}\sigma_z \\ & +\sqrt{3}\mu_B\left(\kappa + \frac{7}{4}q\right)(\sigma_x B_x - \sigma_y B_y). \end{aligned} \tag{16}$$

All we have done so far was to rewrite the Luttinger Hamiltonian in a block form. Next we proceed with the expansion in powers of $w/d \ll 1$ as explained above. We allow for gauges of the form

$$\begin{aligned} A_x &= zB_y - \tau y B_z, \\ A_y &= -zB_x + (1-\tau)xB_z, \\ A_z &= 0, \end{aligned} \tag{17}$$

where τ is a real number expressing the remaining gauge freedom in two dimensions. After taking the 2D limit, we will be able to use a reduced (2D) vector potential, $\boldsymbol{a} = (a_x, a_y)$, which is given by

$$\begin{aligned} a_x &= -\tau y B_z, \\ a_y &= (1-\tau)xB_z. \end{aligned} \tag{18}$$

Having in mind such a transition and substituting Eq. 17 into Eq. 2, we can leave out the z-dependence from k_x and k_y,

$$\begin{aligned} k_x &\rightarrow k_x + \frac{eB_y}{c}z, \\ k_y &\rightarrow k_y - \frac{eB_x}{c}z. \end{aligned} \tag{19}$$

Here, on the right-hand side, k_x and k_y do not depend on z anymore, because they are given in terms of the 2D vector potential $\boldsymbol{a}(x, y)$ as

$$\begin{aligned} k_x &= -i\hbar\frac{\partial}{\partial x} + \frac{e}{c}a_x = -i\hbar\frac{\partial}{\partial x} + \frac{e}{c}(-\tau y B_z), \\ k_y &= -i\hbar\frac{\partial}{\partial y} + \frac{e}{c}a_y = -i\hbar\frac{\partial}{\partial y} + \frac{e}{c}(1-\tau)xB_z. \end{aligned} \tag{20}$$

The next step is to substitute Eq. (19) into the Luttinger Hamiltonian and to group the terms according to their order of w/d. The substitution of Eq. (19) in the blocks H_{hh} and H_{ll} produces linear in k_x and k_y terms which are not multiplied by any Pauli matrix. Such terms can be gauged away after integration over z, since they correspond to a constant shift in a_x and a_y. They also admix higher heavy-hole subbands and slightly renormalize the inplane mass, but this admixture, as well as the mass renormalization, vanishes in the limit $w \rightarrow 0$, because the corresponding perturbation is proportional to z. Therefore, we dispense with the new terms generated in H_{hh} and H_{ll}.

We note that, for the blocks H_{hh} and H_{ll}, the transition to 2D is identical to what is usually done for electrons in the conduction band.

For the blocks H_{lh} and H_{hl}, we make the substitution in Eq. (19) and obtain lots of terms. The origin of each term can be traced back through the following intermediate step:

$$\begin{aligned}
\{k_xk_z\} &\rightarrow k_xk_z + \frac{eB_y}{c}\{zk_z\}, \\
\{k_yk_z\} &\rightarrow k_yk_z - \frac{eB_x}{c}\{zk_z\}, \\
k_x^2 - k_y^2 &\rightarrow k_x^2 - k_y^2 + \frac{2e}{c}(k_xB_y + k_yB_x)z \\
&\quad + \frac{e^2}{c^2}\left(B_y^2 - B_x^2\right)z^2, \\
\{k_xk_y\} &\rightarrow \{k_xk_y\} + \frac{e}{c}(k_yB_y - k_xB_x)z \\
&\quad - \frac{e^2}{c^2}B_xB_yz^2. \qquad (21)
\end{aligned}$$

Then, we classify all terms according to their order of $w/d \ll 1$. The leading order is that of $(w/d)^{-1} \gg 1$ and the off-block acquires the following main term

$$H_{lh}^{(0)} = -i\frac{\sqrt{3}\gamma_3}{m}(k_x\sigma_y + k_y\sigma_x)k_z. \qquad (22)$$

It is important to remark that k_x and k_y contain only the z-component of the magnetic field. The transverse components B_x and B_y do not appear in H_{lh} at this order of w/d. On this reason, the component B_z has a larger effect on breaking the time-reversal symmetry than the other two components.

The next order is that of $(w/d)^0 \sim 1$ and the off-block acquires the following correction

$$\begin{aligned}
H_{lh}^{(1)} &= -\frac{\sqrt{3}\gamma_2}{2m}\left(k_x^2 - k_y^2\right) + i\frac{\sqrt{3}\gamma_3}{m}\{k_xk_y\}\sigma_z \\
&\quad + \sqrt{3}\mu_B\left(\kappa + \frac{7}{4}q + \frac{2i\gamma_3}{\hbar}\{zk_z\}\right)(\sigma_xB_x - \sigma_yB_y).
\end{aligned} \qquad (23)$$

Further, there are two more orders: $(w/d)^1 \ll 1$ and $(w/d)^2 \ll 1$, originating from terms containing z and z^2, respectively. If they are required, one can find them by substituting Eq. (21) into Eq. (16).

While in the blocks H_{hh} and H_{ll} we discard all terms that vanish in the 2D limit ($w/d \to 0$), in the blocks H_{hl} and H_{lh} we keep only the leading-order in w/d terms. These blocks intermix heavy holes and light holes, such that the wave function of the hole in a given QD state assumes the general form

$\Psi = \alpha\Psi_h + \beta\Psi_l$. In terms of the true-spin states, such a wave function consists of a superposition of the spin-up ($\uparrow$) and spin-down ($\downarrow$) states entangled with the orbital degrees of freedom:

$$\begin{aligned}
\Psi_{\Uparrow}(\boldsymbol{r}) &= \Phi_1(\boldsymbol{r})\uparrow + \chi_1(\boldsymbol{r})\downarrow, \\
\Psi_{\Downarrow}(\boldsymbol{r}) &= \chi_2(\boldsymbol{r})\uparrow + \Phi_2(\boldsymbol{r})\downarrow,
\end{aligned} \tag{24}$$

where $\Uparrow$ and $\Downarrow$ denote the components of the Kramers doublet in the QD.

Appendix II

In order to derive the expression for the Rabi frequency in Chapter 3 section 3.4, let us consider a spin 1/2 driven by the g-tensor modulation. The time evolution of the spin is governed by the Bloch equation,

$$\frac{d}{dt}\left\langle \boldsymbol{S} \right\rangle = \left[\boldsymbol{\omega}_{\mathrm{L}} + \delta\boldsymbol{\omega}(t)\right] \times \left\langle \boldsymbol{S} \right\rangle , \tag{25}$$

where $\langle \boldsymbol{S} \rangle$ is the expectation value of the spin $\boldsymbol{S} = (1/2)\,\boldsymbol{\sigma}$, with $\boldsymbol{\sigma}$ being the Pauli matrices, $\boldsymbol{\omega}_{\mathrm{L}}$ is the Larmor frequency, and $\delta\boldsymbol{\omega}(t)$ is the time-dependent frequency part due to the driving field. In the g-tensor modulation, the driving field arises because of the *ac* signal sent to the top gate,

$$V_{\mathrm{tg}}(t) = V_{\mathrm{tg}}^{0} + V_{\mathrm{ac}} \sin\left(\omega_{\mathrm{ac}} t\right) , \tag{26}$$

where V_{tg}^{0} is the average value of the top-gate voltage, V_{ac} is the resulting amplitude of voltage oscillations, and ω_{ac} is the *ac* angular frequency. Since we use dome-like SiGe nanocrystals, which roughly obey rotational symmetry about the axis $z \equiv [001]$, the g-tensor $\hat{g}$ is approximately diagonal in the main crystallographic frame (x, y, z). The non-zero elements of $\hat{g}$ include two equal-to-each-other inplane components, $g_x = g_y \equiv g_{\parallel}$, and one out-of-plane component, $g_z \equiv g_{\perp}$. The g-tensor modulation can, therefore, be written as

$$\begin{aligned} g_{\parallel}(t) &\approx g_{\parallel}^{0} + \alpha_{\parallel} V_{\mathrm{ac}} \sin\left(\omega_{\mathrm{ac}} t\right) , \\ g_{\perp}(t) &\approx g_{\perp}^{0} + \alpha_{\perp} V_{\mathrm{ac}} \sin\left(\omega_{\mathrm{ac}} t\right) , \end{aligned} \tag{27}$$

where $g_{\parallel}^{0} \equiv g_{\parallel}$ and $g_{\perp}^{0} \equiv g_{\perp}$ are constant, $\alpha_{\parallel} = \frac{\partial g_{\parallel}}{\partial V_{\mathrm{tg}}}$, and $\alpha_{\perp} = \frac{\partial g_{\perp}}{\partial V_{\mathrm{tg}}}$. Here, it was assumed that V_{ac} is sufficiently small, so that $g_{\parallel}$ and $g_{\perp}$ depend linearly on V_{tg} in the voltage window $V_{\mathrm{tg}}^{0} \pm V_{\mathrm{ac}}$. Thus, the Larmor frequency entering in Eq. (25) is identified as

$$\boldsymbol{\omega}_{\mathrm{L}} = \frac{\mu_{\mathrm{B}}}{\hbar} \hat{g} \cdot \boldsymbol{B}, \tag{28}$$

whereas the contribution due to driving as

$$\delta\boldsymbol{\omega}(t) = \frac{\mu_{\mathrm{B}}}{\hbar} \left(\hat{\alpha} \cdot \boldsymbol{B}\right) V_{ac} \sin\left(\omega_{\mathrm{ac}} t\right) . \tag{29}$$

To be concise here, we used tensor-vector multiplication, like $(\hat{g} \cdot \boldsymbol{B})_i = \sum_j g_{ij} B_j$. The tensor of linear coefficients, $\alpha_{ij} = \partial g_{ij}/\partial V_{\mathrm{tg}}$, needs not, in general, be proportional to $\hat{g}$. Therefore, the time-dependent driving $\delta\boldsymbol{\omega}(t)$ may have a component that is transverse to the vector $\boldsymbol{\omega}_{\mathrm{L}}$, *cf.* Eqs. (28) and (29). This circumstance is at the heart of the g-tensor modulation technique and necessary in order to induce Rabi oscillations.

It is easiest to solve Eq. (25) in a frame rotating at frequency ω_{ac} about the vector $\boldsymbol{\omega}_{\mathrm{L}}$. The time evolution of the spin is approximated as follows

$$\begin{aligned} \langle S_\pm(t) \rangle &\approx \tilde{S}_\pm(t) e^{\pm i\omega_{ac} t}, \\ \langle S_Z(t) \rangle &\approx \tilde{S}_Z(t), \end{aligned} \tag{30}$$

where $S_\pm = S_X \pm i S_Y$ and the coordinate frame (X, Y, Z) has $Z \parallel \boldsymbol{\omega}_{\mathrm{L}}$. The new unknown functions $\tilde{\boldsymbol{S}}(t)$ obey a time-independent Bloch equation

$$\frac{d}{dt}\tilde{\boldsymbol{S}} = (\boldsymbol{\delta} + \boldsymbol{\omega}_{\mathrm{R}}) \times \tilde{\boldsymbol{S}}, \tag{31}$$

where $\boldsymbol{\delta} = \boldsymbol{\omega}_{\mathrm{L}} (1 - \omega_{ac}/\omega_{\mathrm{L}})$ is the detuning from resonance and $\boldsymbol{\omega}_{\mathrm{R}}$ is the Rabi frequency given by [21]

$$\boldsymbol{\omega}_{\mathrm{R}} = \frac{\mu_B}{2\hbar} V_{ac} \left[(\hat{\alpha} \cdot \boldsymbol{B}) \times \boldsymbol{n} \right], \tag{32}$$

where $\boldsymbol{n} = \boldsymbol{\omega}_{\mathrm{L}}/\omega_{\mathrm{L}}$ is the unit vector along the Larmor frequency.

Next, we consider the situation realized in the experiment. The magnetic field can be rotated in a plane perpendicular to the substrate. Let us assume that it is the (y, z)-plane and represent the magnetic field as

$$\boldsymbol{B} = \boldsymbol{e}_y B_\parallel + \boldsymbol{e}_z B_\perp, \tag{33}$$

where $\boldsymbol{e}_i$ $(i = x, y, z)$ are unit vectors. Then, the Rabi frequency reads $\boldsymbol{\omega}_{\mathrm{R}} = \boldsymbol{e}_x \omega_{\mathrm{R}}$, with

$$\begin{aligned} \omega_{\mathrm{R}} &= \frac{\mu_B V_{\mathrm{ac}}}{2\hbar} \left[\frac{1}{g_\parallel} \left(\frac{\partial g_\parallel}{\partial V_{\mathrm{tg}}} \right) - \frac{1}{g_\perp} \left(\frac{\partial g_\perp}{\partial V_{\mathrm{tg}}} \right) \right] \\ &\quad \times \frac{g_\parallel g_\perp B_\parallel B_\perp}{\sqrt{\left(g_\parallel B_\parallel\right)^2 + \left(g_\perp B_\perp\right)^2}}. \end{aligned} \tag{34}$$

In this expression, the two components of the magnetic field are given by $B_\parallel = B\cos\theta$ and $B_\perp = B\sin\theta$, where θ is the angle of the magnetic field measured with respect to the growth plane. By absolute value, ω_{R} is largest at

$$\theta = \pm \arctan\left(\sqrt{\left| \frac{g_\parallel}{g_\perp} \right|} \right), \tag{35}$$

attaining

$$\omega_{\mathrm{R}} = \pm\frac{\mu_B V_{\mathrm{ac}}}{2\hbar}\left[\frac{1}{g_\parallel}\left(\frac{\partial g_\parallel}{\partial V_{\mathrm{tg}}}\right) - \frac{1}{g_\perp}\left(\frac{\partial g_\perp}{\partial V_{\mathrm{tg}}}\right)\right]\frac{g_\parallel g_\perp B}{\left|g_\parallel\right| + |g_\perp|}. \tag{36}$$

Bibliography

[1] Daniel Loss and David P DiVincenzo. Quantum computation with quantum dots. *Physical Review A*, 57(1):120, 1998.

[2] R Hanson, LP Kouwenhoven, JR Petta, S Tarucha, and LMK Vandersypen. Spins in few-electron quantum dots. *Reviews of Modern Physics*, 79(4):1217, 2007.

[3] Hendrik Bluhm, Sandra Foletti, Diana Mahalu, Vladimir Umansky, and Amir Yacoby. Enhancing the coherence of a spin qubit by operating it as a feedback loop that controls its nuclear spin bath. *Physical Review letters*, 105(21):216803, 2010.

[4] Hendrik Bluhm, Sandra Foletti, Izhar Neder, Mark Rudner, Diana Mahalu, Vladimir Umansky, and Amir Yacoby. Dephasing time of GaAs electron-spin qubits coupled to a nuclear bath exceeding 200μs. *Nature Physics*, 7(2):109–113, 2010.

[5] Floris A Zwanenburg, Andrew S Dzurak, Andrea Morello, Michelle Y Simmons, Lloyd C L Hollenberg, Gerhard Klimeck, Sven Rogge, Susan N Coppersmith, and Mark A Eriksson. Silicon quantum electronics. *Reviews of Modern Physics*, 85(3):961–1019, 2013.

[6] CW Leitz, MT Currie, ML Lee, Z-Y Cheng, DA Antoniadis, and EA Fitzgerald. Hole mobility enhancements and alloy scattering-limited mobility in tensile strained Si/SiGe surface channel metal-oxide-semiconductor field-effect transistors. *Journal of Applied physics*, 92(7):3745–3751, 2002.

[7] DJ Eaglesham and M Cerullo. Dislocation-free stranski-krastanow growth of Ge on Si (100). *Physical Review letters*, 64(16):1943–1946, 1990.

[8] Y-W Mo, DE Savage, BS Swartzentruber, and MG Lagally. Kinetic pathway in Stranski-Krastanov growth of Ge on Si (001). *Physical Review letters*, 65(8):1020–1023, 1990.

[9] Gilberto Medeiros-Ribeiro, Alexander M Bratkovski, Theodore I Kamins, Douglas AA Ohlberg, and R Stanley Williams. Shape transition of germanium nanocrystals on a silicon (001) surface from pyramids to domes. *Science*, 279(5349):353–355, 1998.

[10] J Stangl, V Holỳ, and G Bauer. Structural properties of self-organized semiconductor nanostructures. *Reviews of Modern physics*, 76(3):725, 2004.

[11] A Rastelli. *Structural Evolution of Nanoscopic Islands of Ge and SiGe on Si (001).* PhD thesis, Università degli Studi di Pavia, 2002.

[12] Jean-Marc Baribeau, X Wu, NL Rowell, and DJ Lockwood. Ge dots and nanostructures grown epitaxially on Si. *Journal of Physics: Condensed Matter*, 18(8):R139, 2006.

[13] G Katsaros, P Spathis, M Stoffel, F Fournel, M Mongillo, Vincent Bouchiat, F Lefloch, A Rastelli, OG Schmidt, and S De Franceschi. Hybrid superconductor-semiconductor devices made from self-assembled SiGe nanocrystals on silicon. *Nature nanotechnology*, 5(6):458–464, 2010.

[14] G Katsaros, J Tersoff, M Stoffel, A Rastelli, P Acosta-Diaz, GS Kar, Giovanni Costantini, OG Schmidt, and K Kern. Positioning of strained islands by interaction with surface nanogrooves. *Physical Review letters*, 101(9):096103, 2008.

[15] Oliver G Schmidt. *Lateral alignment of epitaxial quantum dots*, volume 1. Springer, 2007.

[16] Oliver G Schmidt and Karl Eberl. Self-assembled Ge/Si dots for faster field-effect transistors. *Electron Devices, IEEE Transactions on*, 48(6):1175–1179, 2001.

[17] MLW Thewalt, DA Harrison, CF Reinhart, JA Wolk, and H Lafontaine. Type II Band Alignment in Si_{1-x} Ge_x/Si (001) Quantum Wells: The Ubiquitous Type I Luminescence Results from Band Bending. *Physical Review letters*, 79(2):269–272, 1997.

[18] Chris G Van de Walle and Richard M Martin. Theoretical calculations of heterojunction discontinuities in the Si/Ge system. *Physical Review B*, 34(8):5621, 1986.

[19] TU Schülli, M Stoffel, A Hesse, J Stangl, RT Lechner, E Wintersberger, M Sztucki, TH Metzger, OG Schmidt, and G Bauer. Influence of growth temperature on interdiffusion in uncapped SiGe-islands on Si (001) determined by anomalous x-ray diffraction and reciprocal space mapping. *Physical Review B*, 71(3):035326, 2005.

[20] G Katsaros. *Investigation of the properties of SiGe islands by selective wet chemical etching and scanning probe microscopy.* PhD thesis, Universität Konstanz, 2006.

[21] Vitaly N Golovach, Massoud Borhani, and Daniel Loss. Electric-dipole-induced spin resonance in quantum dots. *Physical Review B*, 74(16):165319, 2006.

[22] KC Nowack, FHL Koppens, Yu V Nazarov, and LMK Vandersypen. Coherent control of a single electron spin with electric fields. *Science*, 318(5855):1430–1433, 2007.

[23] S Nadj-Perge, SM Frolov, EPAM Bakkers, and LP Kouwenhoven. Spin-orbit qubit in a semiconductor nanowire. *Nature*, 468(7327):1084–1087, 2010.

[24] M Jung, K Hirakawa, Y Kawaguchi, S Komiyama, S Ishida, and Y Arakawa. Lateral electron transport through single self-assembled InAs quantum dots. *Applied Physics Letters*, 86(3):033106–033106, 2005.

[25] Kohei Hamaya, M Kitabatake, K Shibata, M Jung, M Kawamura, K Hirakawa, T Machida, T Taniyama, S Ishida, and Y Arakawa. Kondo effect in a semiconductor quantum dot coupled to ferromagnetic electrodes. *Applied Physics Letters*, 91(23):232105–232105, 2007.

[26] Christo Buizert, Akira Oiwa, Kenji Shibata, Kazuhiro Hirakawa, and Seigo Tarucha. Kondo universal scaling for a quantum dot coupled to superconducting leads. *Physical Review letters*, 99(13):136806, 2007.

[27] DV Averin and Yu V Nazarov. Virtual electron diffusion during quantum tunneling of the electric charge. *Physical Review letters*, 65(19):2446, 1990.

[28] DV Averin and Yu V Nazarov. Single charge tunneling. In *Proceedings of a NATO Advanced Study Institute, H Grabert, MH Devoret, Eds., Les Houches, France*, volume 5, 1992.

[29] Yasuhiro Funabashi, Kazuhiko Eto, and Kiyoshi Kawamura. Phase relaxation and non-equilibrium transport properties through multilevel quantum dot. *Japanese journal of applied physics*, 38:388, 1999.

[30] Leo P Kouwenhoven, DG Austing, and Seigo Tarucha. Few-electron quantum dots. *Reports on Progress in Physics*, 64(6):701, 2001.

[31] LH Willems van Beveren, R Hanson, IT Vink, FHL Koppens, LP Kouwenhoven, and LMK Vandersypen. Spin filling of a quantum dot derived from excited-state spectroscopy. *New Journal of Physics*, 7(1):182, 2005.

[32] Vladimir I Falko, BL Altshuler, and O Tsyplyatyev. Anisotropy of spin splitting and spin relaxation in lateral quantum dots. *Physical Review letters*, 95(7):076603, 2005.

[33] Claudine Hermann and Claude Weisbuch. k p perturbation theory in III-V compounds and alloys: a reexamination. *Physical Review B*, 15(2):823, 1977.

[34] MT Björk, A Fuhrer, AE Hansen, MW Larsson, LE Fröberg, and Lars Samuelson. Tunable effective g factor in InAs nanowire quantum dots. *Physical Review B*, 72(20):201307, 2005.

[35] Neil W Ashcroft and N David Mermin. Solid state physics. *Saunders College, Philadelphia*, 1, 1976.

[36] Nakul Shaji, CB Simmons, Madhu Thalakulam, Levente J Klein, Hua Qin, H Luo, DE Savage, MG Lagally, AJ Rimberg, R Joynt, et al. Spin blockade and lifetime-enhanced transport in a few-electron Si/SiGe double quantum dot. *Nature Physics*, 4(7):540–544, 2008.

[37] K Ono, DG Austing, Y Tokura, and S Tarucha. Current rectification by Pauli exclusion in a weakly coupled double quantum dot system. *Science*, 297(5585):1313–1317, 2002.

[38] S De Franceschi, S Sasaki, JM Elzerman, WG Van Der Wiel, S Tarucha, and Leo P Kouwenhoven. Electron cotunneling in a semiconductor quantum dot. *Physical Review letters*, 86(5):878–881, 2001.

[39] AV Nenashev, AV Dvurechenskii, and AF Zinovieva. Wave functions and g factor of holes in Ge/Si quantum dots. *Physical Review B*, 67(20):205301, 2003.

[40] JC Hensel and K Suzuki. Anisotropy of the g factor of the free hole in Ge and conduction-band spin-orbit splitting. *Physical Review letters*, 22(16):838–840, 1969.

[41] K-M Haendel, R Winkler, U Denker, OG Schmidt, and RJ Haug. Giant anisotropy of Zeeman splitting of quantum confined acceptors in Si/Ge. *Physical Review letters*, 96(8):086403, 2006.

[42] S Roddaro, A Fuhrer, P Brusheim, C Fasth, HQ Xu, L Samuelson, J Xiang, and CM Lieber. Spin states of holes in Ge/Si nanowire quantum dots. *Physical Review letters*, 101(18):186802, 2008.

[43] Neil Manning Atherton. *Electron spin resonance: theory and applications*. Ellis Horwood Chichester, 1973.

[44] Hans-Andreas Engel and Daniel Loss. Detection of single spin decoherence in a quantum dot via charge currents. *Physical Review letters*, 86(20):4648, 2001.

[45] Hans-Andreas Engel and Daniel Loss. Single-spin dynamics and decoherence in a quantum dot via charge transport. *Physical Review B*, 65(19):195321, 2002.

[46] FHL Koppens, Christo Buizert, Klaas-Jan Tielrooij, IT Vink, KC Nowack, Tristan Meunier, LP Kouwenhoven, and LMK Vandersypen. Driven coherent oscillations of a single electron spin in a quantum dot. *Nature*, 442(7104):766–771, 2006.

[47] JR Petta, AC Johnson, JM Taylor, EA Laird, A Yacoby, MD Lukin, CM Marcus, MP Hanson, and AC Gossard. Coherent manipulation of coupled electron spins in semiconductor quantum dots. *Science*, 309(5744):2180–2184, 2005.

[48] Y Kato, RC Myers, DC Driscoll, AC Gossard, J Levy, and DD Awschalom. Gigahertz electron spin manipulation using voltage-controlled g-tensor modulation. *Science*, 299(5610):1201–1204, 2003.

[49] Gian Salis, Y Kato, K Ensslin, DC Driscoll, AC Gossard, and DD Awschalom. Electrical control of spin coherence in semiconductor nanostructures. *Nature*, 414(6864):619–622, 2001.

[50] RS Deacon, Y Kanai, S Takahashi, A Oiwa, K Yoshida, K Shibata, K Hirakawa, Y Tokura, and S Tarucha. Electrically tuned g tensor in an InAs self-assembled quantum dot. *Physical Review B*, 84(4):041302, 2011.

[51] V Jovanov, T Eissfeller, S Kapfinger, EC Clark, F Klotz, M Bichler, JG Keizer, PM Koenraad, G Abstreiter, and JJ Finley. Observation and explanation of strong electrically tunable exciton g factors in composition engineered In(Ga)As quantum dots. *Physical Review B*, 83(16):161303, 2011.

[52] Craig E Pryor and Michael E Flatté. Landé g factors and orbital momentum quenching in semiconductor quantum dots. *Physical Review letters*, 96(2):026804, 2006.

[53] N Ares, V N Golovach, G Katsaros, M Stoffel, F Fournel, L I Glazman, O G Schmidt, and S De Franceschi. Nature of Tunable Hole g Factors in Quantum Dots. *Physical Review letters*, 110(046602), 2013.

[54] N Ares, G Katsaros, VN Golovach, JJ Zhang, A Prager, LI Glazman, OG Schmidt, and S De Franceschi. SiGe quantum dots for fast hole spin Rabi oscillations. *Applied Physics letters*, 103:263113, 2013.

[55] Glen D Wilk, Robert M Wallace, and JM Anthony. High-κ gate dielectrics: Current status and materials properties considerations. *Journal of Applied Physics*, 89(10):5243–5275, 2001.

[56] JM Luttinger. Quantum theory of cyclotron resonance in semiconductors: General theory. *Physical Review*, 102(4):1030, 1956.

[57] MI Dyakonov. Basics of Semiconductor and spin physics. In *Spin Physics in Semiconductors*, pages 1–28. Springer, 2008.

[58] Roland Winkler. *Spin-orbit coupling effects in two-dimensional electron and hole systems*, volume 191. Springer, 2003.

[59] HW Van Kesteren, EC Cosman, WAJA Van der Poel, and CT Foxon. Fine structure of excitons in type-II GaAs/AlAs quantum wells. *Physical Review B*, 41(8):5283, 1990.

[60] R Winkler, M Merkler, T Darnhofer, and Ulrich Rössler. Theory for the cyclotron resonance of holes in strained asymmetric Ge-SiGe quantum wells. *Physical Review B*, 53(16):10858, 1996.

[61] Martin M Rieger and P Vogl. Electronic-band parameters in strained Si_{1-x} Ge_x alloys on Si_{1-y} Ge_y substrates. *Physical Review B*, 48(19):14276, 1993.

[62] KA Matveev, LI Glazman, and AI Larkin. g-factors of discrete levels in nanoparticles. *Physical Review letters*, 85(13):2789, 2000.

[63] MI Dyakonov and AV Khaetskii. Size quantization of holes in a semiconductor with complicated valence band and of carriers in a gapless semiconductor. *Zh. Eksp. Teor. Fiz*, 82:1584, 1982.

[64] Laura M Roth, Benjamin Lax, and Solomon Zwerdling. Theory of optical magneto-absorption effects in semiconductors. *Physical Review*, 114(1):90, 1959.

[65] AA Kiselev, EL Ivchenko, and Ulrich Rössler. Electron g factor in one- and zero-dimensional semiconductor nanostructures. *Physical Review B*, 58(24):16353, 1998.

[66] JWG Van den Berg, S Nadj-Perge, VS Pribiag, SR Plissard, EPAM Bakkers, SM Frolov, and LP Kouwenhoven. Fast Spin-Orbit Qubit in an Indium Antimonide Nanowire. *Physical Review letters*, 110(6):066806, 2013.

[67] R Hanson, IT Vink, DP DiVincenzo, LMK Vandersypen, JM Elzerman, LH van Beveren, and LP Kouwenhoven. Determination of the tunnel rates through a few-electron quantum dot. *arXiv preprint cond-mat/0407793*, 2004.

[68] Igor Žutić, Jaroslav Fabian, and S Das Sarma. Spintronics: Fundamentals and applications. *Reviews of Modern physics*, 76(2):323, 2004.

[69] Emmanuel I Rashba. Restrictions on modeling spin injection by resistor networks. *Semiconductor Science and Technology*, 23(11):114015, 2008.

[70] Hyun Cheol Koo, Jae Hyun Kwon, Jonghwa Eom, Joonyeon Chang, Suk Hee Han, and Mark Johnson. Control of spin precession in a spin-injected field effect transistor. *Science*, 325(5947):1515–1518, 2009.

[71] Ian Appelbaum, Biqin Huang, and Douwe J Monsma. Electronic measurement and control of spin transport in silicon. *Nature*, 447(7142):295–298, 2007.

[72] CH Li, OMJ van't Erve, and BT Jonker. Electrical injection and detection of spin accumulation in silicon at 500K with magnetic metal/silicon dioxide contacts. *Nature Communications*, 2:245, 2011.

[73] Kazuhito Tsukagoshi, Bruce W Alphenaar, and Hiroki Ago. Coherent transport of electron spin in a ferromagnetically contacted carbon nanotube. *Nature*, 401(6753):572–574, 1999.

[74] Sangeeta Sahoo, Takis Kontos, Jürg Furer, Christian Hoffmann, Matthias Gräber, Audrey Cottet, and Christian Schönenberger. Electric field control of spin transport. *Nature Physics*, 1(2):99–102, 2005.

[75] K Hamaya, M Kitabatake, K Shibata, M Jung, M Kawamura, S Ishida, T Taniyama, K Hirakawa, Y Arakawa, and T Machida. Oscillatory changes in the tunneling magnetoresistance effect in semiconductor quantum-dot spin valves. *Physical Review B*, 77(8):081302, 2008.

[76] FA Zwanenburg, DW van der Mast, HB Heersche, LP Kouwenhoven, and EPAM Bakkers. Electric field control of magnetoresistance in InP nanowires with ferromagnetic contacts. *Nano letters*, 9(7):2704–2709, 2009.

[77] En-Shao Liu, Junghyo Nah, Kamran M Varahramyan, and Emanuel Tutuc. Lateral Spin Injection in Germanium Nanowires. *Nano letters*, 10(9):3297–3301, 2010.

[78] G Katsaros, V N Golovach, P Spathis, N Ares, M Stoffel, F Fournel, O G Schmidt, L I Glazman, and S De Franceschi. Observation of Spin-Selective Tunneling in SiGe nanocrystals. *Physical Review letters*, 107(246601), 2011.

[79] David Goldhaber-Gordon, Hadas Shtrikman, D Mahalu, David Abusch-Magder, U Meirav, and MA Kastner. Kondo effect in a single-electron transistor. *Nature*, 391(6663):156–159, 1998.

[80] O Klochan, AP Micolich, AR Hamilton, K Trunov, D Reuter, and AD Wieck. Observation of the Kondo effect in a spin-3/2 hole quantum dot. *Physical Review letters*, 107(7):076805, 2011.

[81] Silvano De Franceschi and Wilfred G Wiel. Kondo Effect in Quantum Dots. *Handbook of Nanophysics: Nanoparticles and Quantum Dots*, 2010.

[82] Boris L Altshuler, A Gh Aronov, Al L Efros, and M Pollak. Electron-electron interactions in disordered systems. *Modern Problems in Condensed Matter Physics, eds. AL Efros and M. Pollak (Elsevier, North Holland, 1985)*, page 1, 1985.

[83] F Pierre, H Pothier, P Joyez, Norman O Birge, D Esteve, and MH Devoret. Electrodynamic dip in the local density of states of a metallic wire. *Physical Review letters*, 86(8):1590, 2001.

[84] Sebastian Loth, Kirsten von Bergmann, Markus Ternes, Alexander F Otte, Christopher P Lutz, and Andreas J Heinrich. Controlling the state of quantum spins with electric currents. *Nature Physics*, 6(5):340–344, 2010.

[85] Ireneusz Weymann, Jürgen König, Jan Martinek, Józef Barnaś, and Gerd Schön. Tunnel magnetoresistance of quantum dots coupled to ferromagnetic leads in the sequential and cotunneling regimes. *Physical Review B*, 72(11):115334, 2005.

[86] Dong Bing, Lei Xiao-Lin, and Norman JM Horing. Inelastic cotunneling current and shot noise of an interacting quantum dot with ferromagnetic correlations. *Communications in Theoretical Physics*, 48(6):1099, 2007.

[87] V Fock. Physik 47,446 (1928), DARWIN CG, proc. In *Cambridge Philos. Soc*, volume 27, page 86, 1930.

[88] H Pothier, P Lafarge, C Urbina, D Esteve, and MH Devoret. Single-electron pump based on charging effects. *EPL (Europhysics Letters)*, 17(3):249, 1992.

[89] John M Martinis, M Nahum, Hans Dalsgaard Jensen, et al. Metrological accuracy of the electron pump. *Physical Review letters*, 72(6):904–907, 1994.

[90] NE Fletcher, J Ebbecke, TJBM Janssen, FJ Ahlers, M Pepper, HE Beere, and DA Ritchie. Quantized acoustoelectric current transport through a static quantum dot using a surface acoustic wave. *Physical Review B*, 68(24):245310, 2003.

[91] J Ebbecke, NE Fletcher, TJBM Janssen, FJ Ahlers, M Pepper, HE Beere, and DA Ritchie. Quantized charge pumping through a quantum dot by surface acoustic waves. *Applied Physics letters*, 84(21):4319–4321, 2004.

[92] Jukka P Pekola, Juha J Vartiainen, Mikko Möttönen, Olli-Pentti Saira, Matthias Meschke, and Dmitri V Averin. Hybrid single-electron transistor as a source of quantized electric current. *Nature Physics*, 4(2):120–124, 2007.

[93] A Fuhrer, C Fasth, and L Samuelson. Single electron pumping in InAs nanowire double quantum dots. *Applied Physics Letters*, 91(5):052109–052109, 2007.

[94] MR Buitelaar, V Kashcheyevs, PJ Leek, VI Talyanskii, CG Smith, D Anderson, GAC Jones, J Wei, and DH Cobden. Adiabatic charge pumping in carbon nanotube quantum dots. *Physical Review letters*, 101(12):126803, 2008.

[95] B Kaestner, V Kashcheyevs, G Hein, K Pierz, U Siegner, and HW Schumacher. Robust single-parameter quantized charge pumping. *Applied Physics Letters*, 92(19):192106–192106, 2008.

[96] S Amasha, K MacLean, Iuliana P Radu, DM Zumbühl, MA Kastner, MP Hanson, and AC Gossard. Spin-dependent tunneling of single electrons into an empty quantum dot. *Physical Review B*, 78(4):041306, 2008.

[97] Peter Stano and Philippe Jacquod. Spin-dependent tunneling into an empty lateral quantum dot. *Physical Review B*, 82(12):125309, 2010.

[98] Jens Paaske, Andreas Andersen, and Karsten Flensberg. Exchange cotunneling through quantum dots with spin-orbit coupling. *Physical Review B*, 82(8):081309, 2010.

[99] Xiaocheng Jiang, Qihua Xiong, Sungwoo Nam, Fang Qian, Yat Li, and Charles M Lieber. InAs/InP radial nanowire heterostructures as high electron mobility devices. *Nano letters*, 7(10):3214–3218, 2007.

[100] S Csonka, L Hofstetter, F Freitag, S Oberholzer, C Schonenberger, Thomas Sand Jespersen, Martin Aagesen, and Jesper Nygård. Giant fluctuations and gate control of the g-factor in InAs nanowire quantum dots. *Nano letters*, 8(11):3932–3935, 2008.

[101] JM Elzerman, R Hanson, LH Willems Van Beveren, B Witkamp, LMK Vandersypen, and Leo P Kouwenhoven. Single-shot read-out of an individual electron spin in a quantum dot. *Nature*, 430(6998):431–435, 2004.

[102] Mircea Trif, Vitaly N Golovach, and Daniel Loss. Spin-spin coupling in electrostatically coupled quantum dots. *Physical Review B*, 75(8):085307, 2007.

[103] C Piermarocchi, Pochung Chen, LJ Sham, and DG Steel. Optical RKKY interaction between charged semiconductor quantum dots. *Physical Review letters*, 89(16):167402, 2002.

[104] Patrik Recher, Eugene V Sukhorukov, and Daniel Loss. Quantum dot as spin filter and spin memory. *Physical Review letters*, 85(9):1962–1965, 2000.

[105] R Hanson, LMK Vandersypen, LH Willems van Beveren, JM Elzerman, IT Vink, and LP Kouwenhoven. Semiconductor few-electron quantum dot operated as a bipolar spin filter. *Physical Review B*, 70(24):241304, 2004.

[106] DS Macintyre, O Ignatova, S Thoms, and IG Thayne. Resist residues and transistor gate fabrication. *Journal of Vacuum Science & Technology B: Microelectronics and Nanometer Structures*, 27(6):2597–2601, 2009.

[107] I Maximov, AA Zakharov, T Holmqvist, L Montelius, and I Lindau. Investigation of polymethylmethacrylate resist residues using photoelectron microscopy. *Journal of Vacuum Science & Technology B: Microelectronics and Nanometer Structures*, 20(3):1139–1142, 2002.

[108] Wei Chen and Haroon Ahmed. Fabrication of 5-7 nm wide etched lines in silicon using 100 keV electron-beam lithography and polymethylmethacrylate resist. *Applied Physics letters*, 62(13):1499–1501, 1993.

[109] DG Hasko, Shazia Yasin, and A Mumtaz. Influence of developer and development conditions on the behavior of high molecular weight electron beam resists. *Journal of Vacuum Science & Technology B: Microelectronics and Nanometer Structures*, 18(6):3441–3444, 2000.

[110] Shazia Yasin, DG Hasko, and H Ahmed. Fabrication of 5 nm width lines in poly (methylmethacrylate) resist using a water: isopropyl alcohol developer and ultrasonically-assisted development. *Applied Physics Letters*, 78(18):2760–2762, 2001.

[111] Wenchuang Walter Hu, Koshala Sarveswaran, Marya Lieberman, and Gary H Bernstein. Sub-10 nm electron beam lithography using cold development of poly (methylmethacrylate). *Journal of Vacuum Science &*

Technology B: Microelectronics and Nanometer Structures, 22(4):1711–1716, 2004.

[112] Jung-Sub Wi, Hyo-Sung Lee, and Ki-Bum Kim. Enhanced Development Properties of IPA (Isopropyl Alcohol) on the PMMA Electron Beam Resist. *Electronic Materials Letters*, 3(1):1–5, 2007.

[113] P W Anderson, BI Halperin, and C M Varma. Anomalous low-temperature thermal properties of glasses and spin glasses. *Philosophical Magazine*, 25(1):1–9, 1972.

[114] WA Phillips. Tunneling states in amorphous solids. *Journal of Low Temperature Physics*, 7(3-4):351–360, 1972.

[115] MJ Kirton and MJ Uren. Noise in solid-state microstructures: A new perspective on individual defects, interface states and low-frequency ($1/f$) noise. *Advances in Physics*, 38(4):367–468, 1989.

[116] Masanaga Fukasawa, Yoshinori Nakakubo, Asahiko Matsuda, Yoshinori Takao, Koji Eriguchi, Kouichi Ono, Masaki Minami, Fumikatsu Uesawa, and Tetsuya Tatsumi. Structural and electrical characterization of HBr/O_2 plasma damage to Si substrate. *Journal of Vacuum Science & Technology A: Vacuum, Surfaces, and Films*, 29(4):041301–041301, 2011.

[117] AJ Ferguson, RG Clark, et al. Energy gap measurement of nanostructured aluminium thin films for single Cooper-pair devices. *Superconductor Science and Technology*, 21(1):015013, 2008.

[118] Wilfred G van der Wiel, Silvano De Franceschi, Jeroen M Elzerman, Toshimasa Fujisawa, Seigo Tarucha, and Leo P Kouwenhoven. Electron transport through double quantum dots. *Reviews of Modern Physics*, 75(1):1, 2003.

[119] A Vidan, RM Westervelt, M Stopa, M Hanson, and AC Gossard. Charging and spin effects in triple dot artificial molecules. *Journal of superconductivity*, 18(2):223–227, 2005.

[120] Louis Gaudreau, SA Studenikin, AS Sachrajda, Piotr Zawadzki, Alicia Kam, Jean Lapointe, Marek Korkusinski, and Pawel Hawrylak. Stability diagram of a few-electron triple dot. *Physical Review letters*, 97(3):036807, 2006.

[121] Minkyung Jung, Jens Schindele, Stefan Nau, Markus Weiss, Andreas Baumgartner, and Christian Schönenberger. Ultraclean single, double and triple carbon nanotube quantum dots with recessed Re bottom gates. *Nano Letters*, 2013.

[122] FR Braakman, P Barthelemy, C Reichl, W Wegscheider, and LMK Vandersypen. Long-distance coherent coupling in a quantum dot array. *Nature nanotechnology*, 8(6):432–437, 2013.

[123] Mark Johnson and Robert H Silsbee. Interfacial charge-spin coupling: Injection and detection of spin magnetization in metals. *Physical Review letters*, 55(17):1790, 1985.

[124] VN Abakumov, Vladimir Idelevich Perel, and IN Yassievich. *Nonradiative recombination in semiconductors*. Elsevier, 1991.

[125] JM Luttinger and W Kohn. Motion of electrons and holes in perturbed periodic fields. *Physical Review*, 97(4):869, 1955.